SUPERALLOY METALLURGY A GLEEBLE STUDY OF ENVIRONMENTAL FRACTURE IN INCONEL 601

A Thesis
presented to
the Faculty of California Polytechnic State University,
San Luis Obispo

In Partial Fulfillment
of the Requirements for the Degree
Master of Science in Materials Engineering

by
Alan C Demmons
June 2016

COMMITTEE MEMBERSHIP

TITLE: Superalloy Metallurgy A Gleeble Study Of Environmental Fracture In Inconel 601

AUTHOR: Alan C Demmons

DATE SUBMITTED: June 2016

COMMITTEE CHAIR: Dan Walsh, Ph.D.
Professor of Materials Engineering

COMMITTEE MEMBER: Robert Crockett, Ph.D.
Professor of Biomedical Engineering

COMMITTEE MEMBER: Lanny Griffin, Ph.D.
Professor of Biomedical Engineering

ABSTRACT

Superalloy Metallurgy a Gleeble Study of Environmental Fracture in Inconel 601

Alan Demmons

At temperatures above 0.5 T_m and in aggressive atmospheres predicting alloy performance is particularly challenging. Nickel alloys used in regimes where microstructure and properties are altered dynamically present unique requirements. Exposure may alter properties with unexpected early failure. The Gleeble is a valuable tool for investigation and simulation of thermo-mechanical properties of an alloy in various regimes up to the threshold of melting. In this study, four regimes of temperature and strain rate were simulated in an argon atmosphere to both investigate and document normal and abnormal failure modes. Commercial Inconel 601 was tested in selected regimes and in two treatments (as received and strain aged). Next two exposed conditions (TEOS and Hydride) were tested. Slow strain-rate and high temperature produced brittle intergranular fracture. Exposure at elevated temperature to process gases reduced both strength and ductility in both TEOS and Hydride. TEOS exposure reduced reduction in area in the alloy significantly more than the Hydride exposure.

Key Words: Superalloy, Inconel 601, Gleeble, Fracture, Environmental

ACKNOWLEDGMENTS

The author wishes to acknowledge Dr. Dan Walsh for his support and encouragement. He is not only a stellar mentor and minor deity in welding, but also a true humanitarian and friend. Dan took me in when others would drop the bar and pull the curtains. Dan's wife Jane must be recognized for her generosity of spirit and patience for without the sustenance of home and family, which she shared graciously on many memorable occasions this work would not be complete. Peg Peterson my dear friend and muse who nurtured and healed my wounds of struggle with the less gentile practitioners of the writing art. My sincere appreciation is also offered to Dr. Heidersbach whose support of students in their pursuit of dreams fueled with a thirst for new knowledge goes beyond the occasional mending of damaged self-esteem with a little Holy Water.

In our society education has come to represent opportunity. For me, obtaining a Master's degree acknowledges personal growth and a nurturing of a soul living in a community of souls. It is one small step in pursuit of my passion. At this juncture, a time of closure, it is satisfying to acknowledge that I was never alone. In addition to Dan, Jane, Peg, and Bob, I do very much appreciate and thank these other very special people.

Special recognition must be extended to Becky Powel and those persons in the Graduate Office, where they support scholarship with more than thesis editing. Their genteel encouragement, sanguine support, and gracious style are all to be emulated and admired.

Further I must give my very special thank-you to Martin Koch and Dr. Paul Rainey for the complement with FEF recognition of my abilities, wants and needs. Both Martin and Paul know the lessons of history and life. Adding to this group of supporters is Dr. Lanny Griffin who is a valued member of my review committee. These educators are passing on knowledge through thoughts and deeds to fortunate students in their classes.

Thank-you is also offered to David Gibbs, and Alan Shi. These are two, fellow graduate students who share an on-going passion and passionate desire to know. To know, not just cram enough to pass a test but to master the inclusive subjects supporting and incorporated within metallurgy and materials. Together we pursued multifaceted ideas of the engineering science in ways that nurtured mutual intellectual growth.

Finally, I would like to acknowledge the support of my son Patrick, my Mother, my adopted brother Donald Okano, my brother John Sutton, Karen (horses, donkey dogs, cats, et al) and others in my extended family for their sympathetic

forbearance. They all picked up the slack levied by my ambition to pursue a passion for metallurgy. The loss of my presence and income during an important time of their lives brought elements of student life with want or indigence to them all. Their collective sacrifices made in my behalf can only be repaid in-kind, with love.

I also dedicate a loving thank-you to my Grandfathers, Lester and Bion and my Father Wesley for their combined support, sacrifice, and love are the rock solid foundation of the Demmons family upon which I could rely to guide me. From these men I learned the meaning of to be a man and the values of Duty, Honor, and Country.

In conclusion, I have too many associates to thank individually. So if unnamed please know that your fellowship and scholarship is treasured.

TABLE OF CONTENTS

Page

LIST OF TABLES xi

LIST OF FIGURES xii

CHAPTER

1. SUPERALLOYS 1

1.1 Introduction 1

1.2 Preview 6

2. OBJECTIVE 8

3. ALLOY DEVELOPMENT 9

3.1 Alloy Processing 12

3.2 Alloy Evolution 15

3.3 Metallurgical Alloy Theory 18

3.4 The Solid State 20

3.5 Gamma Matrix (γ) 23

3.6 Gamma Prime (γ') 25

3.7 Carbides 31

3.8 Borides 32

3.9 Topologically-Close Packed (TCP) Phases 33

3.10 Mechanical Metallurgy 33

3.11 Dislocations 34

3.12 Burgers' Vector 37

3.13 Edge Dislocation 37

3.14 Screw Dislocations 38

3.15 Grain Boundaries 40

3.16 Twin Boundaries 40

3.17 Deformation 42

3.18 Stage I. Easy–Glide 43

3.19 Stage II. Linear–Hardening 44

3.20 Stage III. Cross–Slip 45

3.21 Mechanical Tests 47

3.22 Creep 49

3.23 Larson–Miller 54

4. GLEEBLE TESTING 59

4.1 Procedure 59

4.2 Gleeble General 60

4.3 Computer Interface 61

4.4 Mechanical Control 62

4.5 Heating 64

4.6 Chemistry 65

4.7 Gleeble Test Samples 67

4.8 Fracture and Microstructure 68

4.9 Imaging 69

4.10 Electronic Characterization 69

5. RESULTS AND DISCUSSION 72

5.1 Introduction 72

5.2 Rod and Plate Test Results 74

5.3 Plane Stress Test Results 79

5.4 Service Conditioned Specimen Test Results 83

5.5 OLM Microstructure and Grain Size 86

5.6 Flow and Fracture Discussion 90

5.7 SEM Fractography 110

5.8 Overview 122

5.9 TEOS and Hydride 126

5.10 Closure 133

6. CONCLUSION..... 136

6.1 Data and Testing..... 136

6.2 Environmental..... 137

6.3 Fractography..... 138

BIBLIOGRAPHY..... 139

LIST OF TABLES

Table Page

1. Composition and designation changes in alloy 8XX 16

2. Typical composition of alloy 803 and alloy 800HT 17

3. Common nickel base alloy constituents 20

4. Phases in nickel base alloys and year of discovery[1] 22

5. Strengthening potency of solid-solution elements-atom % 25

6. Inconel 601 nominal chemistry 66/75

7. Test result inconel 601 plate, as received, test temperature

1024 ^{o}F (551 ^{o}C) 76

8. Test results inconel 601 rod, strain-aged, test temperature

1024 ^{o}F (551 ^{o}C) 77

9. Plain stress test results, inconel 601 plate, gun drilled

center 80

10. Test results inconel 601 plate, teos conditioning 84

11. Test results inconel 601 plate, hydride conditioning 85

12. Chronological list of key publications, authors, and topics 98

LIST OF FIGURES

Figure Page

1. 10,000-Hour stress rupture development chronology 10

2. Face centered cubic unit cell and ABC layers of close packed planes 21

3. Morphologies of gamma prime in astroloy[13] 27

4. Dendritic morphology of gamma prime (size 400 nm to 6μm)[13] 27

5. Nominal composition of gamma prime, inconel 713C 28

6. Phase stability in Ni-X-Al ternary alloys 29

7. Equation for theory of ostwald ripening[1] 30

8. MC decomposition to $M_{23}C_6$ or M_6C [1] 32

9. Illustration of dislocation multiplication, frank-reed source [85] 38

10. Illustrates the intersection of dislocations leaving a “jog” 39

11. Three stages of dislocation movement found in fcc materials, only stages two and three are observed in polycrystals[16] 43

12. Cross slip, dislocations piled up against an obstacle give rise to hardening 46

13. Ashby deformation map for creep—often leading to an increase in strength 49

14. Basic creep curve[15] 50

15. Development of dorn and weertman creep model 51

16. Power law creep model 52

17. The stress exponent n in power law vs. stress—iso-temperature ^{o}K 53

18. Larson—miller parameter for creep rupture 54

19. Development of the larson-miller parameter[24] 55

20. Larson—miller testing time and temperature relative to actual conditions[24] 56

21. Typical larson-miller parameter alloy plot 57

22. Gleeble isolation tank with sample under test 63

23. Typical gleeble tensile bar with thermocouples attached by percussion bonding 67

24. Typical sectioning “A” & “B” illustrating direction of mounting of metallographic samples 68

25. Regression formula for estimating gamma prime solvus.[83,84] 76

26. Plot, rod GDH plane stress – ultimate load vs. temperature 81

27. Plot, rod GDH, reduction in area vs. strain rate, temperature 1023 ^{o}F 82

28. Plot, plane stress ductility dip, reduction in area % 0.5 in/in strain rate 82

29. Microstructure, rod as polished, 200 X 86

30. Microstructure, rod etched, kallings, 500 X 87

31. Feature measurement/orientation, buehler image analyzer 87

32. Bit-plane separation of elongated sulfur inclusions (blue & red) 88

33. Plate etched for image analysis of grain size, 100 X 88

34. Typical field of bit plane separation used for grain size 89

35. Results of grain size measurement of plate (5 fields) 89

36. Dimensional ranges of different classes of defects and imaging methods[29] 92

37. Schematic drawing of the effect of temperature and strain rate on yield strength in inconel X-750[66] 97

38. Void formation thru element clusters and vacancy annihilation 101

39. Schematic of cavity formation in big fracture w-type, r-type, and intermediate..... 102

40. Sulfur influence on ductility with temperature 103

41. Solute flow direction in notch stress field h-position of maximum hydrostatic stress, t-crack tip, f-crack face 106

42. Schematic representation of the rate of nucleation and growth in a condensed phase, after Doremus R.H.[32] 107

43. Dominant flow mechanisms related to stress and strain rate (arbitrary units)[69]..... 108

44. Strain-rate dependence of flow-stress for C263, a nickel base superalloy, data from tensile and torsion tests, correlation using Von Mises criterion[78] 110

45. Fully ductile equiaxed dimples clearly illustrating particles associated with nucleation of the dimples,[27] (rod, 0.0005 sr 1022 ^{o}F)..... 111

46. Shear dimples observed at a distance half way between the central equiaxed fracture zone and the sample edge,[27] (rod, 0.0005 sr, 1022 ^{o}F)..... 112

47. Elongated shear dimples illustrating ligament stretching of dimples located in the shear lip near the edge of the tensile specimen,[27] (rod, 0.0005 sr, 1022 ^{o}F)..... 112

48. Intergranular fracture 40X (hydride, 0.00005 sr, 1295 ^{o}F) 113

49. Intergranular fracture at higher magnification 100X, arrow points to possible w-crack surface, (hydride 0.00005 sr, 1295 ^{O}F) 113

50. Ductile fracture with duplex void size and an area of ridging 114

51. Ductile fracture with duplex (large and small) voids at higher magnification, arrow points to texture in a large void due to streatching[27,30] 114

52. IGF initiated at what appears to be carbides, (teos 0.00005 sr, 1292 ^{O}F) 115

53. Mixed mode fracture, note the fracture following straight twin-boundary fracture and very fine VC[33] r-type and an igf at a triple point due to grain boundary sliding boundary–w-type, typical of intermediate stress, moderate strain-rate, and temperature[33] 115

54. Smooth featureless fracture for what appears to be an igf at a triple point separation due to GB sliding 116

55. Transgranular fracture with quasi-cleavage along slip bands and tear ridges with locally micro ductility at MVC and very fine precipitates (carbides or gamma prime) 116

56. Mixed mode fracture, illustrating very fine ig void coalescence and cleavage, this fracture has local ductility but is brittle on a macro scale [26,27,33] 117

57. Transgranular fracture where slip traces show a flow distorted grain 117

58. Transgranular fracture with markedly different micro-void sizes, arrow indicates tear ridges..... 118

59. Region below arrow in figure 58, note the large difference in micro void size 118

60. Central region of figure 58 showing the hyperfine void coalescence (10,000X), note the very fine second phase particles (carbides & sulphides) where the voids are nucleating..... 119

61. Possibly large M_6C secondary carbide morphology nucleating separation and fracture, note elongated shear dimples..... 119

62. Repeat of figure 59 to emphasize mixed mode fracture with with duplex mv size, in the central area are tear ridges of small mvc following slip bands with fracture either around gamma prime ppt. or carbides, typical of intermediate strain-rate and intermediate temperature 120

63. Transgranular fracture with multiple void sizes and what appear to be facets initiated at twin-boundaries 120

64. Mixed mode fracture with about equal amounts of igf and transgranular mvc with fracture initiating along steps in slip bands, teos 0.5 strain rate, temperature 1195 ^{o}F – fast strain rate at high temperature 121

65. Mixed mode fracture with more igf and finer mv and tear ridges than the previous figure, teos, 0.005 strain rate, temperature 1195 ^{o}F – intermediate strain rate at high temperature 121

66. IGF with smooth gb surfaces or very, very fine mvc, w-voids are found at flat triple point intersections and evidence of fracture initiation along twin-boundaries, teos, 0.00005 strain rate, temperature 1195 ^{o}F 122

67. TTT diagram (c-curve) γ' and carbide formation nickel alloy 617, (report ASME B & PV code section III, 2013) 123

68. Illustrations of various mechanisms of dislocation contributions to flow[77, 82] 125

69. Plots, gleeble stroke vs. load at 1295 ^{o} F, 3 strain rates, hydride..... 127

70. Plots, gleeble stroke vs. load at 1295 ^{o}F, 3 strain rates, teos..... 127

71. Schematic diagram illustrating mechanisms proposed by Hippsley C.A., for high temperature brittle intergranular failure in austenitic steels when damage rate is slow, A and B above, show the transition to intergranular micro void coalescence (mvc) 129

72. Role of nitrogen and sulfur in formation of slip bands 130

73. Plots of load at proportional limit vs. strain rate – hydride and teos..... 130

74. Plots load at ultimate vs. temperature – hydride..... 131

75. Plots load at ultimate vs. temperature – teos..... 131

76. Plots of reduction in area vs. strain rate – teos and hydride 132

Chapter 1

SUPERALLOYS

1.1 Introduction

Physical and mechanical properties of metal alloys for high temperature application as currently constituted are the result of an intensive effort of study and development. Of particularly marked importance to the success of many technologies requiring operation of machinery at elevated temperature is the modern characterization of mechanical behavior of metals at elevated temperature.[2] Use temperatures as high as 0.8 T_m are now possible.[1,5] These high use temperatures derive from our ability to test, interpret, and model the metallurgical properties of an alloy for the load, strain rate and temperature regimes likely to be encountered during operation. Ensuring reliable performance is the challenge for engineering and design. Meeting requisite needs of extreme applications has not always resulted in satisfactory performance.

The history of turbine development is filled with stories chronicling events that push the limits of technology. Superalloy metallurgy is one example where engineers in one field were aided by the success of pioneers in another field. The genesis of aircraft performance and success of the turbine power plant are a story underwritten by failure followed by advancement in metallurgy. In 1937, the first jet airplane to fly was powered by Hans von Ohain's turbine engine. Peak operating temperature of the turbine was 1300 ^oF.[22] This 1300^oF peak operating temperature

was a function of the properties of the available austenitic alloys and those properties effectively limited turbine performance. Thermodynamic performance of the turbine is based upon the Brayton cycle. The thermodynamic principle of the Brayton cycle holds that higher use temperatures (accompanied by lower heat rejection temperatures) result in more efficient operation.

In 1937, the crucial limiting factor to higher performance was the structural integrity of hot section components. Too little was known about mechanical behavior of metal alloys at the higher operating temperatures necessary for efficiency gains from higher temperature turbine operation. Superalloys evolved to satisfy the design demands for hot strength, ductility, fatigue life, and hot-corrosion resistance at the ever higher and higher temperatures required to improve performance. Parts in the hot section of the engine like combustor, blades, vanes, and case improved with alloy design. Underpinning turbine evolution was the advancement of metallurgical science. The term “superalloy” was first used shortly after World War II. Superalloy applies to the alloys developed for use in turbo-superchargers and aircraft turbine engines, which required advanced metallurgical performance at elevated temperatures.[5] Some of the alloys for turbo-superchargers were the result of a coalition development effort between Sanford Moss of Cornell, the General Electric Company and the U.S. Army.[1] Advances in aircraft alloy development have also benefited the power and transportation industries which applied turbines to electricity production, gas-line pumping, furnace parts and primemovers.[5]

After fifty years of progress the metallurgical frontiers of hot-strength, and hot-gas corrosion resistance are still moving forward, but at a slower rate due to reduced funding for development projects here to for supported by DOD, DOE and NASA.

Metallurgical development of superalloys was an extension of the early work on austenitic stainless steel. During the period of 1910-1915, chance observations by H. Brearley in England and E. Maure on Germany led to the discovery of austenitic stainless steel.[2] Gamma (FCC) iron became the phase structure of great interest and ultimately the phase upon which superalloys were developed. These early iron base alloys were created with varying amounts of chromium and nickel as the principle constituents. Commercialization of chromium rich iron base alloys suffered because of their tendency to be brittle caused principally by the presence of massive carbides. Evolution of successful commercial alloys of iron and chromium was dependent upon low carbon ferrochrome first made available in commercial quantities in 1896 by the Goldschmidt process which reduced chromium oxide with aluminum powder.[2] Aluminum powder in the early twentieth-century was still in limited supply. By 1914, the Krupp Works, in Essen Germany where Maure worked, had successfully developed and was selling ever increasing amounts of their V2A alloy (20% Cr-7%Ni-0.25%C-bal Fe) to the chemical industry.[2] During this early period and continuing into the 1930's, intense metallurgical development gradually created the body of information which established the various grades of stainless steel available today.

Earliest methods for strengthening the austenitic alloys during alloy processing included:

- Substitutional Solid Solution
- Cold Work
- Dispersed Carbides

Applying these approaches to alloy strengthening generally resulted in adding more and more of the refractory constituent in vogue at the time. The end result was either an austenitic or ferrite matrix loaded with substitutional alloy constituents. Stability and balance between the carbides and matrix were poorly understood. Also elusive was a grasp of chemical thermodynamics of the phases at increased temperatures. Alloy designers established various ratios for alloy constituents in an attempt to optimize the delicate balance between the matrix strength and amounts of various carbide phases.[1] The outcome was a metallurgical balancing act that achieved some ad-hoc success, but often failed when an increase in operating temperature was required. Clearly the alloys were unstable. Investigation of the failures identified previously unknown phases with a concomitant advance in knowledge of alloys. Turbine engine development and metallurgy formed a strong partnership for advancing the science of both disciplines.

Three broad classes of Superalloys emerged from the work: Iron-base, Nickel-base and Cobalt-base.[1,5,11] These are austenitic alloy groups that are identified as Superalloys today. Due to outstanding high temperature mechanical

stability and corrosion performance, Nickel base alloys predominate. However, in specific environments and for cost considerations Iron and Cobalt base alloys are valued. The end of the 1960's concluded establishment of basic alloy formulations. Examples of some of the generic wrought nickel alloys of today are: 600, 601, 617, 800, 706, 718, 750, 188, Waspaloy, 80A, and HX. Further, the groundwork had been laid for formulation of the precursor alloys of the more exotic cast nickel alloys: i.e., IN-713, IN-100, IN-939 and IN-738.[10] Modern turbines require components cast, forged or sintered to achieve the properties that provide for extended safe reliable service.

The key to understanding the metallurgy of superalloys as a class has been discerning chemical composition in terms of the metallurgical phases and phase stability. How increasing temperature and sophisticated thermomechanical relationships affect dynamic changes to microstructure are crucial to making the components.

It is further necessary to know how the microstructure ultimately affects mechanical and physical properties. Engineering science rests upon mathematical characterization of how alloy properties change with regimes of operating temperature.[1] Clearly as the mechanical engineering designs asked for more power with higher temperature strength from the material, metallurgy responded with improved alloy theory. Hand-in-hand with improvements in alloy theory were development of means and methods of sophisticated mechanical and metallurgical processing and characterization. Some theories, like dislocation movement during mechanical deformation, could not advance without the ability to

view the microstructure and the changes that occur in microstructure with increasing temperature and stress. Invention of both the transmission electron microscopy and the scanning electron microscopy was vital to the advancement of metallurgical theory for Superalloys. Both imaging systems were key to visual elucidation of the interaction between precipitation of Gamma-prime and Gamma-double-prime, the phases responsible for strength and vacancy deformation structure undergoing strain. Small hyperfine precipitates effecting hot-strength and ductility were not detectable by ordinary light microscopy.[20]

This thesis reports the results of thermo-mechanical tests of a nickel base superalloy. The tests were accomplished using the HAZ 1000 testing machine (The Gleeble).[6] Microstructure before and after testing, were related to this performance. Motivation for the study was to provide data needed for insight into potential causes of muffle plate failures experienced by a leading maker of vapor deposition furnaces used in the microelectronics field. As noted above, superalloy metallurgy and engineering is rich in mechanical analysis, chemistry, and solid-state physics crucial to advancing the science of metallurgy. In this thesis, only those topics supporting an understanding of nickel base alloys in general and interpreting the tests of Inconel 601 in particular will be developed.

1.2 Preview

Engineering skill combines fundamental science with the practical. This thesis used investigation of what, how, and why of brittle intergranular fracture

(BIG) in Inconel 601 as the mode of professional development. Metallurgical engineering science applies both the, *learn by doing,* and *progress through failure* paradigms. Chapter one, summarized importance of superalloy applications and development of the essential requirements driving development of metallurgy and superalloy theory.

This short summary is by no means comprehensive for the field of study is vast. Similarly, chapter three traces development of elements of superalloy theory and essential metallurgy germane to this study. An overview of the thermo-mechanical test platform, The Gleeble, was presented in chapter four. Chapter five, contains the data from Gleeble tests and complementary SEM observations. Conclusions, pulling together theory and observations for why are the core of chapter six.

Chapter 2

OBJECTIVE

Learn by doing – to – Doing is knowing

The objective of this study was to determine why Inconel 601 did not last as planned in a no load muffle plate furnace design. In use the alloy was held at elevated temperature and exposed to semiconductor process gas. Two process conditions TEOS and Hydride were identified. In both exposures BIG fractures were reported. This objective will be achieved through physical simulation of the thermomechanical environment in baseline samples. Results from baseline tests will then be compared to test samples of process exposed material in parallel thermomechanical regimes. Well controlled testing will highlight effects of exposure of the alloy to semiconductor processing gases.

Chapter 3

ALLOY DEVELOPMENT

Decades of intense work with contributions from many groups developed the modern nickel-base superalloys.[8] Nickel base superalloy progress is a model of the engineering paradigm where the path to improvement is built upon the understanding of failure. Composition of each superalloy tends to be highly specific to the end use. Constituents in many of the commercial alloys are proprietary and patented. Alloy formulations were aimed to satisfying a bill of particulars of relevant properties at a temperature predetermined by design. In general, an alloy for use at high temperature must have: creep resistance, fatigue resistance, thermal-shock resistance, fracture toughness, oxidation and hot-corrosion resistance, and a high stress rupture strength.[1,5,11] Mechanical testing and metallurgical theory attacked the mechanical engineering design problem from many different directions. Theories using microstructure, solution chemistry and crystal deformation addressing material properties were developed. Mechanical tests were developed to effectively characterize, model and compare alloy performance as determined by new and refined design criterion. Tests for mechanical characterization of an alloy were part of the co-evolutionary process of superalloy development. Alloy processing, metallurgical structure and

mechanical metallurgy all played equally critical roles in furthering the goals of the superalloy design paradigm.

Early success with alloys intended to operate at temperatures above 0.6 T_m appeared to be more black art than science. Superalloys operate in extremely hostile environments, at high fractions of the alloy homologous temperature, which was an entirely new domain to metallurgists. The stress rupture performance of selected alloys is shown schematically in Figure 1. The figure illustrates the achievements in increasing strength as defined by the 10,000-hour stress rupture value at 1600 ^oF. During the decades illustrated, one sees clearly the reversals, plateaus, and periods of steady incremental increase.

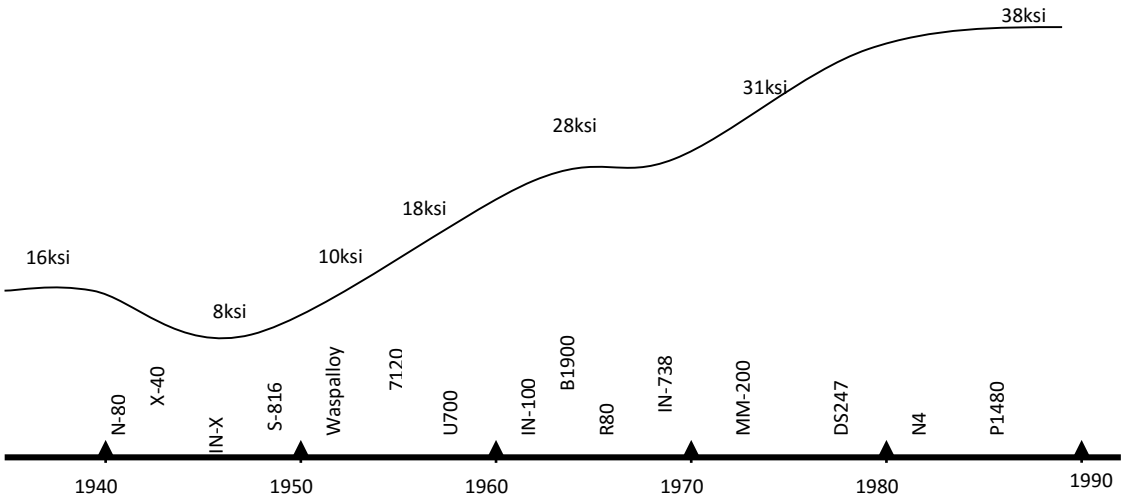

Figure 1. 10,000-Hour stress rupture development chronology

A complete treatise documenting the history of development of superalloys is far beyond the scope of this thesis. However, a discussion of the factors

essential to the performance of Inconel 601 and to the evaluation of Inconel 601 in a key application is warranted. Elements for discussion fall within the broad topics of:

- Alloy Processing
- Metallurgical Alloy Theory
- Mechanical Metallurgy

In considering the various aspects of alloy development one is presented with a “chicken or egg” conundrum. Which came first, insights into the role of constituents in alloying and microstructure or the improvements in processing and refinement?[5,24] No singular view represents the truly coincident and disjointed progress that characterized the advances in both processing and theory. Mechanical metallurgy acts as a capstone to processing and alloy theory. Mechanical metallurgy, in the context of this thesis, covers the integration of macroscopic testing and theories of crystal deformation; linking both the microscopic and macroscopic views of structure and test results.[5,9] In many respects the topics overlap, but an attempt will be made to separate development of nickel-base superalloy discussion along the lines identified above. This thesis presents summaries of selected essential concepts. More detail is provided for concepts directly connected to understanding and interpreting the alloy (IN 601) and the Gleeble test results in the results and discussion.

3.1 Alloy Processing

Commercial alloys start with the melt. Care exercised during alloy production often determines the success or failure of a material and design in operation. In the finished form the alloy must have uniform and predictable properties. Ideally in a primary melting and casting operation the complete process will produce a[2,10]:

- Clean uniform chemical composition
- Melt free of impurities and deleterious gasses
- Specific microstructure with a uniform grain size
- Finished product with high efficiency and low scrap
- With controllable properties and at economic cost

This ideal casting process is far from reality in the production and processing of useful parts. Processing for a given part evolves from the choice of composition. Composition has been selected to optimize a particular combination of mechanical and chemical properties. Knowing how innovative processing attains the final properties in an efficient and economical way is as important to success in superalloys as knowing which alloy achieves the desired design properties.

Some of the processing methods which evolved with superalloy production have included:

- Air melting and refinement by argon-oxygen-decarburization (AOD).[2]

- Vacuum melting in the various forms: induction melting (VIM), arc melting (VAR), electro-slag melting (ESR), electron beam melting (EBM), plasma arc melting (PAM) etc.[2,5]
- Casting methods such as, lost wax-investment casting, directional solidification, single crystals from the melt.[2]
- Forging practice innovations like superplastic forging, hot isostatic pressing of castings and powders.[1,2,5]

In each major step in metallurgical innovation, processing has been a force contributing to bring superalloys to maturity. Efficient production of the finished part drove development. An economical, reliable turbine must be built with alloys that are strong and stable at increasingly higher temperatures.

Early alloys suffered from excessive amounts of carbon, derived from carbon in the basic sources of chromium and nickel.[2] Metallurgists, limited to post process refinement by AOD (argon-oxygen-decarburization), used the higher residual carbon to advantage by alloying with carbide formers (Cr, V, W, etc.) to produce various carbides in post processing heat-treatments. MC, M_6C, and $M_{23}C_6$ in carefully balanced alloys provided one means of reaching the targeted strength.[1,2] Difficulties involved with using residual carbon for strengthening will be discussed later when deleterious effects of carbides in microstructure is considered.

Removal or minimization of oxygen and nitrogen have been the focus of alloy processing, as these elements form inclusions which degrade mechanical properties such as fracture toughness. Vacuum melting and casting achieved the necessary reduction in dissolved gasses with a spectacular increase in stress-rupture properties; stress rupture gains have been attributed to the derived ability to control grain size and segregation.[1] Vacuum melting (VIM, VAR) and electro slag refinement (ESR) served two key metallurgical objectives. First, reduction of oxygen to very low partial pressures helped to retain and control the amounts of crucial reactive constituents like aluminum and titanium. Second, vacuum induction melting (VIM) effectively removes the dissolved gasses oxygen and nitrogen as well as harmful trace elements with high vapor pressures like lead, selenium, copper, bismuth, and tellurium.[1] Refinement of trace elements like sulfur and phosphorus are more problematic. Removal of sulfur and phosphorus as volatile compounds is impractical as the reaction rates are slow.[1] Fortunately, with low oxygen levels realized by VIM, desulfurization can now be accomplished by slagging with lime (CaO).[1] Slagging has drawbacks, and thus using electrolytically refined virgin raw material with controlled low quantities of sulfur and phosphorus is preferred.

3.2 Alloy Evolution

Ganesan et al. reported the introduction of INCOLOY Alloy 803, a fourth generation superalloy, used in many applications such as heat-treating hardware, petrochemical processing, home appliances, food processing, industrial heating, super-heater and re-heater tubing. Alloy 803 is a workhorse material for the chemical processing industry in applications requiring high temperature creep strength and oxidation resistance.[12] First in the series was INCOLOY 800.

INCOLOY alloy 800, introduced in the 1940's. Modification to the composition limits and improvement in constitution processing of the 8XX alloy series typifies the evolution of chemistry and processing in superalloy metallurgy. Alloy 800 is a Fe-Ni-Cr alloy with small amounts of silicon, manganese, aluminum and titanium. In applications using Alloy 800 it was soon recognized that heats containing higher carbon levels (but within specification) had higher creep and rupture properties than lower carbon heats. For that reason, an increase in carbon range from 0.05 to 0.10% and a restriction to the total Al + Ti was adopted and designated as INCOLOY alloy 800H.[12] Gains in material strength achieved by the change in composition were acknowledged by higher approved design stresses in the ASME Code for alloy 800H. Note the ASME Code also required a grain size of ASTM 5 or coarser to meet the higher values for creep and stress rupture allowed.[12] Further study of some 87 heats (1057 data points) led to an understanding that maintaining the aluminum and titanium in the upper portions of the specified range for composition contributed to higher creep and stress rupture properties.[12] Revised limits to the composition were instituted to narrow the

allowed range led to the alloy designation INCOLOY alloy 800HT. Evolutionary composition changes to the alloy 8XX series are shown in

Table 1.

Table 1. Composition and designation changes in alloy 8XX[12]

Alloy	UNS No.	C	Al	Ti	Al+Ti
800	8800	0.10 max	0.15 to 0.60	0.15 to 0.60	none
800H	8810	0.05 to 0.10	0.15 to 0.60	0.15 to 0.60	0.30 to 1.20
800HT	8811	0.06 to 0.10	0.15 to 0.60	0.15 to 0.60	0.85 to 1.20

In addition to the changes in composition, specifications were established for the heat treatment and microstructure (larger grain size) to achieve the improved mechanical properties. To further improve the strength and gain greater carburization resistance, more Cr and Ni were added to the basic Fe—Ni—Cr formulation of alloy 800 and the fourth generation alloy 803 designated. Comparison of the composition modification is shown in Table 2.

Table 2. Typical composition of alloy 803 and alloy 800HT[12]

Alloy	C	Mn	Si	Fe	Ni	Cr	Al	Ti
803	0.07	0.92	0.71	38.6	34.4	25.6	0.49	0.62
800HT	0.07	0.90	0.21	46.3	31.2	20.0	0.49	0.58

Alloy 803 is made from virgin raw material by VIM followed by two successive ESR processes. The ingots are further refined by VAR to eliminate deleterious amounts of oxygen and nitrogen. Increased alloy and processing costs of alloy 803 are offset by the improved mechanical properties at high temperature. These improvements provide processing efficiencies as machinery can operate at higher temperature. High alloy costs have been the trade-off for other applications and processing innovations.

The investment casting (IC) process was developed to minimize material loss during machining as well as to circumvent difficulties inherent in casting and machining superalloys. IC is effective producing complex parts of near-net-shape. Elimination of premature creep failures due to cracks originating in transverse grain boundaries was attained by directional solidification. Innovation in solidification processing ultimately resulted in single crystal turbine blades.[1,5] Single crystals eliminated deleterious creep due to grain boundaries. Single crystals also allowed a reduction in total alloy by taking away those constituents normally included to

control grain-boundary sliding (W, V, Zr, B, C…). Wrought alloys are by nature polycrystalline. Alloys like the IN 601 tested are required for products that are not easily cast to shape and must be fabricated from rod, bar, sheet, or plate.

Following casting into ingots, wrought products are formed by some means of mechanical working such as forging, rolling, extruding etc., thus good hot-working properties become important. During and often following finished shaping by machining, bending, or welding, heat-treating is required to create the final microstructure. Some of the aims of heat-treating a wrought alloy are controlling finished grain size and controlling shape, size and distribution of the carbides and precipitate phases. Paralleling the innovation in metallurgical processing was improvement in metallurgical microstructure and fundamental understanding of alloy constituents. Alloy theory will be the theme of the next section.

3.3 Metallurgical Alloy Theory

Chester Sims in his book “Superalloys” characterized the combination of constituents in Superalloys as a “Chemical Stew”.[1] To many of the metallurgists working on high-temperature alloys this is an apt description of the combination of constituents they used to achieve a particular set of mechanical and physical properties. Both the system designer and alloy metallurgist know that in the severe operating environment of turbine engine hot-sections, a superalloy is a white-hot, chemically dynamic entity of constantly changing solid-state phases, just a few degrees below its melting point.[1, 4, 5, 10] Sims also says clearly,

> As in all classic equilibrium metallurgy, the alloy chemical composition defines the solid phases present. Phases, in turn, make up microstructure useful for most visual understanding of alloys in service. Thus, the chemical composition, phase constitution, and microstructure define superalloy properties in the physical sense.[1]

From Sims' statements, it is clear how composition is crucial to any discussion of a superalloy. Table 3 identifies the elements and their common purpose when used as major constituents of nickel base superalloys. This modern list of alloying elements and their function in high-temperature alloys summarize sixty-plus years researching and use of superalloys at temperatures and in environments where instability and potential failure is normal. Contributions to performance improvement came from many individuals. Researchers continue to look for methods to increase performance and life of systems; currently hot-section life limited parts reach 0.8 T_m and remain in operation 18,000 to 20,000 hours before requiring service or replacement will be helpful to consider several general ideas related to structure.

Table 3. Common nickel base alloy constituents [1,11]

Common Function	
Solid-solution strengtheners	Co, Cr, Fe, Al Mo, W, Ta
Carbide formers	
MC	W, Ta, Ti, Mo, Nb
M_7C_3	Cr
$M_{23}C_6$	Cr, Mo, W
M_6C	Mo, W
Carbonitrides: M(CN)	C, N
Forms $\gamma' Ni_3$ (Al, Ti)	Al, Ti
Lowers solvus temperature of γ'	Co
Forms hardening precipitates and/or intermetallics	Al, Ti, Nb
Oxidation resistance	Al, Cr
Improve hot corrosion resistance	La, Th
Sulfidation resistance	Cr
Improves creep properties	B
Increases rupture strength	B (in large amounts)
Causes grain-boundary segregation	B, C, Zr

3.4 The Solid State

Before developing some of the explicit microstructures found in nickel base alloys we look at Metals as crystalline solids. As such, atoms in the solid state arrange themselves into imperfect three-dimensional arrays. The three most common crystal structures in metals are body centered cubic, face centered cubic

and hexagonal close packed. Austenite, the solvent phase of a nickel base alloy, is a face centered cubic (fcc) structure; a short review of the FCC structure follows. An fcc unit cell is characterized by a cube with an atom occupying each corner of the cube and an atom in the center of each of the six faces of the cube as illustrated in Figure 2 below. Half of the atom in each face is identified with the cube of the unit cell (1/2 x6=3 atoms) and each atom in the corners of the cube is shared with eight adjacent cells (1/8 x8=1 atom). hus a unit cell consists four atoms.

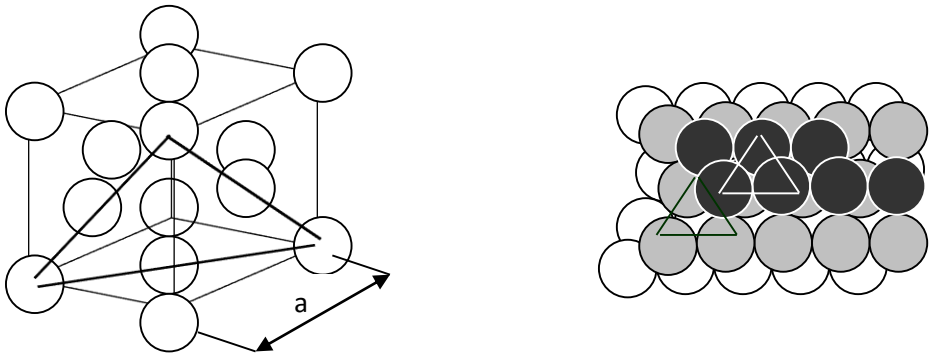

Figure 2. Face centered cubic unit cell and ABC layers of close packed planes

The FCC structure may be built up by laying down close-packed planes in a sequence ABCABC…. A stacking fault occurs if this sequence goes wrong, e.g. as in ABCBCABC…., here a layer A is missing, or sequence ABCABACABC…. in which an extra A layer has been inserted.[16] While stacking faults can in principle extend through the crystal they usually only occupy part of the plane.[9,16] Since in the region of a stacking fault the atoms do not have exactly their correct relationships to one another, there will be some extra elastic strain.[1, 14, 15, 17] This means that there will be extra surface energy associated with a stacking fault.[17]

Note that it is extremely unlikely that a stacking fault of the type AA will occur because the extra elastic energy required for such a big mismatch would be very large.[16] Stacking faults as defects in crystals will be discussed further with the topic dislocations.

Of the new phases discovered not all were harmful, some were good. Chester T Sims listed some of the key the phases discovered in characterizing the austenitic microstructures of superalloys.[1] Listed in Table 4, with the approximate year of discovery are two categories of new phases, beneficial and deleterious.

Table 4. Phases in nickel base alloys and year of discovery [1]

Approximate year of significance	Beneficial phases	Deleterious phases
pre 1940	Equiaxed ɳ	ɳ (nata) Plates
1940's	γ′ (Gamma prime)	G-phase
--	$M_{23}C_6$	Cellular $M_{23}C_6$
1950's	MC	Laves
1960's	GB γ′	Sigma
--	Eutectic	Mu
--	γ γ′	Sulfides
1970's	ODS	
1970's	Directional solidification	
--	γ′ Rafts	
1980's	Single crystals	
--	TaC fibers	
	γ γ′′	

Control the microstructure---to---control the properties.

Dan Walsh

As stated earlier, solid solution strengthening, precipitated carbides, and cold work were considered the principal means of improving the mechanical properties of nickel base alloys prior to discovery of gamma prime (γ'). Nickel base superalloys are based upon single phase austenite. Austenite designated gamma (γ) is a face center cubic crystal structure. Cold work is impractical as a means of strengthening high-temperature alloys because properties are lost due to recovery and re-crystallization well below the operating temperatures of the parts. With a cursory look at Table 4, one will notice that a lot has come to pass altering perceptions of structure and metallurgical understanding of nickel base alloys. Essential concepts of alloy structure and austenite microstructure and the gamma prime phase follow.

3.5 Gamma Matrix (γ)

The continuous matrix in nickel-base alloys at room temperature is the FCC austenitic phase hardened with a precipitation of ordered intermetallic phase called gamma. Austenite usually contains a large weight percent of solid-solution elements such as those listed in Table 3, i.e., Co, Cr, Mo, W, Al, Fe, and Ta. These

elements have various degrees of solid solubility in the austenite. Solubility and phases expressed in binary and ternary phase diagrams are an incomplete picture. The ability to represent the phase relationship of more than three elements in solution in a single diagram is a stretch beyond existing theory. Ross and Simms summarized the metallurgical problem by saying, “The very complex high-temperature solid-state reactions prevent defining chemical equations of state (with appropriate activation energies) to categorize the systems”.[1] Thus the metallurgist makes use of basic chemical principles, empirical methods, and experience to guide his choice of chemistry and quantity in a particular alloy.

The identified common solid solution elements are cobalt, iron, chromium, molybdenum, tungsten, titanium and aluminum. These elements differ from nickel by 1—13% in atomic diameter (Goldschmidt) and 1—7% in N_v . Table 5 below lists the estimated strengthening potency of solid-solution elements in atom % in a nickel matrix of γ.

Table 5. Strengthening potency of solid-solution elements-atom %

Co	Fe	Cr	Mo	W	V	Al	Ti
20	10	20	4	4	1.5	6	1

Solid solution strength effects persist to high temperatures but begin to lose potency above about 0.6 T_m. In this range diffusion becomes the dominant mode of deformation and creep much more important.[1]

3.6 Gamma Prime (γ')

The discovery of Gamma prime (γ'), in nickel base alloys and the control of its precipitation in nickel base alloys was crucial for the development superior hot-strength in superalloys. In austenitic alloys containing sufficient Aluminum and/or Titanium noteworthy secondary hardening occurs when aged at elevated temperature.[2] Optimizing properties became a matter of discovering the complex combination of elements to optimize γ' and avoid harmful phases. An increase in hardness indicates a concomitant increase in tensile and yield strength. Solid solution alloying and carbide strengthening practice were unable to account for the total increase in properties.[1, 2]

Light microscopy and x-ray diffraction are both powerful tools in metallurgical studies but they were inadequate for resolving and identifying γ'

precipitation and morphology as the phase key to the success of superalloys. The precipitate was initially isolated and identified with the Transmission Electron Microscope (TEM). Gamma prime (γ') is an ordered intermetallic compound of nominally fixed composition (e.g. A_3B, Ni_3 Al) with a $L1_2$ (ordered FCC) structure.[8] This ordered FCC structure has aluminum atoms occupying the corner sites of the unit cell cube and nickel atoms occupy the center of each face.[1, 8] Most Gamma prime in nickel-austenite has a lattice constant (a) very nearly the same as austenite (γ); for example in Udimet-700 the γ' lattice is only 0.02% greater than that of the γ matrix.[18] Thus the precipitate particles invariably occur as coherent or nearly coherent with the matrix.[1, 8] TEM studies of the morphology and coherency of γ' in Astroloy were conducted by Macia and Sanders. This investigation found the γ' particles varied from coherent for the small octet shapes produced at lower aging temperatures to partially coherent for larger dendritic particles produced at higher temperatures.[13] Discovery of the ordered inter-metallic phase gamma prime (γ′) is particularly meaningful and represents one of the marked successes of alloy development in superalloy metallurgy.

In the small volume fractions (≈ 0.1 Vol. fraction)[13] necessary for the results measured by hardness or tensile testing γ′ was not visible at magnifications available with ordinary light metallography (OLM). Gamma prime is resolved in the high energy transmission electron microscope (TEM) and the scanning electron microscope (SEM) with proper sample preparation and when examined at magnifications of 2500-10,000 X with nanometer resolution.[1] In early studies of γ′ the morphology of low temperature precipitates was generally spherical while γ′

precipitated at higher temperatures was cuboidal.[1, 13] Due to the importance of the morphology, size and distribution of the γ′ to the creep and stress rupture properties of an alloy, morphology control and characterization of the precipitate

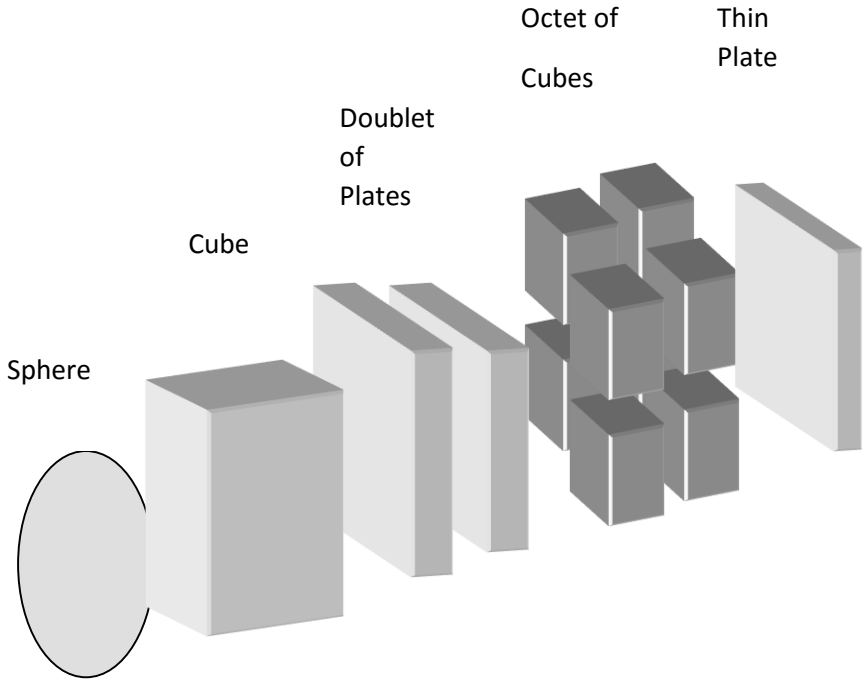

Figure 3. Morphologies of gamma prime in astroloy[13]

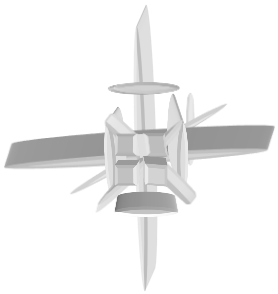

Figure 4. Dendritic morphology of gamma prime (size 400 nm to 6μm)[13]

continues to attract metallurgical attention. Figures 3 and 4 illustrate the various morphologies developed by different heat-treatment regimes of Astroloy,

reported by Macia and Sanders.[13]

Hagel and Baettie related the shape of γ′ to the degree of matrix-lattice mismatch; 0-0.2% γ′ forms spheres, 0.5—1.0% γ′ as cubes, and above 1.24% γ′ becomes plates.[1] Composition of γ′ as well as the temperature at which γ′ is formed has marked effect on the degree of lattice mismatch.

Similarities in the crystalline structure, composition and lattice constant between γ and γ′ confounded the investigations by x-ray diffraction of solid or powdered samples.[17] Using extraction methods it is possible to more carefully characterize the γ′ found in various alloys. With an extraction method Mihalisin and Pasquine determined the composition of γ' from Incoloy 713C to be,

$$\mathbf{(}Ni_{0.980}Cr_{0.016}Mo_{0.004}\mathbf{)}_3\ \mathbf{(}Al_{0.714}Cb_{-0.009}Ti_{0.048}\ Mo_{0.038}Cr_{0.103}\mathbf{)}.\ ^{1}$$

$\mathbf{(}\ A\ \mathbf{)}_3\ \mathbf{(}\ B\ \mathbf{)}$ is the nominal chemical formula of γ'

Figure 5. Nominal composition of gamma prime, inconel 713C

Notice that chromium is found as a substitute for either nickel or aluminum in the intermetallic lattice, with greater substitution for aluminum than nickel. This effect is attributed to the atomic size of chromium.[1]

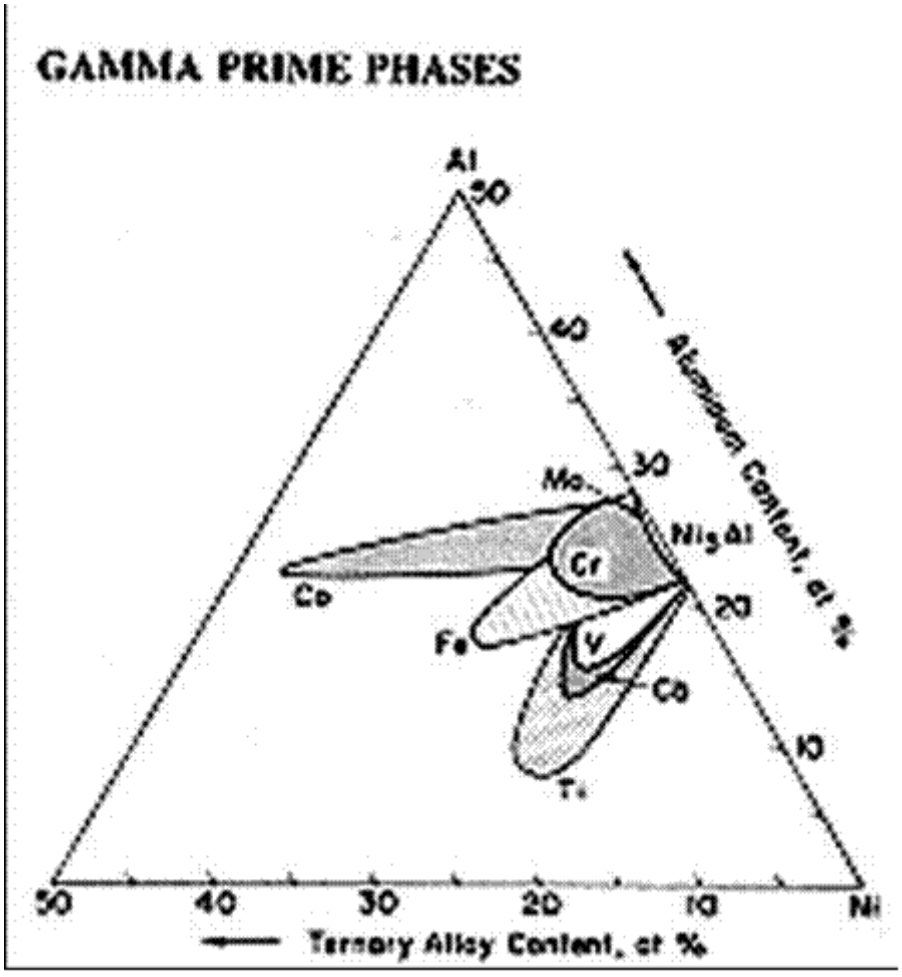

Figure 6. Phase stability in Ni-X-Al ternary alloys

Other elements will substitute into the γ' as shown schematically by the relative thermodynamic stability indicated in Figure 6 plotting superimposed phase fields of the indicated elements on the Ni-X-Al ternary phase diagram.[1] Accordingly, complex relationships are found in the γ' of a nickel-base alloy. Loomis et al. have shown that molybdenum has extensive solubility in the γ' of a titanium free alloy.[19]

Size and dispersion of γ′ in the γ matrix has a marked effect on creep and stress rupture values, therefore operating temperature and degree of saturation both concern the metallurgist in specifying heat-treatments. Temperatures above

0.6 T_m cause the γ′ to increase in size by a process known as Ostwald Ripening.[1,8] Fleetwood's formulation of Ostwald ripening of γ′ illustrates the key variables.

$$h^3 = \frac{64\gamma_e D C_e V_m^2 t}{9RT}$$

Where

t = time

γ_e = Specific γ′-- γ interfacial free energy

D = coefficient of diffusion of γ′ solutes in γ

C_e = equilibrium molar concentration of γ′ solute in γ

V_m = molar volume of γ′

R = gas constant

h = particle size

T = Kelvin Temperature

Figure 7. Equation for theory of ostwald ripening[1]

Volume percent γ′ markedly effects strength and stability of the microstructure. In Ni—Cr—Ti—Al alloys an increase in chromium (10—37%) has been found to decrease the ripening rate.[1] Cobalt is known to lower the γ′ solves temperature and retard ripening.[8] Similarly additions of refractory elements with slow diffusion rates and high melting points like molybdenum and tungsten will significantly retard the rate of γ′ ripening.[1] Overall the approach to forestall ripening is two fold: (1) increase the volume percent of γ′ and (2) add high

partitioning, slow-diffusing elements such as columbium and tantalum or molybdenum and tungsten. Tien and Copley observed rafting of γ′ due to the influence of uniaxial stresses during stress annealing but did not offer a reason for how applied stress effected coarsening.[18]

The important concept of how the γ′ precipitates interact with dislocation movement responsible for observed properties of flow will be differed until after dislocations are discussed.

3.7 Carbides

Above about 0.05—0.2% additions of carbon exceeds austenitic solubility and combine with reactive and refractory elements (Ti, Hf, Ta) to form MC carbides in the melt. At elevated temperature during heat-treatment or during service the MC carbides decompose forming lower carbides like $M_{23}C_6$ and M_6C.[1] MC carbides from the melt are generally small and dispersed heterogeneously in the matrix while lower carbides tend to populate the grain boundaries in nickel alloys. Additions of cobalt and iron cause a marked shift to intergranular sites for carbide precipitation. At well controlled volume fractions grain-boundary carbides reduce creep, but with carbides as a continuous grain-boundary phase an alloy is brittle. Furthermore, deleterious Topologically-Close-Packed (TCP) phases (σ or μ) can nucleate on the $M_{23}C_6$ carbides. Formation of $M_{23}C_6$ carbides in the grain boundary depletes chromium from the matrix and the solubility of γ′ near the grain boundary is raised. The loss of chromium and γ′ denudes the near the grain

boundaries regions reducing strength and contributing the susceptibility of the boundaries to corrosion.[1] Thus there is some controversy with opinions associated with the location, amount and purpose of carbides in these alloys.

MC carbide in the matrix adds strengthened at elevated temperatures. During heat-treatment or service the MC decomposes slowly, acting as a source of carbon, permeating the alloy and triggering the reactions shown in figure 8.

MC Decomposition to $M_{23}C_6$ [1]

$$MC + \gamma \rightarrow M_{23}C_6 + \gamma'$$

$$MC + \gamma \rightarrow M_6C + \gamma'$$

Figure 8. MC decomposition to $M_{23}C_6$ or M_6C[1]

As the MC carbides decompose the matrix loss in strength is offset by γ′ precipitation. In certain alloys M_6C can form from $M_{23}C_6$ and vice versa.

3.8 Borides

Until just recently boron additions to superalloys in amounts of 50—500 ppm were considered essential to controlling grain–boundary precipitation presumably by reducing diffusion rates.[1] Boron in the grain-boundary has also been shown to block the onset of tearing under creep rupture loading.[11, 15] However, recent studies of welding metallurgy of investment cast nickel-based superalloys showed that the boron content at higher levels were associated with heat-affected-zone cracking. However, the mechanism is not yet understood.[21] Current practice restricts boron additions to the range of 50—200 ppm.

3.9 Topologically-Close Packed (TCP) Phases

For the most part TPC phases are undesirable structures that precipitate in certain alloys during heat-treatment or during service. These precipitates are characterized by the close-packed layers of atoms forming in “basket weave” nets aligned with the octahedral planes of the FCC matrix.[1] They appear as thin linear plates, often nucleating on grain boundary carbides.[1] Common TCP phases found in nickel base alloys are σ and μ.

Two important metallurgical tools were developed while studying the evolution and control of TCP phases in superalloys. Polar phase diagrams and Phase Composition (PhaseComp) programs both were created to predict TCP formation and aid in their prevention. These two tools continue as valuable cornerstones in predicting complex constituent solubility and phase stability.[1] They are keys to setting proper limits in constituent constitution in modern alloy formulation.

3.10 Mechanical Metallurgy

Previous discussions of alloy metallurgy and processing were presented as a bridge between the twin towers of knowledge shaping the mechanical metallurgy of superalloys. Microstructure as observed with OLM, SEM, and TEM, links macroscopic properties with microscopic structure. The superalloy metallurgist must have a familiarity at both scales to solve the engineering problems integral to

high-temperature applications. This discussion introduces the essential concepts of deformation at the microscopic level. It then relates this to results of macroscopic tests used to discover key engineering properties of the materials studied. For the macroscopic tests, many variables are important. These include stress, strain, strain-rate, temperature, and temperature gradient experienced by alloy in high-temperature applications. At the microscopic level, flow and fracture can be explained through chemistry, crystal structure, and dislocation movement. Further complex interaction of these elements and defects determine properties. Dislocations explain how metal crystal structure serves as the stage upon which defects play to determine deformation and fracture behavior. From the macroscopic view, practical mechanical tests are used to quantify and model material properties in various conditions. Bulk properties are linked to the crystal in field theory. However, it must be acknowledged there remains a gap between the two-scaled domains.

3.11 Dislocations

Mechanisms of crystal deformation in metals is a vital issue in the study of mechanical metallurgy. Elementary estimates of flow stress of a metal, based upon atom to atom bond energy and crystal structure, over estimate strength by a factor of 100 to 100,000 when compared to actual tests.[15] This disparity between theoretical yield strength and the measured yield strength made it clear that improved theory of mechanics was needed to predict yield, flow and fracture in any useful way. Modern dislocation theory was suggested independently in 1934 by

Taylor, Orwin, and Polanyi, in order to account for the observed strength of crystals….. particularly metals.[14,16,17] Observations from microscopic investigations suggested that when a metal crystal (or polycrystals), is plastically deformed the deformation occurs by the slip of one atom over another. This occurs not as a unit but thru the shift of a defect, bond-to-bond. In modern terms this motion is known as glide.[14, 15, 16, 17] By 1950, dislocation theory was well developed. When comparing regimes of theoretical flow stress and creep, Earl R. Parker wrote, “dislocation theory on the other hand, suggests a mechanism of slip in which the atomic forces are overcome a few at a time, and can thus account for the low values observed for the yield strength of metallic single crystals.”[15] In succeeding years, dislocation theory has fully matured to become the dominant means of describing flow and fracture in crystalline metals. In the broadest terms, a dislocation is a linear flaw in a crystal lattice; moving in stress fields at lower temperature (0.6 T_m). Methods for studying dislocations and some key concepts of dislocation formation and movement follow.

Early x-ray study allowed the crystal structures of metal matrix phases, and constituent phases to be discerned. This formed the basis for imaginative researchers to develop theory of dislocations to explain deformation in crystalline materials. Real confirmation of theory came with invention of the electron microscope.[16] In extremely thin (0.1 μm) specimens used in TEM studies, rotation of the sample in the electron beam cause variations in contrast due to changes in the diffraction pattern resulting from the presence of dislocations.[16, 17] The patterns provide an indirect image of the dislocation defect structure. In some favorable

situations heat from the electron beam is sufficient to vary the stress, allowing motion and interaction of the dislocations to be observed.[16] Direct observation provides confirmation and powerful insights to atomic structure. A few of the other detection techniques used to study dislocations are:

1. X-ray topography in nearly perfect crystals with a low dislocation density.
2. X-ray line broadening in work-hardened specimens with high dislocation density.
3. Etch pits are used to reveal dislocations which end at the surface of the crystal.
4. Field-ion microscopy used to image atoms located at the tip of a fine needle.
5. Decoration techniques used to study dislocation networks by preferential segregation of impurities around dislocations.

Because of the number of dislocations (density) observed in different orientations, which may occur in the crystal, the patterns revealed by the various methods of study are complex. In their extremes, two basic forms of dislocation are believed to exist, the edge dislocation and the screw dislocation.[9] These are line defects in the crystal structure which may occur individually, but are typically found as mixed dislocations which are combinations of both edge and screw dislocations (and at times as incomplete or partial dislocations).[14, 25] Careful measurement of spacing between planes of atoms by x-ray and electron diffraction were pivotal in these determinations.[14, 16, 17]

3.12 Burgers' Vector

Burgers' Vector is the term used to distinguish the dislocation types and quantify the amount of mismatch in the crystal. The Burger' Vector (b) is defined as the length and direction of the line segment (vector) required to complete an atom-to-atom path outlining the defect. When the vector lies in and moves within the plane of the crystal mismatch the dislocation is an edge dislocation.[16, 17] A Burgers Vector perpendicular to the orientation of slip is characteristic of a screw dislocation.[16, 17]

3.13 Edge Dislocation

An edge dislocation is a line defect in a lattice which represents the simplest dislocation defect used to describe how defect movement can account for changes within the crystal.[15] Edge dislocations are either added or missing planes of atoms and as such represent either extrinsic or intrinsic stacking faults respectively.[9,14,15,16,17,25] Additional or missing atom planes represent stacking faults in another wise perfect crystal.[14, 16, 17] While stacking faults can in principle extend through the crystal they usually only occupy part of the crystal plane.[16,17] Edge dislocations move in the direction of the Burgers' Vector under the influence of shear stress. If a coherent precipitate e.g. (Ni_3Al in γ) blocks the movement of an edge dislocation the dislocation must either cut through the precipitate or climb around. When the motion of an edge dislocation becomes pinned at two points it can multiply by means of a Frank-Read source.[9, 17]

The heavy red line identifies a dislocation on plane A, which moves by shear stress, to cross slip on plane B and again on A, where it bows out to become a Frank-Read source of increased dislocation line length and new dislocations.[17, 85]

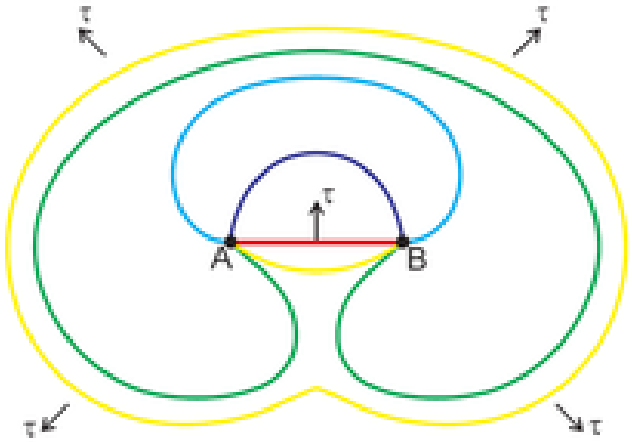

Figure 9. Illustration of dislocation multiplication, frank-reed source [85]

3.14 Screw Dislocations

It is characteristic of a screw dislocation that the Burgers' Vector lies parallel to the dislocation line and slips perpendicular to the Burgers' Vector.[14] A path around the dislocation in the crystal traces a spiral in which one revolution advances a distance of the Burgers' Vector.[17] Confirmation of screw dislocations is found in growth spirals seen in natural crystal faces of crystals like silicon carbide, magnesium, PbI_2 and CdI_2.[17] Obstacles like a precipitate can block the

slip movement of screw dislocations. If the stress is increased sufficiently, screw dislocations can cross slip and continue to slip via an intersecting plane which is parallel to the main slip plane.[14] Sense of the b identifies a positive or negative dislocation. Like dislocations repel and dislocations of opposite sense will attract and can annihilate each other if they meet on the same plane restoring order to the crystal structure. A complete synopsis of dislocation action is beyond the scope of this review.

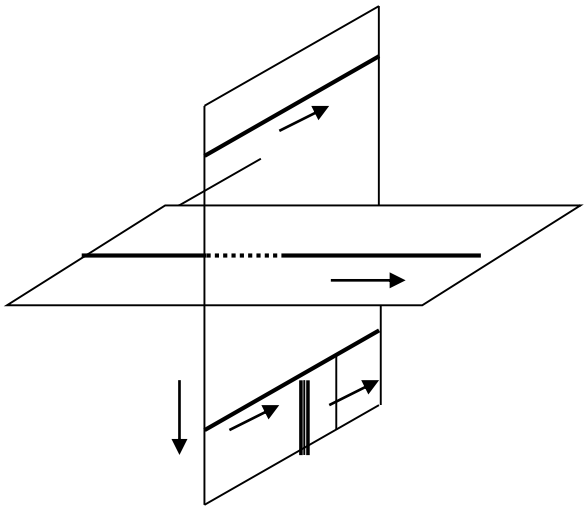

Figure 10. Illustrates the intersection of dislocations leaving a “jog”

The intersection of dislocations can leave a ‘jog’ on either or both of them, as illustrated in figure 10. Depending on the Burger’ Vectors of the dislocations, the motion of the jog can be either conservative or non-conservative depending upon whether it moves by slip or diffusion.[16,17] For the intersection of two edge dislocations shown here, the jog will have a non-conservative motion as it is moved downward in a manner that constitutes a drag on the dislocation motion.[16]

Features, such as grain boundaries and fracture surfaces, of metal crystal structure observed in the light microscope are also explained by dislocation structure.

3.15 Grain Boundaries

Most engineering materials are polycrystalline with randomly oriented grains. The interfaces between grains, which etch more rapidly than the matrix, are known as grain boundaries. In general, the structure of a grain boundary is exceedingly complex but a special case should be distinguished when the orientation of neighboring grains is very similar. These are called low-angle boundaries.[16] Their geometry is quite simple and can be described in terms of dislocations.[3,17] A mosaic structure, very similar to low-angle grain boundaries in polycrystals, can be seen in etched single crystals. Higher etch rates at slight changes of orientations between one part of the single crystal and another account for the structure. This mosaic structure is also sometimes called crystal sub-grain-structure and originates from dislocation patterns in the crystal.[16]

3.16 Twin Boundaries

Twinning in crystals produces a fault in which one region of the crystal that is the mirror image of the other. This is caused by an angular shift in orientation of a major axis of the crystal lattice, or twin boundary.[16,17] A Twin often occurs in metals which have a low stacking-fault energy; this implies that the extra energy

required for any small atomic mismatch is small.[16] Twinning also occurs during mechanical deformation (cold work).[9,17]

As explained previously, deformation does not involve the general breaking of the atomic bonds by one atom being pulled from another, but rather the localized slip of one plane of atoms an atom at a time. Slip occurs on a particular crystallographic plane and in a well-defined direction; usually the direction of greatest atomic lineal density on the plane of closest atomic packing (e.g. the four equivalent {111} planes in FCC metals and six equivalent {110} planes in BCC metals).[9,17] Slip can be observed and measured in a standard tensile test. The operative stress producing the first signs of yielding is a shear stress, the stress parallel to the slip plane in the slip direction.[9,14,16] Derivation of the resolved shear stress component of the applied force along the slip direction and perpendicular to the slip plane was a key step in the understanding of deformation in crystals.[9] A threshold shear stress for slip on any active plane is found to be constant for any specific alloy and condition. This principle, known as Schmids' characterization is independent of orientation of applied tensile stress.

Establishing the conceptual link describing movement of crystal imperfections accommodating stress conveyed theories linking bonding to the macroscopic mechanical properties of polycrystalline aggregates. Testing for the engineering properties like Young's modulus, ultimate tensile strength, yield point, work hardening in various regimes were useful but insufficient for design. Visualizing the complexity of dislocation tangles and observing the changes between slipped and un-slipped regions of the crystal under load, and developing

schemes for dislocation interactions supported prediction of fracture and failure in use. However, A Bergers' Vector, useful to link bond energy and structure of the line defects like edge or screw dislocations has little design value.[9,14,16,17]

Dislocation theory can help explain how crystals react to stress and underpin the mechanisms of deformation. Dislocation theory thus has a supporting role and serves as a link between the microscopic structure and macroscopic behavior of metals. Knowing how Atoms, too small to be observed directly during test, respond to macroscopic environments and forces has yet to be directly derived from first principles. However, the approach can be valuable to help conceptualize deformation and fracture.

3.17 Deformation

Three separate stages of deformation in single crystals have been identified:

- **Stage 1—**easy glide
- **Stage 2—**linear hardening
- **Stage 3—**cross slip

Figure 11 shows the regions of the normal load—elongation (or stress—strain) characterization in each of these stages. The mechanisms of yielding and flow in super alloys can be associated with dislocation interactions. The means of accommodating deformation in a real alloy is more complicated as they are

polycrystalline aggregates. The following is a discussion of deformation in FCC single crystals. The structure of superalloys is typically FCC.

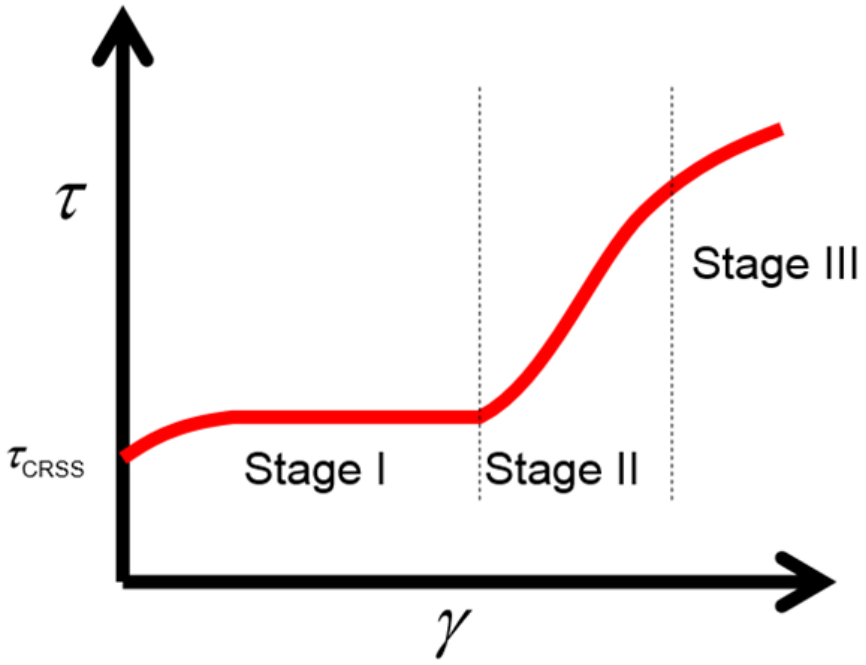

Figure 11. Three stages of dislocation movement found in fcc materials, only stages two and three are observed in polycrystals[16]

3.18 Stage I. Easy–Glide

In easy–glide (fcc, hcp) the dislocations can move fairly freely over large distances. Slip occurs on one set of parallel planes.[14,16,17] Dislocations in parallel slip plane have a tendency to line up under one another.[14] As deformation proceeds in stage one, there is some dislocation multiplication. Dislocations start to interact with one another impeding their motion. Thus as more dislocations are formed the stress for further deformation continually increases. In poly-crystals

stage one is not present and thus the observed mechanical behavior most often reported in studies is stage two and three. The dotted set of axis superimposed on the diagram in figure 11 highlights this fact.

Near the end of stage one some slip and dislocation multiplication would have occurred on other sets of easy glide planes which are not parallel to the primary glide plane.[9,16] Some of these dislocations, as they get close to or cross the primary glide plane will tend to hinder the motion of the original dislocation. This interaction becomes more pronounced as stage two is entered.

3.19 Stage II. Linear–Hardening

During stage two, substantial resistance to dislocation motion occurs. This resistance to dislocation motion is attributed to the following:

1. Like dislocations on the same plane repel on another. There will be a “back stress” if dislocations pile up against an obstacle—or as tangles occurring in the path of the glide plane at a grain boundary, or precipitate.[14,16,17]

2. Dislocations on one plane experience resistance when passing a piled-up group on a parallel plane—this is similar to the inter-planer interaction in stage one, but more marked.[16] Large, pile-ups of N dislocations act as a super-dislocation of Burgers’ Vector Nb. It will have concomitantly larger elastic strains and interaction forces.[16]

3. When dislocations must cut thought a ‘forest’ of dislocations which thread the glide plane.[16]

4. When dislocations cut thorough one another, one or both of the dislocations can be left with a ‘jog’. In the ‘jog’ one part of the dislocation has moved one Burger’ Vector relative to the other part. Depending upon the conditions and dislocations involved the motion in the ‘jog’ is either conservative or non-conservative. Non-conservative jogs will lead to the formation of vacancies or interstitials, as observed with dislocation climb.[16]

All of these mechanisms will operate as the dislocations multiply during subsequent deformation and so work-hardening proceeds and the stress required to cause flow increases.

3.20 Stage III. Cross–Slip

Dislocations blocked by an obstacle can cut through the obstacle, climb away from the obstacle, or cross slip away from the obstacle. Under sufficiently high stress and assisted at higher temperature, dislocations eventually gain enough energy to cross slip to a neighboring parallel plane.[16] Cross-slip initiates stage three of plastic deformation. This stage is characterized by a decrease in the rate of work hardening. In stage three, predominantly screw dislocations or those portions of any dislocation which has screw character, a gliding dislocation cross slips on an intersecting close packed plane to avoid the obstacle and subsequently continues in the same direction on a parallel close packed plane.[16,17]

Cross slip, illustrated in figure 12, must have several equivalent parallel slip systems to occur and thus is restricted to fcc and bcc lattice structures.[16]

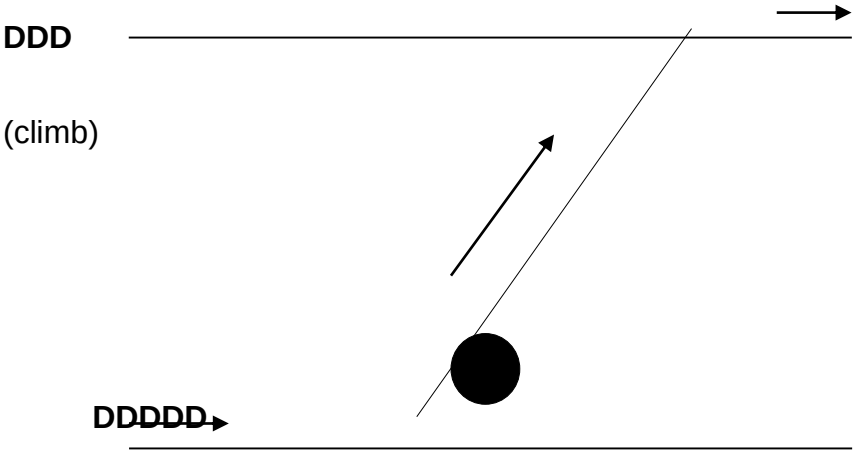

Figure 12. Cross slip, dislocations piled up against an obstacle give rise to hardening

Thermal activation is implicit to all dislocation movement and interaction. Increasing temperature facilitates movement between atoms on adjacent planes.[14, 16, 17] Along with heating comes an increase in atom motion and internal energy. There is a sound theoretical basis for the influence of temperature on the stress-strain relationship in materials. Following sections present a synopsis of testing practice and the concomitant relationships to dislocation theory, temperature, properties, and fracture in different regimes.

3.21 Mechanical Tests

A major purpose of mechanical testing is to provide data for modeling, useful in design. Mathematical description and modeling is the essence of engineering practice today. It provides the impetus and efficiency at the heart of modern systems. Modeling allows the design engineer to analytically test concepts and assumptions. One can never test for every condition of stress, strain, strain—rate, temperature, pressure for all of the continuum of the physical world encountered in the life cycle of a product. Good design will set reasonable limits. These limits are based upon experience, testing and desire to narrow the margin of ignorance. Material testing is developed to ascertain basic material properties in appropriately scaled macroscopic tests. The tensile test, normally conducted at room temperature, is the grandfather of all material tests. From a tensile test one defines key material properties with a measure of stiffness (Young's modulus), minimum flow stress (yield), ultimate tensile stress (UTS) and ductility (elongation and reduction in area). It is well known that when a metal is heated it becomes softer, and deforms more easily, and has a lower modulus. Thus the widely familiar room temperature material properties do not apply to design and application that requiring an alloy to operate at temperatures that are high fractions of the melting temperature or near melting (T_m or homologous temperature). Even hot—tensile properties are not sufficient when a mechanical design, like a turbine engine, operates at temperatures where the phases are in a state of dynamic change and thermal gradients play a major role in mechanical

behavior. For this regime of stress and temperature predicting the life and service of a part becomes complex and challenging.

Dieter presents a detailed treatise of the various models used to describe material properties covering the wide range of tests used to predict strength and flow in materials. Properties of superalloys are principally studied as a function of load, load- rate, strain, strain-rate, temperature, temperature gradients and atmosphere. Strain-rate has a marked influence where flow is well characterized by various test regimes adapted to study the independent variable, strain-- rate.

in/sec*	**Regime**
$10^{-8} – 10^{-5}$	Creep
$10^{-5} – 10^{-1}$	Static Tension
$10^{-1} – 10^{2}$	Dynamic Tension
$10^{2} – 10^{4}$	High-speed Impact
$10^{4} – 10^{8}$	Hypervelocity-impact

Two of the accepted mechanical tests and regimes used to describe flow at high-temperature are creep and stress-rupture. Data gathered has been analyzed and used to develop constitutive models like the Larson-Miller parameter, and the Zener-Holloman parameter. These models are used to characterize a number of different creep regimes. Similar mathematical models are outcomes of applying the scientific method in a systematic approach to construct theories correlating wide groups of observed facts capable of predicting general tendencies. Tests for

a property are inherently stochastic. Models developed for use by an engineer designing structures or machinery must often address variability and uncertainty in materials and processes likely to be experienced.

3.22 Creep

How alloys deform in a specific system of load and temperature has been studied extensively. As previously recognized, a primary aim of alloy development is to obtain strength at the highest temperatures possible without sacrificing ductility, toughness or corrosion resistance.

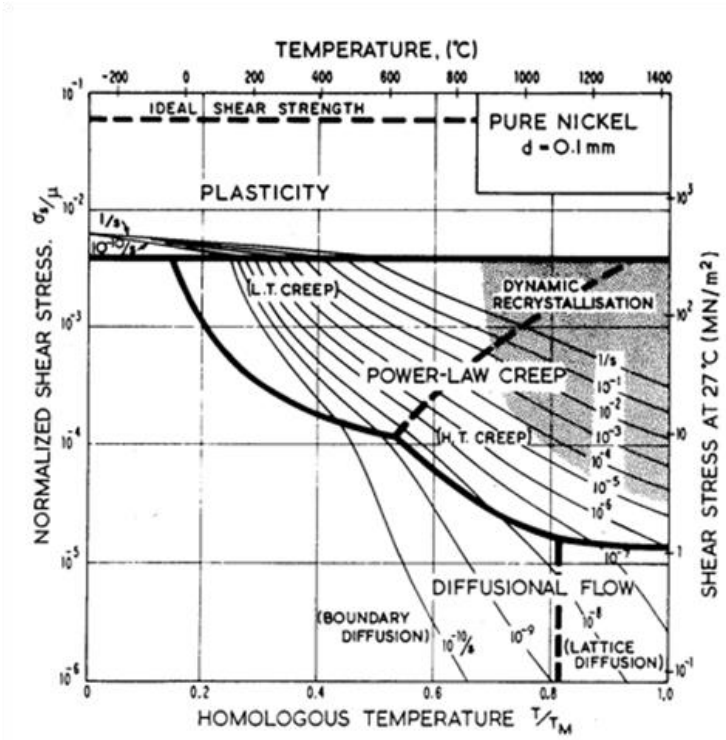

Figure 13. Ashby deformation map for creep—often leading to an increase in strength

At high temperature increased vacancy concentration, increased dislocation density and mobility decrease phase stability. This decrease is accompanied by a concomitant decrease in ductility.

Strain at temperatures above $0.5T_m$ pertains to the regime known as creep. Ashbys' useful amalgamation of the various flow regimes into a single schematic, called a deformation-mechanisms map made a marked contribution to organizing and understanding the test results reported from variations of temperature and stress on an alloy.[1,11] The deformation-mechanism map delineates the boundaries between the respective regimes identified with stress and temperature modes of flow. Boundaries are illustrated schematically with plots of test conditions normalized for test temperature to T_m and stress to shear modulus, G.[4] These maps summarized a great deal of empirical data and are useful as a quick reference for the alloy designer. This concept of property mapping has been applied to other empirical data such as fracture.

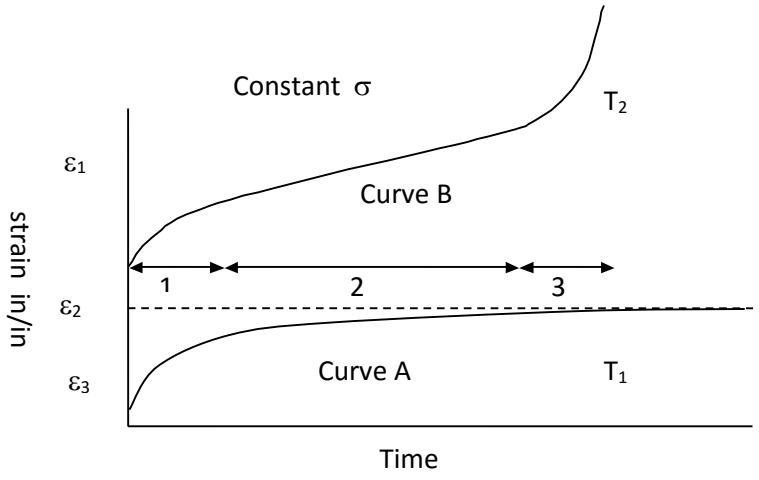

Figure 14. Basic Creep Curve[15]

Observed in the creep map are Coble creep and Herring creep, these are limiting cases. Coble creep deformation occurs by stress-assisted diffusion around blocking phases in the matrix. Significantly Nebarro-Harring creep deformation occurs by grain-boundary mechanisms resulting in sliding.[4, 9, 15] Alloy designs apply this knowledge to tailor composition and processing to promote precipitate phases and grain-boundary carbides to resist flow. Diagramed in figure 14 are two schematic creep curves illustrating deformation during constant stress and two temperatures ($T_1 < T_2$). In curve A, with constant stress, the creep strain rate initially is quite rapid followed by a decrease with increasing strain and time until it eventually reaches a steady state creep ε_2. Curve A typifies creep at low temperatures in the absence of thermal activation and display only stages 1 and 2. Conditions illustrated in curve A are successfully modeled as power law creep. Higher temperatures produce three distinct stages (1, 2, 3) with stages 1 and 2 following the power law pattern of curve A. Stage 1 is known as primary creep with Stage 2 known as secondary or steady state creep. During these periods the flow curve represents a balance between coincident work hardening and recovery within the microstructure. Finally, at stage 3, terminal or tertiary creep occurs. With the onset of Stage 3, concluding the power law range, accelerating strain

$$\dot{\varepsilon} = (B \sigma^n / G) e^{-Qsd / R T}$$

Figure 15. Development of dorn and weertman creep model

deformation is characterized due void formation just before nucleating growing cracks that ultimately determine failure mode.[1, 4, 9]

In the model formulated and advocated by Dorn and Weertman secondary creep, which occurs as a linear function of time, is strongly temperature and stress dependent. Strain rate conforms to an Arrhenius type function. This model is applied to low stress high temperature regimes where dislocation climb acts as the rate controlling mechanism. In this stage the Q_{sd} is the activation energy for self-diffusion.[9] Included in the Dorn—Weertman model is the well know power formulation of creep, given below:

$$\dot{\varepsilon} = B\sigma^n$$

Figure 16. Power law creep model

A power law model fits the creep response in the range of intermediate stress associated with stages 1 and 2. B and n are stress-independent coefficients determined for the alloy by testing and applied over the region investigated. Figure 17 is a plot of the stress exponent n for the pure metals Pt, Al, and Ni.

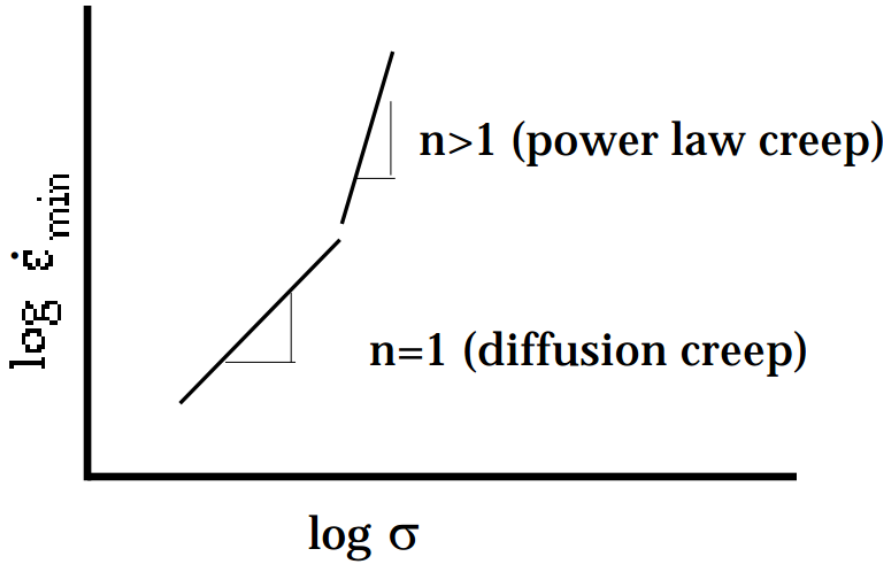

Figure 17. The stress exponent n in power law vs. stress – iso-temperature ^{o}K

Data of this nature is useful in studying basic flow mechanisms in crystals but suffers from an inability to compare different alloys over a range of stress, temperature and time. These are all variables crucial to engineering design. In a similar fashion, Ashbys' presentation has value in understanding flow response from the viewpoint of alloy design by depicting how alloys respond to different regimes of stress and temperature. However, the deformation map fails to include time, a crucial engineering variable. After predicting the conditions for the onset of flow, time to failure becomes dominant as a design parameter. To compare alloys in the time domain calls for testing every expected design condition. Testing is not an option when the planned life is 100,000 hours. Test durations of 11.5 years to validate design assumptions are just not practical. Larson-Miller

addressed this problem and formulated a model applying temperature and stress as variables.

3.23 Larson–Miller

At high temperatures, an alloy deforms slowly in response to a given stress. Time to rupture in the stress rupture test suggests a piece of the missing information. One cannot feasibly test at all levels of stress or temperatures to assure alloy performance in the time domain. When considering the important unknown variable missing in the conventional models, Larson and Miller published a most practical parametric model for relating the response of a material exposed to stress at elevated temperature for extended periods of time.

$$T\,(\log t = C_1) = b = f(\sigma) = P_1 \quad \text{or} \quad T\,(\log t = C_1) = P_1$$

Where

T = the test temperature (^{o}R or ^{o}K)

T = the time to rupture

C_1 = the Larson-Miller constant, often assumed to be 20 (15-20)

Figure 18. Larson—miller parameter for creep rupture

Dieter described the parametric approach by Larson-Miller as a tradeoff between temperature and time. Basically, it is a means of predicting long time

stress rupture values from tests of shorter time and higher temperature for the same level of stress.

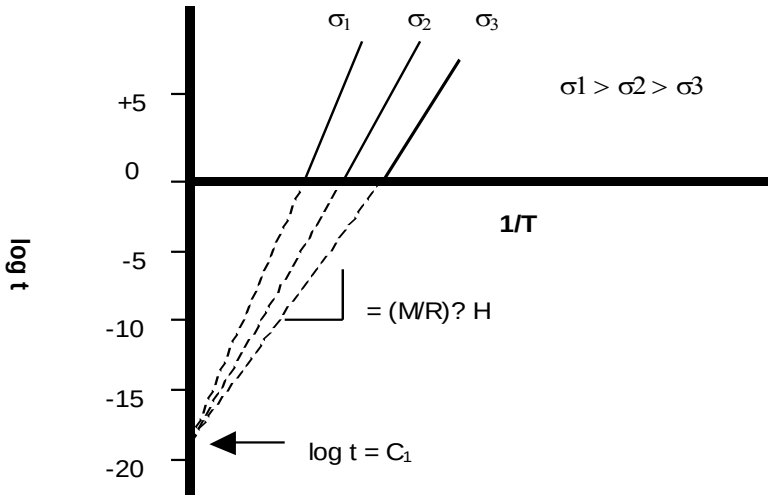

Figure 19. Development of the larson-miller parameter[24]

In figure 20, a relationship between short time stress-rupture data and the predicted operating conditions represented in the Larson-Miller analysis accurately accommodates time compression for evaluating a given alloy. This methodology also allows for the evaluation of alloys of different composition or treatment with analogous standards.

Operating conditions	Larson-Miller analogous test conditions
10, 000 hours at 1000 ^{o}F	13 hours at 1200 ^{o}F
1000 hours at 1200 ^{o}F	12 hours at 1350 ^{o}F
1000 hours at 1350 ^{o}F	17 hours at 1500 ^{o}F

Figure 20. Larson—miller testing time and temperature relative to actual conditions[24]

The schematic figure 21 shows a typical shape of a master curve of the Larson-Miller parameter for an alloy developed from paired time and temperature tests in a range of stress levels. When presented in this form, there is a clear representation of stress rupture data for different alloys on one plot. Care needs to be exercised when using the master curve approach for representing short term stress-rupture data not to over extend to extremely long times like 100,000 or more hours in service. These plots are seldom strictly linear. Further, if the diagram is used to predict stress rupture times at higher temperatures than the original test, it is vital to be sure metallurgical structure does not change in the extended operating regime. Such changes often alter mechanical properties, or change the dominant deformation mechanisms.

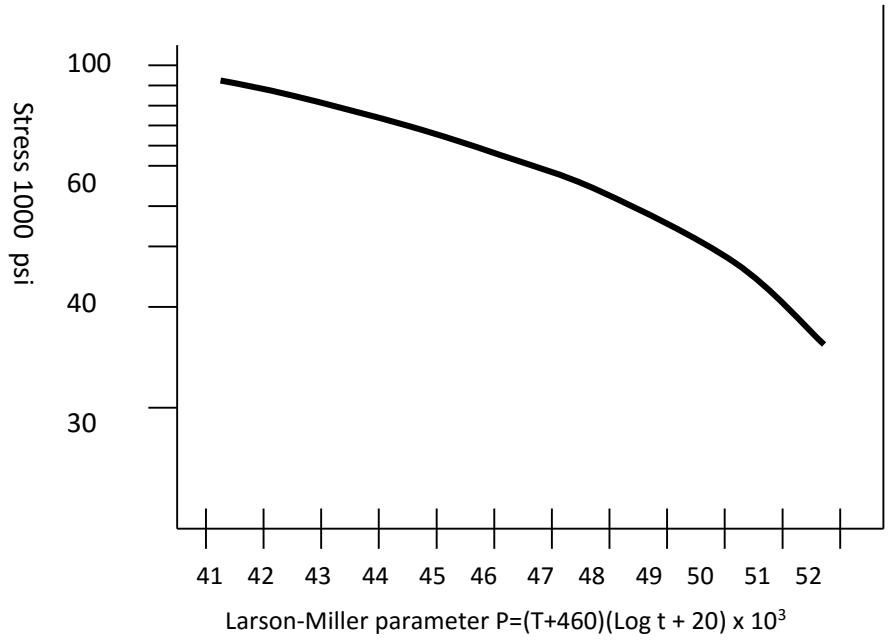

Figure 21. Typical larson-miller parameter alloy plot

Various mathematical models have been offered to represent test regimes known as creep, creep-rupture, or stress-rupture. This testing attempts to elucidate how an alloy will function in differing domains of stress, strain, and temperature. Some competing parametric models followed Larson-Miller and have practical application for limited regimes. Miller and Chamber, in *Superalloys,* summarize the models as follows.[1]

1. Larson-Miller $T(C + \text{Log } t)$
2. Manson-Hanford $(T - T_A) / (\log t - \log t_A)$
3. Pre-Sherby-Dorn $t \exp(- \Delta H / R T)$
4. Goldhoff-Sherby $(\log t - \log t_A) / (1 / T - 1 / T_A)$
5. Manson-Succop $\log t - B T$

Where

T = temperature

B, C, T_A, t_A = material constants

R = universal gas constant

Larson-Miller is used extensively for iron, cobalt, and nickel base alloys operating above 0.5T (Homologous) and up to 0.8 T_m. Considering the range of alloys, treatments and operating conditions where the model is used for turbine design, L-M treatment is established as the principle model. The L-M model has success in comparing alloy life as a function of stress, temperature and time, however it fails to predict the fracture mode.

Chapter 4

GLEEBLE TESTING

One good test is worth 1000 expert opinions – Learn by Doing

4.1 Procedure

The goal of this study was to investigate the hot ductility of the Inconel alloy 601 under conditions encountered in its' use as the furnace bed in a wafer fabrication furnace. Unexpected, rapid failures of the furnace bed were experienced in service. This is a recurring problem confronting engineers using super alloys. The complex thermomechanical history experienced by the furnace bed was seen as the root cause of these failures. The HAZ 1000 [DSI, Poestenkill, N.Y.], commonly and affectionately known as the Gleeble, was used to simulate the thermomechanical environment experienced by the materials in the furnace bed. Samples were tested in Argon atmosphere, and data developed characterized the changes in the material during exposure.

Many of the alloys available in the market are patented and proprietary, thus the detailed developmental data is unavailable or overly generalized. Companies providing materials don't often report problems or failures. Further, data that is available for specific alloys and conditions has a

tendency to be sales oriented or sanitized during publication to illustrate specific principles. Unexpected results frequently encountered in high temperature

applications, at first blush, occur in regimes similar to available data but the specifics of heating, cooling, heat and load cycling and/or atmosphere are sufficiently different to alter performance drastically from published properties. Also, even though the alloys are intensively researched the data generated to support a specific application is treated as proprietary. A proven furnace design experienced enigmatic failures not explained from experience or alloy data. Gleeble testing in this case was conducted to evaluate properties of tensile, yield, and ductility for Inconel 601 at several temperatures and strain rates of interest for four different sample treatments. In this section pertinent information regarding Gleeble simulations, test coupons and testing procedure is presented.

4.2 Gleeble General

The Gleeble is a unique computer controlled testing machine useful in simulating the thermomechanical conditions experienced by materials in actual applications. First developed at Rensiler Polytechnic Institute by Dr. Warren Savage to simulate the heating, cooling and mechanical loads experienced by materials during welding, the Gleeble has matured into a sophisticated thermomechanical testing system useful in studying material properties under many conditions. In union with controllable well characterized predetermined rates of heating and cooling, load and strain rate can be programmed to simulate real world environments.

4.3 Computer Interface

Computer control is achieved with a dedicated program interface language called GPL. This is a dos based system that will run on most current dos compatible computers. Programs and data originate and are stored on a pc, which is interfaced with a dedicated internal controller. The dedicated controller manages actual Gleeble control. Collected data from tests is passed to the interfaced computer for plotting and preliminary analysis. Data files are in ASCI II format and are exportable to any modern pc system using a spreadsheet, math or graphics program with ASCI II compatibility. Microsoft ® Excel, Math Cad, and Axum have all been applied to data analysis and plotting of Gleeble data. Axum has the most features and is the most flexible program of those used.

Typical GPL system control functions are listed below:

- 0--system on
- 1—mechanical on
- 2—heat on
- 3—pump on
- 4—high pressure on
- 5—high speed on
- 6—recorder on
- 7—X-Y operation off
- 8—quench 1 on
- 9—quench 2 on
- 10—x 10 force control on
- 11—auxiliary load cell on
- 12—acquisition on
- 13—air ram on
- 14—panic stop
- 16—datalyzer record
- 17—datalyzer run
- 18—auto zero channel #1
- 19—thermal auto stop mute on
- 20—heat mute on

The functions are toggled off or on based upon a digital clock during sequential execution. All logic requirements are handled within the GPL structure. This format gives full control over the testing with programming that is easy to establish, understand and modify.

4.4 Mechanical Control

The HAZ 1000 is a horizontal test frame with servo controlled air-over-hydraulic loading (10,000 lb. system maximum). Under stroke control the Gleeble can duplicate the moderate to rapid strain rates experienced by materials undergoing shock loads as in a crash or during forging. More moderate rates of loading are often accomplished with the system in feedback for load control. Loads are measured through a load cell mounted in line with the stroke piston shaft. The HAZ 1000 test chamber used in this study was equipped with a test isolation tank that allows hot ductility tests to be conducted either in a vacuum or protective atmosphere. An atmosphere of research grade (five 9's pure) argon was used in this testing.

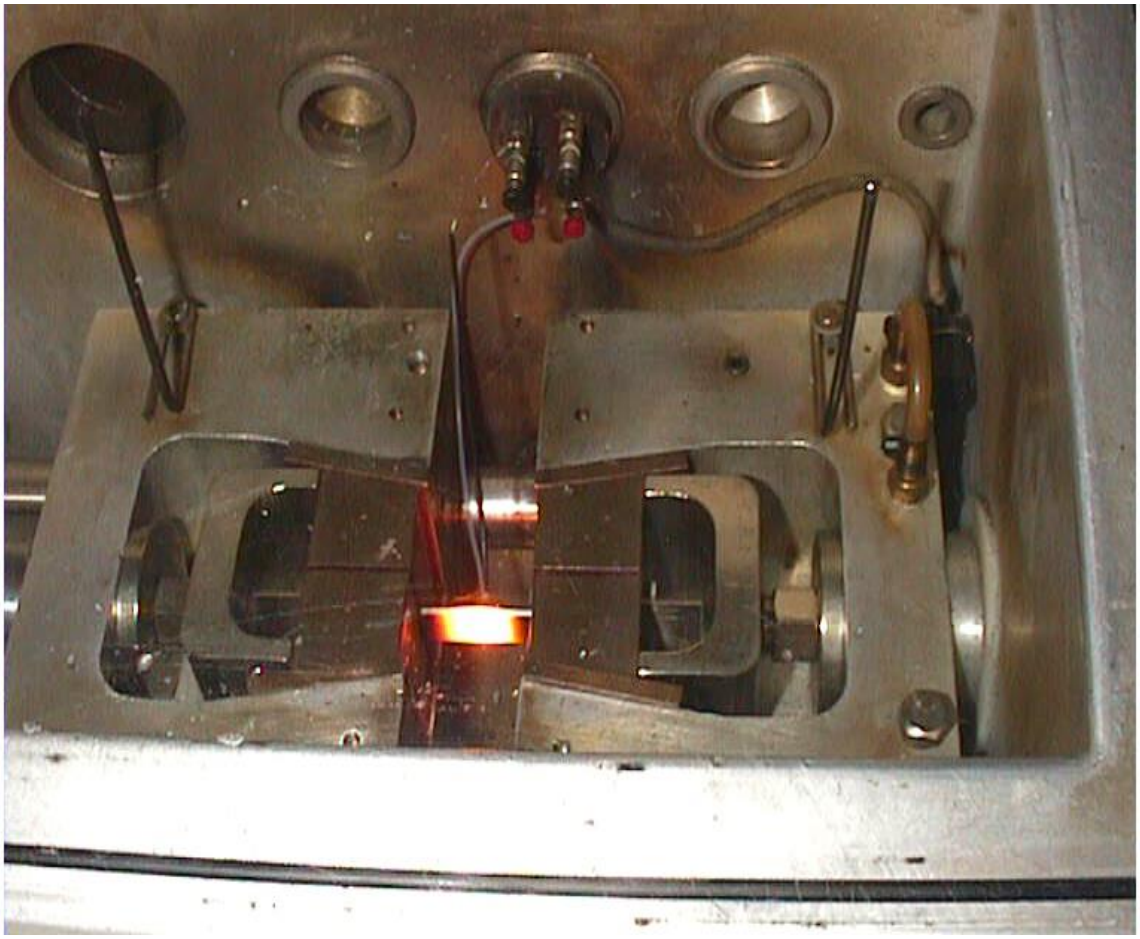

Figure 22. Gleeble isolation tank with sample under test

A glass safety cover seals the isolation tank and a mechanical vacuum pump is used to evacuate the atmospheric gases to a vacuum of about 30 inches of mercury. Rough vacuum is measured by a diaphragm gage. After evacuation the tank is refilled by purging with argon. This procedure is performed twice to assure low residual levels of oxygen and nitrogen in the test tank. A small flow of argon is maintained during the test to assure the argon atmosphere is maintained.

4.5 Heating

Heat is uniformly generated through the cross-section by resistance heating. Control is maintained by thermocouples attached directly to the test sample with a percussion welded ball bond. With the thermocouples welded to the sample a plane of control is established. Current required to maintain the predetermined temperature is regulated in a closed loop feedback through the computer interface and temperature control module. A means of adjusting temperature offsets between programmed and measured temperature in the cycle is provided through a vernier dial on the front panel In the HAZ 1000, 480V 3Φ, at 200 amps (~50 KVA) from the grid is transformed to 7—20 volts by setting variable taps on the system transformer. With the approximately 3000-7000 amps (reactive) available the sample can be heated a rates approaching 10,000 degrees per second. Limitations to the control and heating rate are a function of the resistivity of the sample under test and continued continuity of thermocouple contact.

Heating occurs in the central portion between the jaws and cooled at the ends where the jaws attach to the sample producing a thermal gradient. Jaw separation and the jaw type are used to control the severity of the gradient. Both water-cooled copper and hot jaws (Inconel or Refractory Alloy) are used to modify the thermal gradients. Point control of temperature is determined by the location of the thermocouple. Uniformity at the plane of maximum temperature is affected by the grip, jaw type, sample shape and material properties. Current is fed to the

sample through the jaws, therefore both the integrity of the grip and area of contact can influence the plane of maximum heat in a rapid test. In tests with heat-soak times or moderate heating rates there is a practical difference of only a few degrees between the test temperature and the plane of control with round samples. Other shapes require specific modeling and study that can be very complex and require special handling in the analysis of the data. With careful observation of the set-up and operation, placement of the thermocouples can be adjusted so that the plane of control and the plane of maximum temperature coincide.

Rapid heating and cooling experienced during welding is readily simulated with the Gleeble. In the continuum of heating—and—cooling of actual welds, crucial microstructures of interest may occur in a distance of a few grains. Controlled heating and thermal gradients like those found in forging or industrial tooling or piping are easily simulated with the Gleeble. This allows one to duplicate microstructures mechanical states in a sample several millimeters in width. Thus with simulation of a specific microstructure in the Gleeble sample, the material properties can be characterized for the temperature, and loading conditions of interest.

4.6 Chemistry

The Inconel 601 used in this study came from four sources. Two of the sources were commercially available wrought plate land commercially available rod. TEOS and Hydride samples were not tested to establish the chemistry; thus

it is assumed both mill product samples and muffle samples tested conformed to the nominal commercial chemistry for Inconel 601 as shown in table 6.

Table 6. Inconel 601 nominal chemistry

Ni	Fe	Cr	C	Si	Al	Cu	S	P	Trace
60.5	14.8	23.0	0.08 max	0.2 max	1.4	0.5	0.15 max	0.015 max	W,Ta,Cb ,B,Zr

Commercial Inconel 601 contains a portion of scrap remelt thus the presence of trace amounts of the elements W, Ta, Cb, B, and Zr may reasonably be considered as a possibility. These elements are not intentionally added, measured or controlled in the melt chemistry. However, in small amounts these elements can initiate important deleterious changes in mechanical properties observed to affect phase instability when the alloys are held at high fractions of the homologous temperature for long periods.

The third and fourth sources were samples made from furnace beds used in two different semiconductor processing applications. Process conditions of TEOS and Hydride were the only characteristics provided. All other information was proprietary.

4.7 Gleeble Test Samples

Gleeble test coupons are typically machined as shown in figure 23. These were provided by the project sponsor. Thermocouple wire for

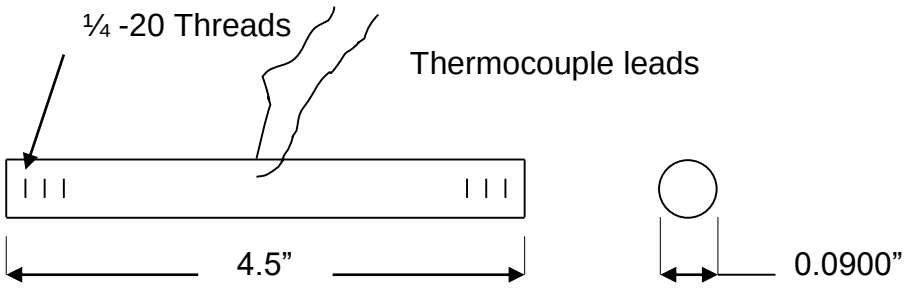

Figure 23. Typical gleeble tensile bar with thermocouples attached by percussion bonding

temperature control was percussion welded to the coupon at the center of the sample as indicated.

A grip spacing of one and a half inches was used in conjunction with copper jaws. This geometry provided a uniformly heated test zone of approximately one-inch-long and centered on the plane of control. The remainder of the distance between the jaws constitutes the thermal gradient at each end of the test zone with the length equally divided between each end of the sample. Fracture occurred in the sample center at the plane of control. Often splitting the thermocouples at the plain of control.

4.8 Fracture and Microstructure

Typical fractures were examined using the Amray 1810 scanning electron microscope (SEM). Pertinent images of the fracture surfaces were recorded. Longitudinal and transverse samples were cut from both the as received ends of the samples and in the fracture zone and mounted for metallographic examination. Typical sectioning and mounting are illustrated in figure 24 below.

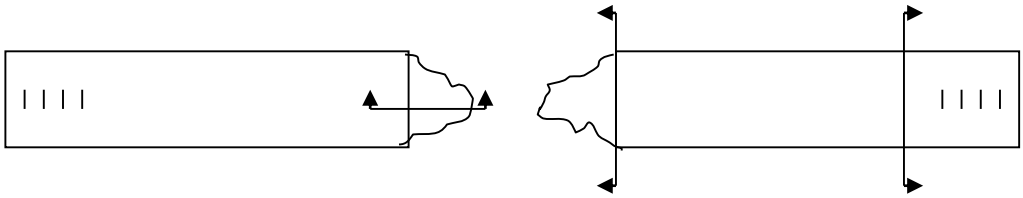

Figure 24. Typical sectioning “A” & “B” illustrating direction of mounting of metallographic samples

4.9 Imaging

Photomicrographs provide a crucial record of material changes before, during and after testing. Macrographs documenting visual conditions are important because memory and material conditions change with time. Ordinary light microscopy (OLM) in the range of metallography is effective in resolving and documenting microstructure. Typical magnifications vary from 50X up to 1000X. Practical boundaries of OLM are set by the resolution limits. Scanning electron microscopy supplement the knowledge of structure by extending the boundaries of observation beyond the resolution limits of OLM. A fundamental over view of electron imaging basics and data follows.

4.10 Electronic Characterization

Electron microscopes (SEM and TEM) are beam energy imaging systems. Resolution limit is determined by the accelerating voltage or velocity of the electron. Transmission electron microscopy is capable of resolution to the scale of atoms. One the other hand the SEM used in this study is limited to resolution to the 10's of nanometers. An SEM produces and image by scanning a sample with a focused beam of electrons. As the beam raster's the sample topography it interacts with the material producing signals containing information about the material. Backscatter and secondary electrons are applied to imaging. Secondary electrons are useful in both energy dispersive (EDS) and wavelength dispersive

(WDS) modes for analysis of chemistry and structure. EDS was useful in this study but had one significant limitation.

When beam electrons interact with the sample secondary electrons are produced well as electrons backscattered from the beam. Some of the backscatter electrons represent noise in the x-ray spectrum known as “Bremsstrahlung” radiation or, literally, breaking radiation. The radiation occurs in a continuum when a beam of charged particles decelerates when deflected by another charged particle (typically a nucleus). Bremsstrahlung radiation is proportional to accelerating voltage, probe current and atomic weight of samples and occurs in the region of electromagnetic spectrum coincident with the characteristic signals produced from elements with atomic weights lower than aluminum. Thus Bremsstrahlung (noise) radiation masked light element analysis. An EDS detector captures characteristic radiation produced when excited electrons fall in quantum steps (k, l, m) back to the ground state. Full width half maximum (FWHM) integration of counts detected in the characteristic peaks are used to produce a semiquantitative chemistry analysis of the sample. Precision of +/- 5% is possible with rough samples without a standard. Further, the SEM analysis is averaged as a result of surface and beam interacting to average concentration over a large interaction volume. The beam penetrates into the sample as a function of beam shape, angle of incidence, diameter, and accelerating voltage. Thus the volume region producing sample energy characteristics deviates from surface mapping. Correction factors for element, atomic weight, and sample florescence commonly called ZAF are applied to results to improve analytical results. But the exactness

and precision is still a reflection of a specific activated volume and near surface region of the sample, and thus does not exactly map the region in the field of view.

Chapter 5

RESULTS AND DISCUSSION

"The great tragedy of science is the slaying of a beautiful theory by an ugly fact"

Dr. A Huxley

5.1 Introduction

Evaluation and development of commercial alloys is, as a rule, a phenomenological exercise. The approach is to construct, test, observe and revise. Engineering properties are determined from modeling test results in the various regimes anticipated by design. Experience is the teacher.

Crystalline solids deform plastically by a number of alternative, often competing, mechanisms. Many regimes, like creep, hot-tensile, fatigue, and impact, represent and are macroscopic expressions of kinetic processes in plastic flow and phase stability. In the most general sense, properties of an alloy are determined by, strain, strain-rate, and temperature and the thermo-mechanical history. Alloy chemistry may set bounds to properties but does not in and of itself, determine properties. To be clear, behaviors observed at the macroscopic level are determined by kinetics of deformation on the atomic scale. Examples of these atomic scale processes include:

- ✓ glide-motion of dislocation lines on close packed planes
- ✓ coupled dislocation movement with interaction between glide and climb

- ✓ diffusion coupled flow of individual atoms; displacement of individual grains by boundary sliding (thru diffusion and defect-motion to and within boundaries)
- ✓ mechanical twinning (by movement of twinning dislocations)
- ✓ intragranular adjustment thru development of slip-traces or poligonization

These are the fine structure mechanisms of flow.

This thesis investigated the hot-ductility of Inconel 601. Tests were done at three different temperatures and four different strain rates. All tests were performed in an argon atmosphere. Both during testing and in-service, atmosphere is known to have an often profound influence upon both microstructure and properties. Samples were machined from different heats and processing of IN601 including as received plate, as received rod; and materials exposed to two different conditions in service. Test conditions examined were as received, strain aged and service exposed (Teos, Hydride). Gleeble testing enables a researcher to vary test peak temperature, heating and cooling rates, gradients associated with peak temperatures, mechanical loading and load rates (or strain and strain rates) in an environmentally conditioned chamber all controlled by means of a computer interfaced preprogrammed control system. This allows material testing to be done under the same dynamic, non-equilibrium conditions found in a complex real world processing environment. In this case, the ease and flexibility of thermo-mechanical testing with the Gleeble established bounds for critical conditions where a damaging change in the fracture mode of samples was observed. These

fractures reflected those actually observed in the material exposed in service as muffle plates in a wafer furnace. A regime of temperature, strain, strain-rate and temperature gradient was identified where the normally ductile nickel base alloy failed with very little ductility by brittle intergranular (BIG) fracture. In addition to identifying BIG fracture conditions, the Gleeble data was applied to define classic alloy properties; proportional limit, ultimate tensile strength and reduction in area for a range of temperatures and strain rates. An attempt to rationalize fracture behavior observed and to couple dynamic changes in alloy microstructure to observed results for flow and fracture in the material is presented.

5.2 Rod and Plate Test Results

Inconel 601 plate and rod were evaluated in the initial test series to determine base line properties. Plate was in the mill anneal or as received condition and the rod was strained in 3-point bending (3%) and aged at 1094 ^{o}F for 111 hours (strain aged). The strain-aged pretreatment simulates the effect of prior thermal mechanical treatment (PTMT) on hot-ductility in the regimes studied. In nickel base alloys PTMT influences mechanical properties at elevated temperature. These test conditions and regimes also provide representative material properties applied to explain BIG fracture conditions. Initial tests of the IN 601 confirmed the alloy was both strong and ductile in the regime of temperature and strain rate of interest. In the following discussion, values for load are given as a proxy for stress. Samples measured a nominal 0.250” in diameter.

As a prelude to the discussion, nominal chemistry for the alloy, previously presented (table 6, chapter 3) is repeated below for convenience.

Table 6. Inconel 601 nominal chemistry

Ni	Fe	Cr	C	Si	Al	Cu	S	P	Trace
60.5	14.8	23.0	0.08 max	0.2 max	1.4	0.5	0.15 max	0.015 max	W,Ta,Cb ,B,Zr

The main strengthening phases in the alloy are carbides and gamma-prime. Gamma prime does not form in this alloy under normal processing conditions. However, sufficient aluminum is present to precipitate gamma prime when nominal amounts of the trace elements Ta, Cb or Zr are present. Carbon forms various primary MC carbides during solidification like WC, or TaC. Primary carbides are unstable at elevated temperatures and transform to more complex carbides. Aluminum in the alloy may precipitate from the austenite matrix to the ordered intermetallic gamma prime at a temperature that is a function of the alloy chemistry and homogeneity. An empirical equation [83, 84] developed for estimating

the gamma prime solvus is:

T(Gamma prime solvus)°C = 1299.315 -2.415wt%Co -6.362wt%Cr

-2.224wt%Mo +3.987wt%W +0.958wt%Re +2.424wt%Ru +2.603wt%Al

-4.943wt%Ti+3.624wt%Ta

T = 1299.315 – 6.362(23 Cr) +2.603 (1.4 Al)

T = 1156.63 ^{o}C (2113.34 ^{o}F)

Figure 25. Regression formula for estimating gamma prime solvus[83, 84]

Results for the mechanical testing of as-received material and strain-aged material are shown in tables 8 and 9 respectively. Samples were tested at three different strain rates (0.5, 0.05, 0.005), all samples were tested at a temperature of 1024 ^{o}F. Values for load and ultimate strength, proportional limit, and reduction in area at fracture are summarized for each test condition. Results of the plate show that both the ultimate strength and proportional limit increased as strain-rate decreased. This behavior is central to that expected in a material, unless microstructural change is occurring during the testing.

Table 7. Test result inconel 601 plate, as received, test temperature 1024 ^{o}F (551 ^{o}C)

Sample Type	Strain Rate in/in	Ultimate Load lbs.	Proportional Limit Load lbs.	Reduction in Area %
Inconel 601 Plate	0.5	3853	3450	32.2
	0.05	4150	3747	31.2
	0.005	4233	3843	20.8

Reduction in area of plate shows a marked decrease when tested at the slowest stain rate. Strain-aged rod tested in the same manner as the plate reflected the contrasting prior-thermo-mechanical-treatment (PTMT) of the two commercial products. In rod the load at ultimate was nominally the same for the 0.5 and 0.005 strain rate. Strength of the strain-aged rod was nominally 5-10% higher than as received mill anneal plate. One possible reason for the lower load at ultimate for the intermediate (0.05) strain rate in rod is an improper aging treatment. In addition, values for load at the proportional limit were nominally the same at the onset of flow for the 0.5 and 0.005 and markedly lower for the intermediate strain rate (0.05). Dynamic interaction between temperature and strain rate first promote easy flow and then increased resistance to flow reflected in the test values.

Table 8. Test results inconel 601 rod, strain-aged, test temperature 1024 ^{o}F (551 ^{o}C)

Sample Type	Strain Rate in/in	Ultimate Load lbs.	Proportional Limit Load lbs.	Reduction in Area % %
Inconel 601 Rod	0.5	4546	3200	34.8
	0.05	4131	2471	27.2
	0.005	4526	3125	25.6

Percent reduction in area for the rod showed a marked monotonic decrease with decreasing strain rate; fractography to be presented later indicate ductile failure in all test regimes for the baseline tests.

Rod was used to save cost of machining of test samples from plate. Although the chemistry of the two forms conform to material specifications, processing and thermo-mechanical treatment (TMT) of rod and plate differ markedly. TMT differences would account for most of the difference in the material characterization reflected in a comparison of tables 8 and 9. In addition, the rod contains sulfur in higher levels than the plate. Presence of higher sulfur is noted in metallography, SEM fractography, and Energy Dispersive x-ray (EDS) analysis.

Base line results report a single test value for each material (mill) condition at three strain-rates at a fixed temperature (1024^{o}F) provides interesting findings for the effect of strain-rate. Due to the lack of replication, results must be considered with caution. Two mill conditions do not meet the standard for double replication although there is comparative value. Plate texture has important consequence to mechanical values in contrast with rod. As previously described, using rod saved cost and time. However, testing with two different mill conditions did detract from an ability to perform direct correlations of test results between mill condition and strain-aged condition with limited number of tests. Changes in toughness, as determined by reduction-in-area, are similar in both the rod and plate but are not entirely equivalent. Both sample types presented a decrease in toughness with a decrease in strain rate. Strain aging of the rod produced an observable difference for load at ultimate and proportional limit between plate and rod, with rod being 5-10% stronger. Strain-rate had no clear effect on the strength of the strain-aged rod. In the plate the load at ultimate and load at proportional limit clearly increased with a decrease in strain rate. Strain aging of the plate

during the test would account for this result. Lower values for the load at proportional limit in the rod compared to plate may be the result of Hall-Petch effect as the rod had a larger grain size. Microstructure will be addressed later, thus a discussion of the influence grain size on the yield will be deferred until then.

5.3 Plane Stress Test Results

Stress state can have a significant influence on fracture mode. The material in-service is gun drilled laterally thru the thick cross section and the resulting cylindrical void drilled in linear arrays of perpendicular closely spaced holes. This pattern is used as a gas path for the Teos and Hydride process gasses. Test samples of the plate with the center section hollowed by gun drilling were used to simulate the plane stress conditions in the service furnace plate. A state of plane stress is created by geometry and loading, often in concert with thermal gradient, generate localized strain in a highly constrained area of a part. Gun drilled holes(GDH) produced hollow samples were tested in the strain-aged condition. Residual effects of stress risers and severe

Table 9. Plane stress test results, inconel 601 plate, gun drilled center

Sample Type Plate, GDH / Strain Rate in/in	Test Temperature °F (°C)	Ultimate Load lbs.	Proportional Limit Load lbs.	Reduction in Area %
0.05	522 (272)	3984	2655	47.7
0.05	622 (328)	3882	2656	47.3
0.05	722 (383)	3848	2690	45.1
0.05	822 (439)	3760	2656	29.3
0.05	922 (495)	3564	2518	31.6
0.05	1022 (550)	3237	1578	41.9
0.05*	522 (272)	3604	N/D	N/D
0.05*	622 (328)	3882	2725	N/D

* These tests were identified as possibly anomalous during testing attributed to thermocouple placement and the effect of the gun drilled hole thus this data is for information only.

mechanical working occurring due to rough conditions of poor machining practice are considered when evaluating these results. Results of the gun drilled specimens tested at the intermediate strain rate of 0.05 and at increments of 100 °F for testing starting with 522 °F and going to 1022 °F are tabulated in table 10, above.

These tabulated results clearly show a gradual loss of strength starting at 722 °F and similarly a loss of ductility above 722 °F. The decrease in strength as

temperature increased is emphasized graphically (Figure 26), which plots strength as a function of temperature for the ultimate load. Load at yield fell 40% between 922 ^{o}F and 1022 ^{o}F.

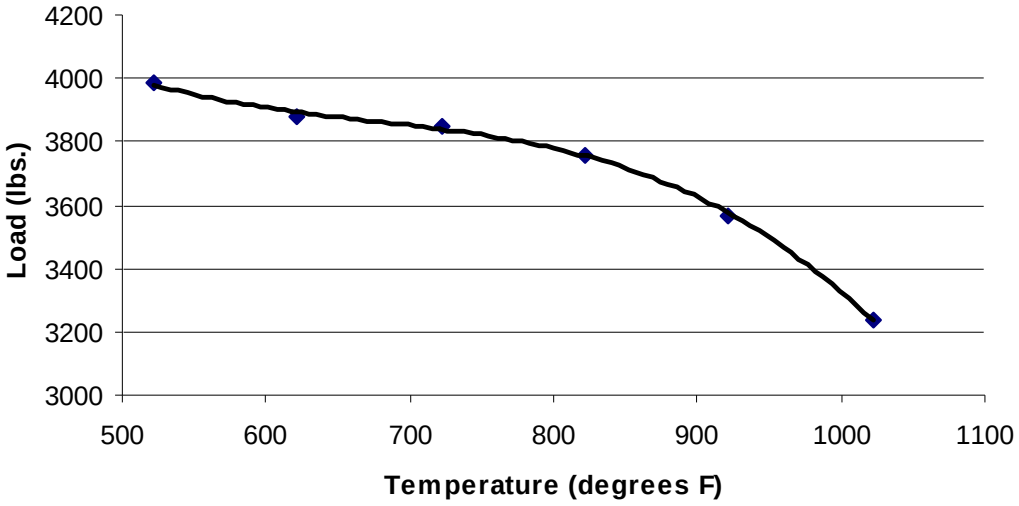

Figure 26. Plot, rod GDH plane stress – ultimate load vs. temperature

Conversely, reduction in area fell to 30% above 722 ^{o}F and recovered to nearly 45% at 1022 ^{o}F. No transition in fracture mode from ductile to brittle was found in the plane-stress test. Thus it does not appear plane-stress played a crucial role in the BIG fracture. However, a clear loss of ductility occurred between 800 and 1000 ^{o}F. These results parallel the changes in ductility observed in the plate and strain aged rod. These dips reflect a dynamic balance between strengthening mechanisms and softening mechanisms in the material.

The gun drilled material conforms to trends observed with the strain-aged rod. First reduction-in-area of both plate and rod show a loss of ductility with decreasing strain rate (figure 27). Second, in strain aged plain stress plate specimens a ductility dip was found between 700 and 1000 ^{o}F (figure 28).

At the 0.05 in/in strain rate a minimum occurs somewhere between eight and nine hundred degrees Fahrenheit. Evaluation of base-line tests was applied to determine testing regimes for service-conditioned samples.

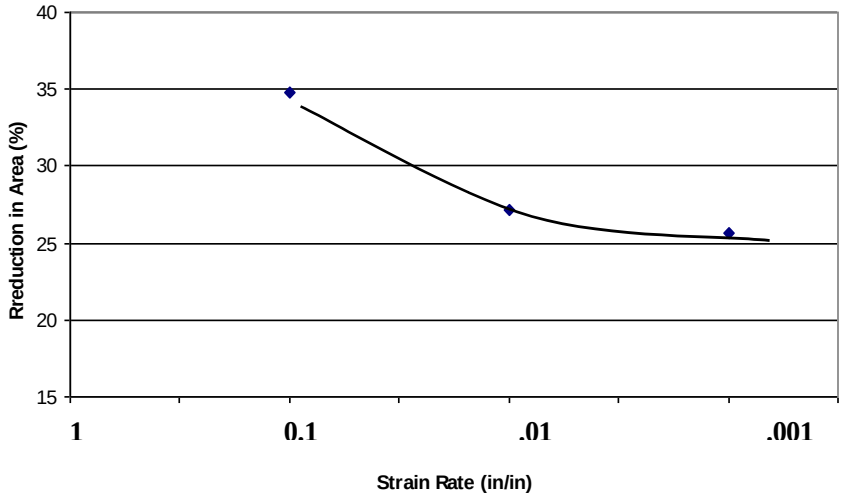

Figure 27. Plot, rod GDH, reduction in area vs. strain rate, temperature 1023 ^{o}F

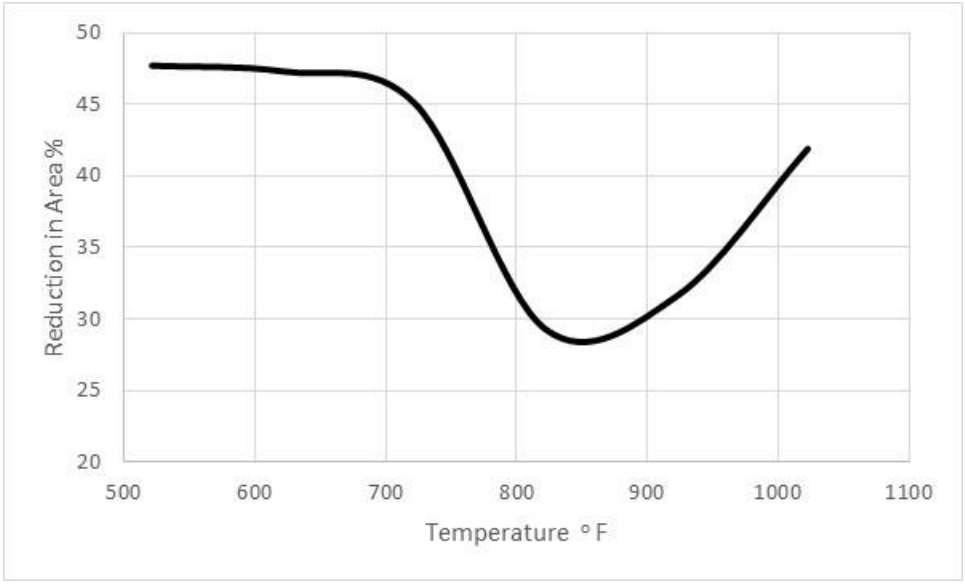

Figure 28. Plot, plane stress ductility dip, reduction in area % 0.5 in/in strain rate

5.4 Service Conditioned Specimen Test Results

Two varieties of service conditioned samples were tested; Teos and Hydride. Particulars of service conditions were not reported or controlled for the purpose of this study as these conditions are considered proprietary by the user. Thus these conditions are not reported and not varied in this study. Sample identification provided had the two treatments only. However, each process can be assumed to have chemical atmosphere and thermal regimes typical of those used in the manufacture of microprocessors. Full simulation of process conditions was not pursued. Each test was used to refine selection of temperature and strain rate applied in subsequent testing because the number of samples provided for testing was severely limited. Programmable features of the Gleeble 1000 system underpinned the ability to successfully change to the test plan on-the-fly. Impromptu change allowed the corporate participant to fully explore the critical change in fracture mode from ductile to BIG fracture. It was unknown how service exposure altered the base line alloy properties.

Table 10. Test results inconel 601 plate, teos conditioning

Sample Type Plate, Teos Strain Rate in/in	Test Temperature °F (°C)	Ultimate Load lbs.	Proportional Limit Load lbs.	Reduction in Area %
0.05	1292 (700)	4775	3074	19.6
0.0005	1292 (700)	3647	2606	11.4
0.00005	1292 (700)	3095	2255	12.9
0.5	572 (300)	5375	3180	29.0
0.5	1022 (550)	4853	2772	31.6
0.0005	572 (300)	5415	2516	N/R

Teos samples ultimate load, and proportional limit, decrease monotonically with decreasing strain-rate. At a fixed temperature, a small decrease in reduction-in-area was found when strain-rate was slowed from 0.5 to 0.0005 in/in and then recovered slightly when strain-rate was slowed further

Table 11. Test results inconel 601 plate, hydride conditioning

Sample Type Plate, Hydride Strain Rate in/in	Test Temperature °F (°C)	Ultimate Load lbs.	Proportional Limit Load lbs.	Reduction in Area %
0.05	1292 (700)	5005	2875	8.8
0.0005	1292 (700)	3979	2964	2.5
0.00005	1292 (700)	3488	2796	4.9
0.5	572 (300)	5625	2865	N/R
0.5	1022 (550)	5283	2814	14.7
0.0005	572 (300)	Not	Tested	---

to 0.00005 in/in. Slight improvements in ductility are not significant given the number of samples available for testing. Replication is required to improve significance. The limited number of samples did not allow deeper evaluation.

In the tests of Hydride samples, ultimate load and reduction-in-area were found to decrease with decreased strain-rate. A loss and recovery of reduction-in-area with the changes to strain-rate similar to the Teos condition was also found for the Hydride test. However, the ductility values were markedly lower with Hydride. In both Teos and Hydride samples the fracture mode changed from ductile at rapid strain-rates (0.5) to BIG fracture when tested at the slowed (0.00005) strain-rate. This transition in fracture mode will be explored more completely in the fractography discussion.

5.5 OLM Microstructure and Grain Size

Samples of as-received plate and rod were sectioned, mounted, and etched to reveal grain boundaries and to compare with published examples of Inconel microstructure. Samples of the rod were considerably more difficult to etch than plate because the rod contained many more inclusions. Figures 30 and 33 show microstructure typical of the rod and plate in the polished and etched conditions, respectively. Etching was done with Kalings #1 ($CuSO_4$—HCl 50 : H_2O 50%) for 20 seconds to one minute.

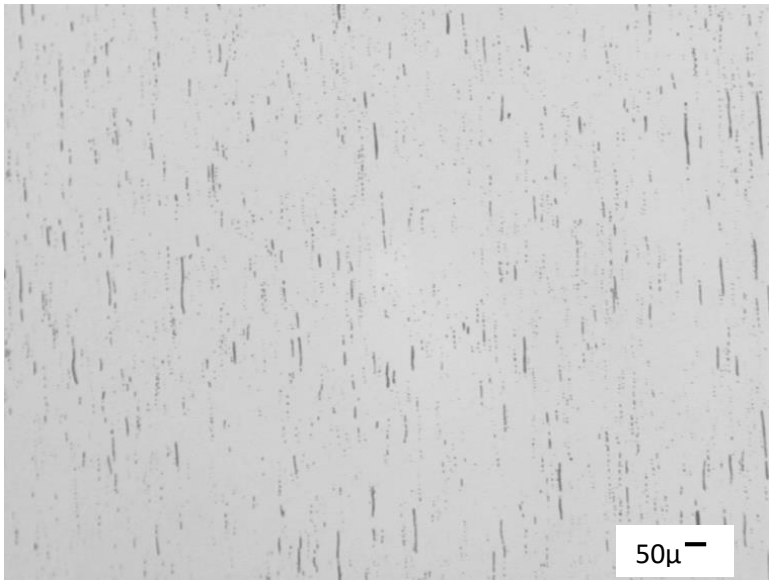

Figure 29. Microstructure, rod as polished, 200 X

Notice the presence of elongated inclusions in both photomicrographs. X-ray energy analysis (EDS) during SEM examination identified the inclusions as sulfides.

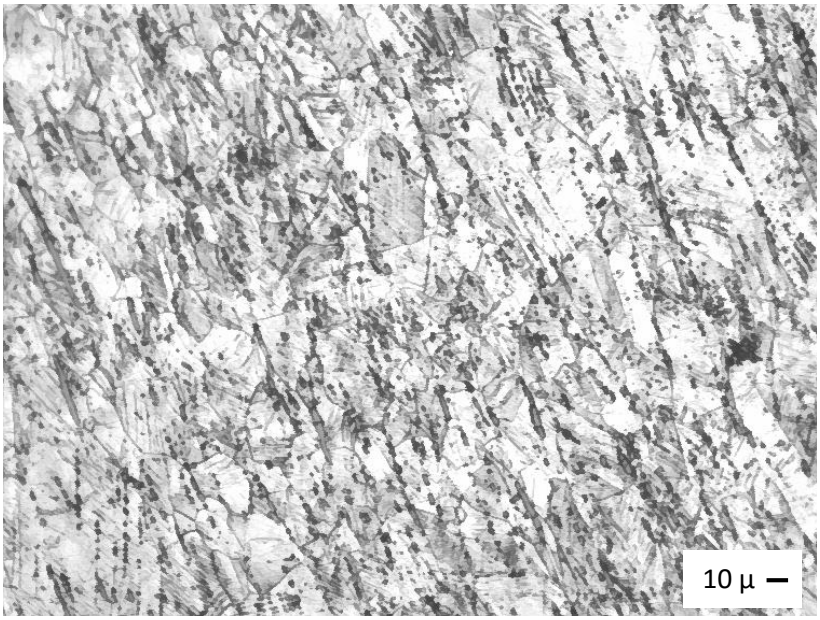

Figure 30. Microstructure, rod etched, kallings, 500 X

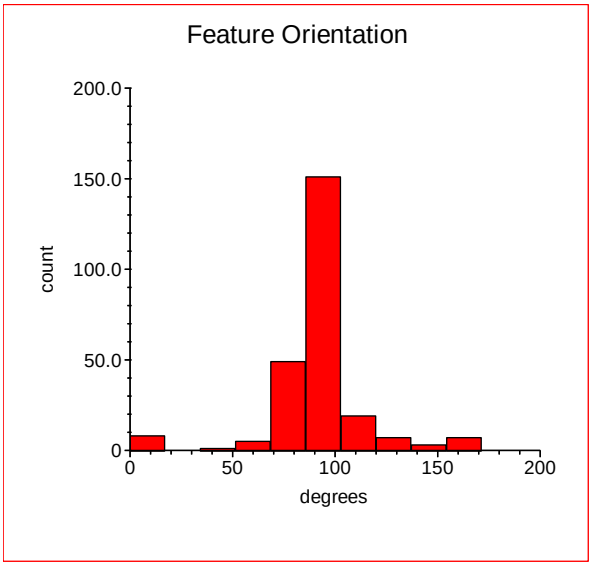

Field Summary	
Bitplane	Bitplane1
Max:	171.563 °
Min:	0 °
Mean:	93.2512 °
Std Dev:	22.7422 °
Fld Area:	216608 µm²
Tot Area:	216608 µm²
Fld Count:	1
Obj Count:	250
Over:	0
Under:	0
Accepted:	100 %

Figure 31. Feature measurement/orientation, buehler image analyzer

Microstructures were analyzed using a quantitative microscopy system. Figure 32 clearly shows a preferred orientation in the inclusions as a result of forging procedure.

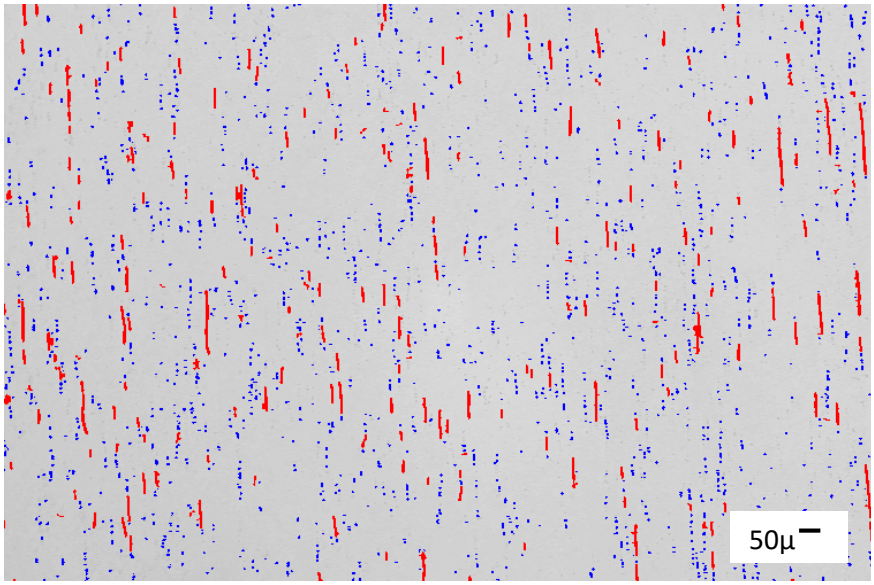

Figure 32. Bit-plane separation of elongated sulfur inclusions (blue & red)

Etching of the plate and rod materials with fresh Aqua Regia produced excellent grain boundary contrast which enabled the grain size of each material to be determined. Furthermore, regions of twinning formed during heat-treatment are evident.

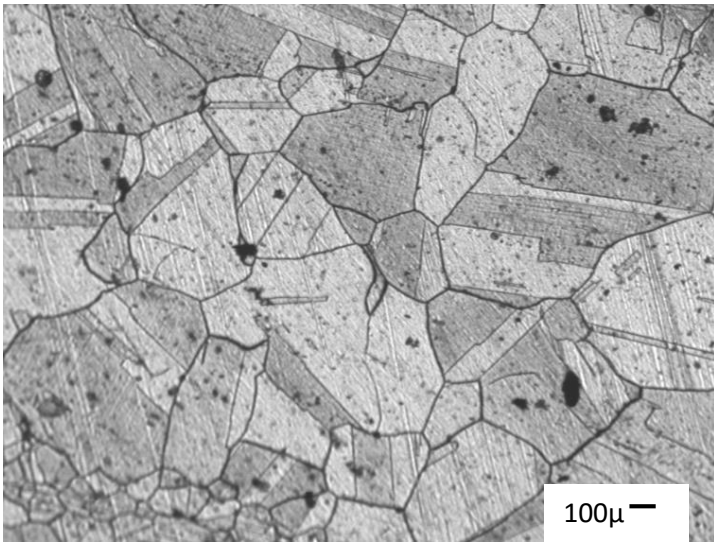

Figure 33. Plate etched for image analysis of grain size, 100 X

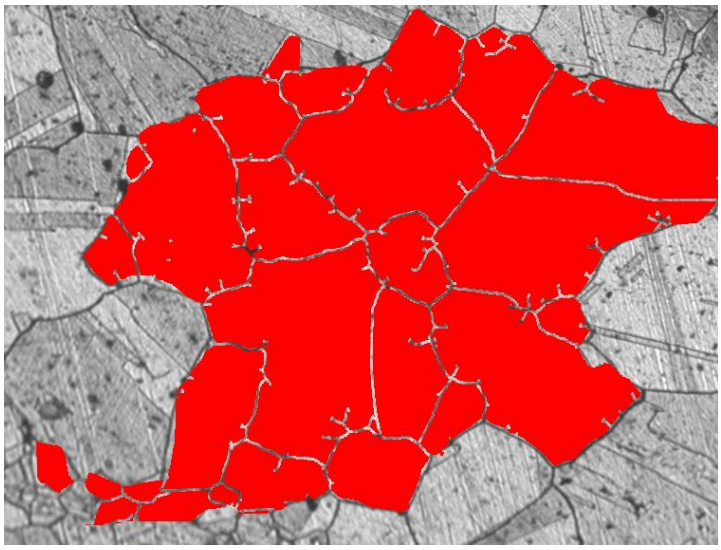

Figure 34. Typical field of bit plane separation used for grain size

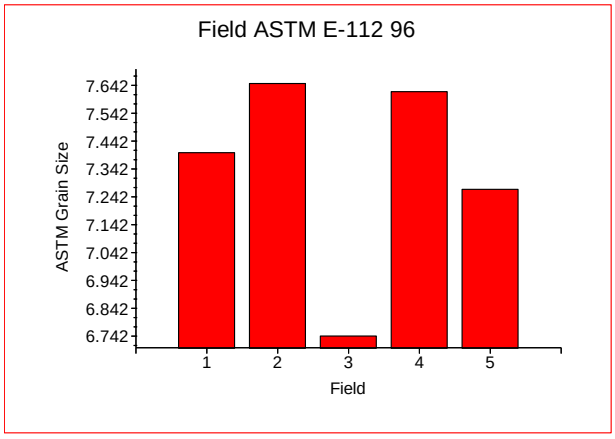

Field Summary

Bitplane	Bitplane1
Max:	7.64807
Min:	6.74167
Mean:	7.33533
Std Dev:	0.367155
Fld Area:	71207.6 µm²
Tot Area:	356038 µm²
Fld Count:	5
Over:	0
Under:	0

Figure 35. Results of grain size measurement of plate (5 fields)

Plate grains were uniform with a mean grain size of 7.3 ASTM and two sigma standard deviation of less than one. By comparison, grain size in figure 30, typical of the rod, is estimated at 10-12 ASTM.

5.6 Flow and Fracture Discussion

Flow mechanisms and fracture surfaces in pure metals and in alloys have been extensively studied and well characterized. The basic tensile test, normally conducted at room temperature (RT), is widely used as measure of mechanical strength. A tensile test is simple to perform and is widely accepted to characterize engineering materials. The uniaxial tension test at room temperature provides the important material values; Modulus (E), Proportional Limit (PPL) and Ultimate (UTS). The values represent three important macroscopic changes in crystal deformation.

- In the Elastic range metal crystals stretch without permanent macro change. This region is characterized by the important material property known as the Modulus. In this region, Stress = E (strain) and strain is recoverable.
- Non-recoverable change, plastic deformation, occurs after load (stress) exceeds the PPL. Between the PPL and UTC the deformation is uniform.
- At the UTS there is localization of plastic strain. The on-set of plastic instability causes the sample cross section to deform locally. Elongation is no longer a useful characterization of strain. Reduction in area measures the extent of local deformation to final fracture.

However, in many applications where materials must be used the mechanical properties measured and published from tensile tests at RT are of little value for

reliable characterization of flow and fracture. At temperatures above 0.4 T_m, various approaches to characterize properties have been employed to include:

- Hot-tensile testing
- Creep testing
- Stress Rupture testing
- Low Cycle Fatigue and High Cycle Fatigue and various cycles

Each approach involves a standardized testing methodology and modeling calculus. Some of the theoretical engineering models based upon creep and stress rupture have been previously presented (chapter 3). Creep and Stress rupture are time consuming and tedious to complete. Investigation and evaluation of the fractures created in the Gleeble test was accomplished in short times. The fractures were evaluated with an Amray 1800 SEM equipped with EDX. Furthermore, engineered thermal gradients in the Gleeble provide opportunities to evaluate the effect of such gradients on microstructure and concomitant flow regimes within each test. Such gradients are often encountered but rarely appreciated in actual production or service. However, a unique ability to control temperature in closed loop with the attached thermocouple provides both data and precision not found in other systems or test methods.

As indicated above, engineering and material models rely upon testing, measurement, and observation to describe and predict material behavior. Interpretation of hot-ductility and fracture improve as investigative tools become more powerful. Early studies of structure and flow (1947-1952) were based in

imagination and conjecture. Theory improved and became accepted as factual when the ability to image structure and measure chemical composition precisely in small areas improved. Also precision improved with automated data collection. Development of modern instruments commonly used in fracture studies advanced functional evaluation of feature size related to crystal defects. Advancements are illustrated in figure 36.

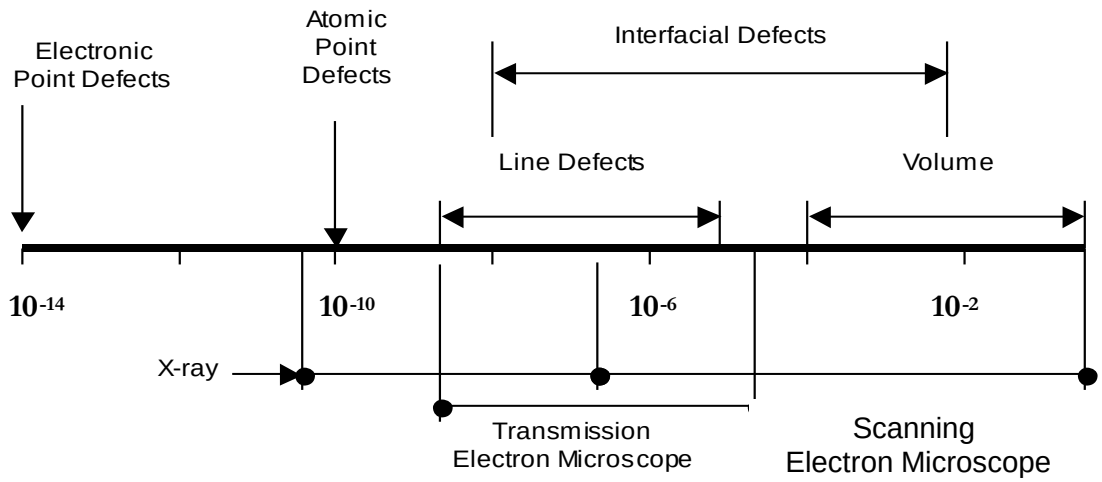

Figure 36. Dimensional ranges of different classes of defects and imaging methods[29]

Resolution in TEM and SEM imaging systems are several orders of magnitude better than resolution available with traditional light microscopes. TEM and SEM have been applied to study microstructure and fracture with great success. An explanation of beam imaging was presented in chapter three. Electronic noise of Bramsturlung (breaking) radiation obfuscates characteristic x-ray peaks of elements below Aluminum in the periodic table. Accessories added to the electron beam instruments improve spatial resolution and chemical sensitivity. Auger and Secondary Ion Mass Spectroscopy (SIMS) are two

adaptations of basic beamed instruments used to examine surface structure and chemistry. Researchers, like C.A. Hippsley, studied fracture produced in vacuum (10^{-7} torr.) and at a partial pressure of oxygen (10^{-3} torr.) and concluded sulfur at crack tips embrittled grain boundaries. Phosphorous has been similarly implicated in BIG fracture by others. How composition and microstructure affect fracture mode will be discussed in the section treating interpretation of fracture surfaces. Flow and fracture can be studied over a wide range of physical scales and time periods. Our understanding and theory of metals relates concomitantly with an ability to measure, analyze and model between the scales of macroscopic, mesoscopic, microscopic, and atomic.

McLean, et al., provided a summary of early studies of fracture, in the nickel based alloys Nimonic 80, 80A, 90 and Rex 337A. This summary included important observations concerning intergranular fracture and cavity formation in tensile tests performed at temperatures above 0.4 T_m. McLean's test regimes were at constant load or constant stress, e.g. creep, and under severe conditions hot tensile samples failed by intergranular fracture. He found that the characteristics of the fracture observed depended on stress. At high stresses, cavities were predominantly wedge-shaped and based on grain corners (w-type). At low stresses, they were distributed along the boundaries (mainly transverse) and rounded (r-type). At intermediate stresses, both types of cavity were found. Mechanisms of crack nucleation and growth are discussed in more detail with presentation of work by White (see figure 39).

In Rex 337A, cavities were found within the grains at the higher stresses, and fractures were transgranular; there was evidence that cavities were formed at the points where crystal slip was blocked by precipitate particles. At low stress, Rex 337A showed r-type cavities.

In the Nimonic alloys, Weaver found that the form of the grain-boundary precipitate depended on heat-treatment, which influenced ductility and the type of cavities. When large particles of carbide were present at the boundary, cavities formed in the true grain boundary between the particles, often adjacent to the particles; cavities never seemed to form in the precipitate matrix boundary. When the cavities were linked to form cracks; such cracks were zigzag in shape, sometimes going above, sometimes below the particles. When the precipitate was fine and duplex, cavities were correspondingly smaller and, as before, located in the grain boundary between adjacent particles. When the heat-treatment resulted in ductile grains and no boundary precipitates, cracks formed from w-type cavities at the triple points.

Cracks were observed to form at each end of an annealing twin that completely crossed a grain. However, they would form on opposite sides of the twin boundary, with the result that the cracks and twin boundary would constitute a Z-shaped configuration. It was observed that these cracks apparently commenced at triple points and extended towards the twin boundary. Where cracks in the boundary extended as far as twins that did not completely cross the grains, there was evidence of accommodation by slip beyond the ends of the coherent twin boundaries, suggesting some relaxation along the twin boundaries.

Precipitation was also greater along such twin boundaries that in the matrix. Glen found that when the alloys were tested in normal hot-tensile tests, a peak in strength was associated with the minimum ductility in plots against temperature. This peak was associated with strain-age hardening.

These observations were made on polished samples using OLM. Subsequent studies of fracture at high temperature using the TEM or SEM have added depth to the observations and established fertile ground for the development of dislocation theories relating slip and cross slip.

The Gleeble has been used to study strain-aging previously. Short time elevated temperature tensile tests of Inconel X-750 were conducted Savage and Dix to establish Pot Weld Heat-treatment (PWHT) behavior. Testing temperatures in the range of 1000-1750 ^{o}F and at strain rates ranging from 0.16-16.0 ipm were conducted with emphasis on measuring ductility, flow strength, and ultimate tensile strength. During (PWHT) cracking can occur when a stress of sufficient magnitude acts on a susceptible microstructure at an appropriate elevated temperature. Theories associated with this mode of failure dubbed this type of failure strain-age cracking. Cracks associated with the loss of ductility in the temperature range of 1600-1700 ^{o}F were found to cause failure in Inconel X750 weldments. Samples tested in air have lower ductility than samples tested in nitrogen, argon or vacuum. Prager and co-workers investigated Rene 41 and concluded that hyperfine γ' in the γ matrix was the deleterious microstructure responsible for cracking.

Dix and Savage used the following test procedure: samples were placed in the test chamber in an argon atmosphere and heated to the selected test

temperature at a rate of tens of degrees F per minute. After reaching the desired temperature, a uniaxial tensile load was applied at a crosshead velocity approximating the strain rates selected. Elongation is confined to the hottest central zone of the specimen where the thermocouples are attached. This zone approximates a constant strain rate that is nearly uniform during the test.

Dix and Savage observed serrated yielding or load drops in testing Inconel X-750. The number of drops and severity decreased sharply with increasing temperature and decreasing strain rate. Further, in specimens tested above 1660 ^{o}F serrated yielding was not observed. Harding and Honeycomb reported similar results in austenitic steels containing Nb and Ti. However, in the austenitic steels the discontinuous (serrated) yielding was attributed to immobilization of dislocations by the precipitation of carbides along the dislocations paths. Owczarski reported similar behavior in Waspaloy and Inconel 718 but found the serrated yielding restricted to a limited temperature range.

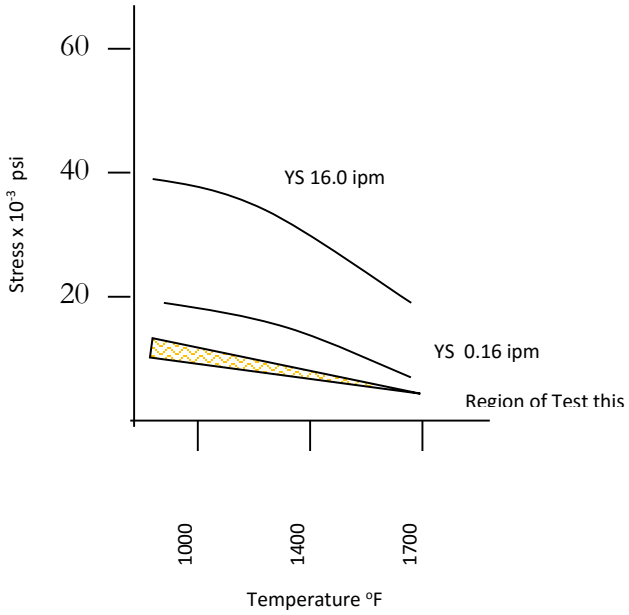

Figure 37. Schematic drawing of the effect of temperature and strain rate on yield strength in inconel X-750[66]

In testing Inconel X-750 Dix and Savage found a 50% reduction in yield (flow stress) between tests at 16.0 ipm and 0.16 ipm. Reduction in strain rate had a more significant effect on flow stress than an increase in temperature in the range from 1000-1660 ºF.

Research at the Savannah River Laboratory used hydrogen-assisted fracture to study the failure modes in a series of FE-Ni-CR alloys and found: [33]

- Faceted fracture
- Quasi-cleavage
- Striations

- Dimpled fracture (void coalescence)
- Twin-boundary parting
- Intergranular separation

The study concluded the alloy system (composition), prior thermo-mechanical history (TMH), strain rate, temperature and stress in combination determine the fracture mode and ductility as measured by reduction in area (RA). Sulfur and Phosphorous segregation to the grain boundaries and an increase in the per-cent nickel in an alloy were noted to influence a change to IGF mode. General characterization of alloy and fracture in the above is representative of conclusions from research published during the period covering 1965 thru 1985. Table 13 provides a list of key publications, with dates and with topics. This table is a chronology of research highlights from significate work focused on properties of alloys and damage leading to fracture.

Table 12. Chronological list of key publications, authors, and topics

Publication Date	Lead Author and Topic	
1978	R. Raj	Intergranular Fracture in Bi-crystals
1979	M.P. Seah	Adsorption-Induced Interface Decohesion
1982	R. Raj	Intergranular Creep Fracture In Aggressive Environments
1983	C.L. White	High Temperature Embrittlement of Ni and Ni-Cr Alloys by Trace Elements
1987	J.J Lewandowski	Effects of Impurity Segregation and Test Environment of Sustained Load cracking of 2 ¼ Cr- 1 Mo Steel –II Crack Propagation

1987	D.H. Lassila	Intergranular Fracture of Nickel: The Effect of Hydrogen—Sulfur Co-Segregation
1987	C.A. Hippsley	Sulphur Segregation and High-Temperature Brittle Intergranular Fracture in Alloy Steels
1992	J. Kamada	Mechanism of High Temperature Brittle Intergranular Cracking in High Strength Nickel Alloys
1998	P.G.Shewmon	Grain Boundary Cracking
2003	N.E. Nissley	Development of the Strain-to-Fracture Test
2003	M.G.Collins	Investigation of Ductility Dip Cracking in Nickel-Based Filler Materials—Part I
2003	M.G.Collins	An Investigation of Ductility Dip Cracking in Nickel-Based Weld Metals—Part II
2003	M.G.Collins	An Investigation of Ductility—Dip Cracking in Nickel-Based Weld Metals—Part III
2003	Hu-Chul Lee	Electron Microscopy Study on the Grain-Boundary Precipitation during Aging of Fe-10Ni-5Mn Steel

Raj studied fracture in bi-crystals of copper dispersion hardened with fine silica particles. This study provided a quantitative basis for the theory of diffusion-controlled growth of cavities in grain boundaries at constant load and elevated temperature. This study is an early indication of the importance of hydrostatic stress at the crack tip in promoting dislocation enhanced material flow at grain boundaries. Dimpled surfaces were produced where silica inclusions initiated a

loss of cohesion. Seah studied ferrous matrix and segregation of some 70 minor element solutes with Auger electron spectroscopy (AES). Sensitivity and spatial separation possible with AES documented precise grain boundary locations and concentrations influencing fracture in SAE 4130 steel when temperatures were less than 100 ^{o}C. The elements Bi, S, Sb, Se, and Te, segregated at GB were all found to be “highly embrittling”, and are listed in order of decreasing potency. Other elements having an intermediate effect were; P, As, Ge, Si, and Cu. Notably, the presence of N, B, and C were shown to promote recovery of grain boundary strength. Oxygen was not studied in this research.

Raj followed previous work with a study of the effect of O_2 on a nickel alloy. He asserted that oxygen migrating to the GB participated in void formation. He also asserted that fracture was enhanced by pressure exerted through internal oxidation. Subsequent work using chemical thermodynamics demonstrated that development of CO pressure in internal voids cannot rise to a high enough level to cause fracture. However, the implication of elements diffusing to a triple point or to incoherent precipitate surfaces was insightful, and prescient to later investigations with better theoretical foundation.

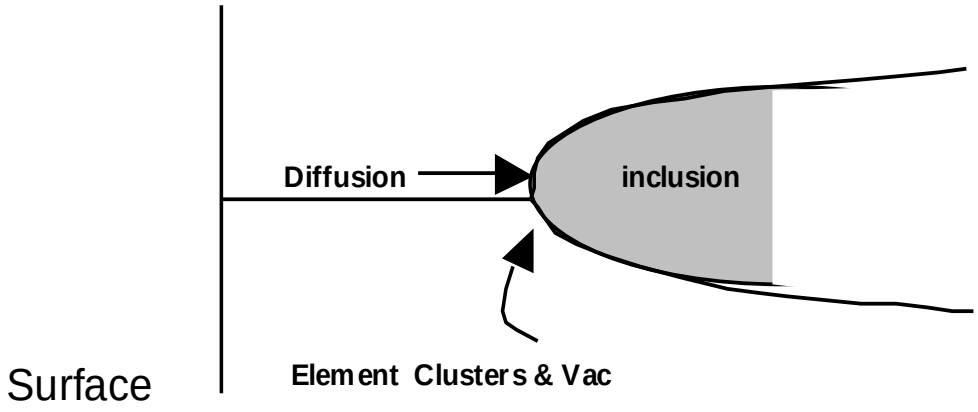

Figure 38. Void formation thru element clusters and vacancy annihilation

C.L. White also contributed to the discussion of BIG fracture occurring during creep of single-phase nickel alloys. Studies during the period suggested that low melting grain boundary phases were not necessary for impurity induced BIG fracture. This was demonstrated not to be the case. Void formation by athermal nucleation occurring during plastic deformation formed W-type and P-type cavities on highly stressed grain boundaries. Between the extremes of high stress-low temperature and low stress-high temperature, both types of cavity nucleation were found. Cavities, once nucleated, grow by either localized plastic deformation or by diffusion mechanisms. Localized plastic deformation is favored in triaxial stress state or in high stress conditions. Auger maps clearly demonstrated higher sulfur concentrations on grain boundaries where cavities were nucleated. Furthermore, ductile regions where fracture was by micro void coalescence were free of sulfur while flat fracture regions showed high sulfur

concentrations. White concluded that his study provided clear evidence of trace element segregation to cavity surfaces in all cases of high temperature-intergranular fracture. Figure 39. below, illustrates key elements of the segregation crack nucleation and formation.

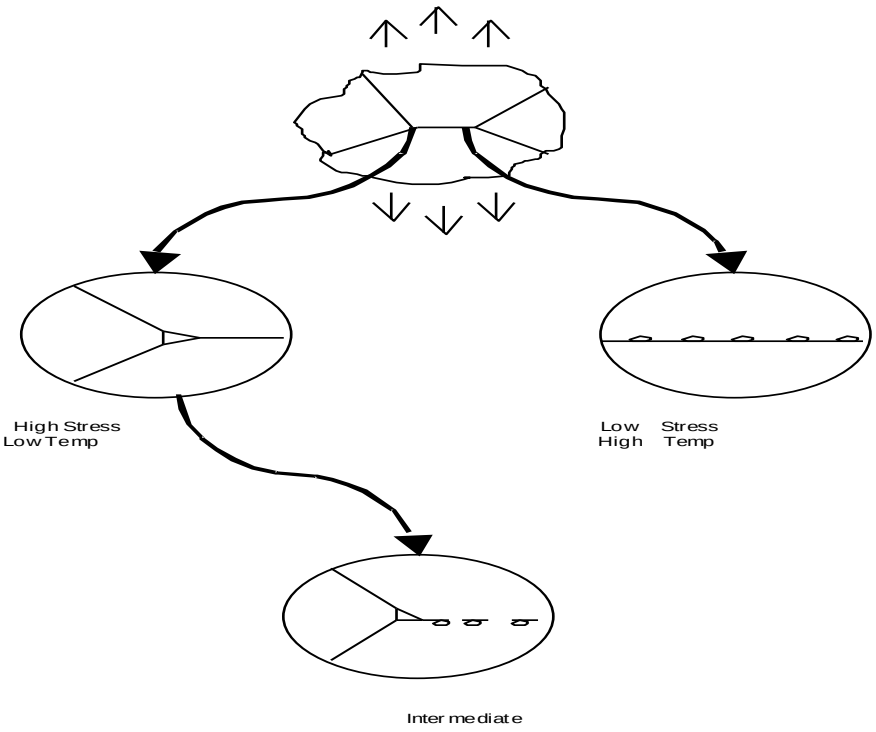

Figure 39. Schematic of cavity formation of big fracture w-type, r-type, and intermediate

In addition, White summarized the work of others who were researching the consequence of ppm level of sulfur impurities in nickel base alloys. He related impurity levels, and loss of ductility and temperature of exposure reflected in the percent reduction in area.

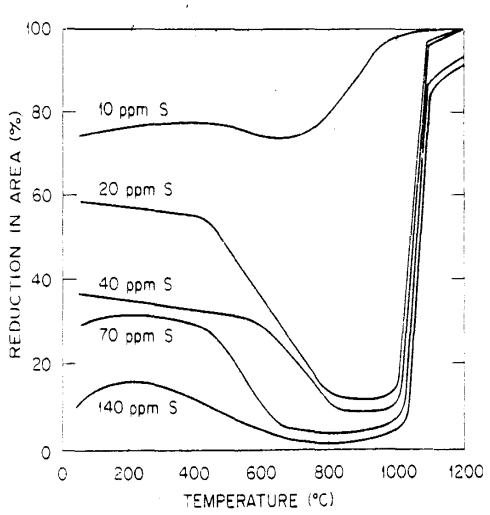

Figure 40. Sulfur influence on ductility with temperature

The graph in figure 40 shows both a monotonic loss of ductility when sulfur in nickel alloys increased from 20 ppm to 140 ppm. In addition, it shows, that sulfur content causes a significant ductility dip in the temperature range between 500 ^{o}C and 900 ^{o}C. Above 1000 ^{o}C there is a dramatic increase in ductility for all concentrations of sulfur to values well above those found at temperatures below the ductility dip. Significantly, the ductility dip occurs at temperatures where many designs using nickel base alloys call for superior performance. It is easy to understand why specifications for nickel base alloys set a limit of sulfur at 15 ppm maximum. If it were economically and practically achievable, data suggests a limit on sulfur below 10 ppm would provide a margin of safety and prevent BIG fracture associated with this ductility dip.

1987 was a banner year for publications regarding BIG fracture. Scanning Auger spectroscopy (AES) provided a powerful tool for investigating fracture surfaces. Investigations of grain boundary embrittlement were completed

evaluating the solutes hydrogen and sulfur in pure nickel, and sulfur, phosphorous, oxygen, and carbon in a 2 ¼ Cr 1 Mo steel. BIG fracture was recognized as a separate and unique fracture mechanism involving stress-assisted concentration of one or more of the impurity elements that segregate to GB or at crack tips and diminish cohesion.

Lassila studied both sulfur and hydrogen embrittlement of grain boundaries in pure nickel. Temperature was used to control the mobility of hydrogen. Evaluating the concentration of segregated hydrogen is difficult. One method to qualitatively identifying concentrations of segregated hydrogen are to use Tritium as the hydrogen source and track concentration with autoradiography. Secondary Ion Mass Spectroscopy (SIMS) has also been used to detect concentrations of hydrogen on grain boundaries. Lassila was able to determine threshold concentrations for hydrogen necessary to produce BIG fracture using AES. Threshold concentrations needed to effect the change in fracture mode were shown to vary with temperature. Furthermore, the critical concentration fell when sulfur was also present. Monolayer segregation of sulfur alone did not appear to produce BIG fracture. Lassila also reported, that the presence of oxygen or chromium oxides confounded Auger measurements when samples were fractured in air. Finally, Lassila suggests clustering within the “Embedded Atom Model” or “Decohesion Model” as the basis for loss of bond strength causing low ductility and basis for BIG fracture in the pure nickel studied.

Lewandowski and Hippsley explored BIG fracture produced in vacuum. They implicated solute sulfur segregation to the grain boundaries as the cause for the loss of cohesion. However, indirect measurement of crack growth rate in 2 ¼ Cr 1 Mo commercial grade and phosphorous doped steel under sustained load in the temperature range of 500-650 ^{o}C showed a 2X faster growth when tested in air versus tests in vacuum. Various heat-treatments were used to control the amount of free sulfur in solution. Finite element stress analysis of the plastic zone ahead of the crack tip predicts a peak stress 85 μ ahead of the crack tip under plane strain conditions in the samples tested. From observations of sulfur and oxygen concentrations and stress calculations, it was concluded that in the hydrostatic tensile stress field ahead of the tip sulfur segregated to the grain boundary. Finally, Hippsley suggested that sulfur retained in solution was involved in advancing BIG fracture even though MnS particles existed on or near grain boundaries.

Hippsley extended the previous study with definitive data supporting sulfur in solution as the source of interface decohesion supported with exceptional results characterizing enrichment ahead of the crack front. Crack surfaces in both transgranular and intergranular regions were studied in both vacuum and partial pressure of air from 10^{-9} to 10^{-3} torr. Sulfur enrichment was observed to be highly localized. Sulfur exhibited a general segregation to the growing crack surfaces and a significant concentration in the plastic region ahead of the crack front. Oxygen in intermediate concentration (pressure) played a role in enhancing sulfur segregation but also competed with sulfur for surface up to 15-

25% O coverage. The oxygen coverage conforms to pressures of air of $1*10^{-4}$ to $5*10^{-4}$ torr. Test data definitively supports the “pure drift” model of BIG fracture and suggested refinements to that model using finite element stress analysis to develop the illustration figure 41.

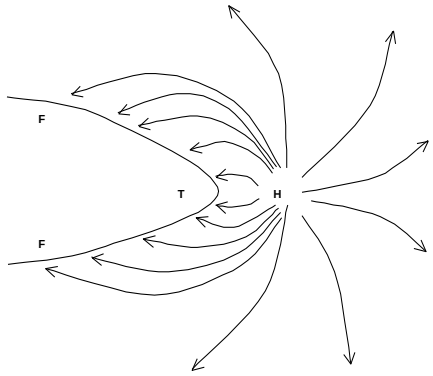

Figure 41. Solute flow direction in notch stress field h-position of maximum hydrostatic stress, t-crack tip, f-crack face

Firm conclusions regarding spatial embrittling effects of sulfur concentrations ahead of the crack tip were difficult to make. No evidence was found to favor general decohesion with the crack moving continuously; rather, fractographs suggest step-wise propagation with occasional evidence of some localize flow. This interpretation is in line with other mechanisms of impurity affected decohesion. In these models, slower strain rates allow the impurities to move to the critically affected regions of stress.

Kameda explored BIG fracture in a nickel base superalloy with methods similar to Hippsley. In this research, commercial lots of the nickel alloys with high concentrations of Zr, and B were paired with high and low sulfur concentrations. SIMS examination of grain boundaries at different distances from the crack tip led

Kameda to conclude that the “pure drift” model applied to segregation of the sulfur to the embrittled interface. Both Zr, and Ti formed sulfide compounds and concomitantly limited the amount of sulfur segregation. Boron on grain boundary surfaces limited embrittlement by sulfur, this effect was attributed to a site competition mechanism.

In 1997, Paul G. Shewmon gave the Edward DeMille Campbell Memorial Lecture at the American Society for Metals International Convention. Grain Boundary Cracking, the lecture subject, chronicled metal working experience and the development of metallurgy from as early as the 16th century to modern times. Liquid metals, vapors and trace element solutes (H, O, S, & P) all generate fractures with low ductility. The influence of temperature and strain rate are crucial to void formation. Void nucleation and subsequent growth are two separate phenomena, with different activation energies and mechanisms.

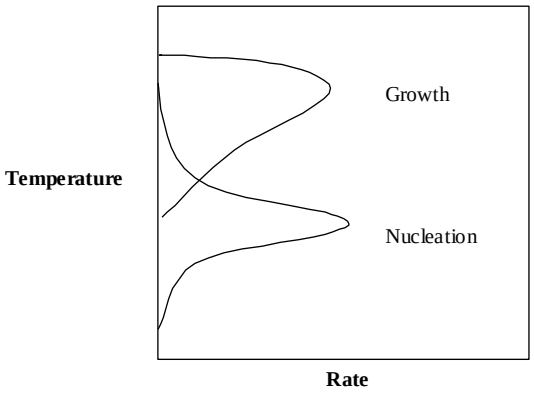

Figure 42. Schematic representation of the rate of nucleation and growth in a condensed phase, after Doremus R.H.[32]

Polycrystals deform under the influence of stress and strain through a number of mechanisms. It involves the complex interplay of dislocation motion

and interaction, of vacancy formation and annihilation, of precipitate nucleation and growth, and ultimately micro void nucleation and growth as modified by the transport of active elements to the growing surface. Theory of crystal modification suggested improving strength by blocking or retarding dislocation movement. Stronger alloys created by adding atoms in solid solution that stretch or pinch the lattice or precipitate new phases within the crystal all impede easy flow to improve strength. Shewmon invoked the strong alloy and stress concentration concepts to support why brittle intergranular fracture occurs. This approach neglects strain-rates or the reasons why trace element solutes segregate and concentrate in regimes where BIG fracture prevails, and those contributions of segregation to fracture.

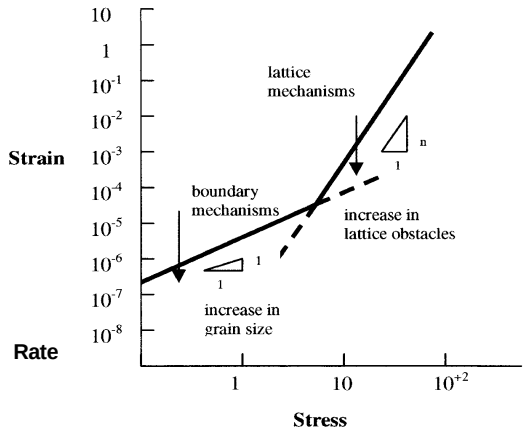

Figure 43. Dominant flow mechanisms related to stress and strain rate (arbitrary units)[69]

Mechanisms of plastic flow as viewed by Landon shown in the schematic in figure 43, correlate stress-and-strain rate with polycrystalline structure and regimes observed in various alloys. Slower strain rates favor grain boundary flow at lower

stress and alternately higher strain rates in concert with higher stress bring lattice mechanisms into play. Arrows indicate the general shift in the line with transformation in regime and microstructure and GS and precipitation. While these relations are valuable in predicting the influence of alloy adjustments or design space, it neglects any means to consider influence due to changes in temperature.

Investigation of BIG fracture advanced in 2003 when Nissley, et al., reported development of the “Strain-to-Fracture Test” (STFT). This test targets ductility dip cracking and other elevated-temperature crack growth phenomena. STFT is robust allowing changes in test parameters to identify material conditions affecting cracking. Programed test envelopes performed using a Gleeble offer advantages of being conducted in selected environments. Ductility dip cracking (DDC) studied using STFT provide engineering data from rapid tests that are highly correlated to actual production conditions. Rapid cycles of heating and cooling experienced in welds, thermal cycles in aircraft turbines during take-off and climb and in environments in power turbines at peak load conditions are three design regimes where STFT of austenitic alloys improve crucial engineering knowledge.

Coherency strains associated with disregistry or mismatch between the crystal lattice of the austenite matrix (γ) and gamma prime (γ') precipitates have been used to explain the hardening of the γ'-strengthened alloys. Maniar

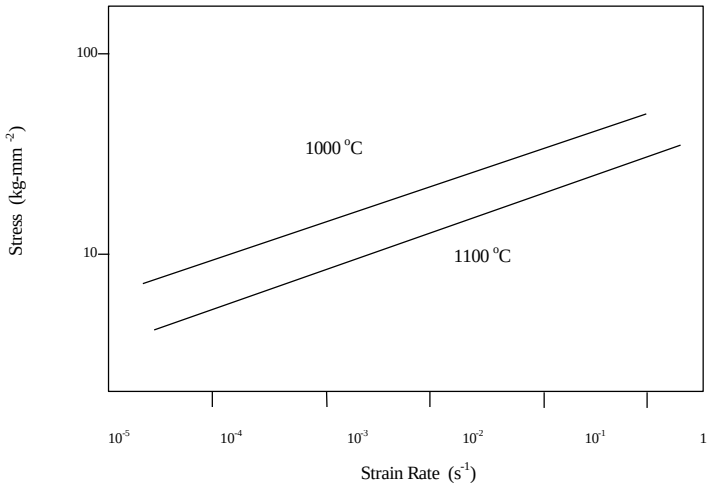

Figure 44. Strain-rate dependence of flow-stress for C263, a nickel base superalloy, data from tensile and torsion tests, correlation using Von Mises criterion[78]

measured the effect of γ-γ' mismatch on mechanical properties as a function of composition. Mismatch was adjusted by varying the ratio and total amount of the γ' formers aluminum and titanium[34]. In some heats the alloy was adjusted and both iron and molybdenum substituted for a few per-cent of the nickel in the γ'. In stress rupture tests, these heats demonstrate reduced ductility correlated with an increase in the precipitate (γ') matrix (γ) mismatch between the crystal lattices.

5.7 SEM Fractography

Fracture surfaces of Gleeble samples were imaged in an Amray 1800 SEM. Images were studied to discern relevant features indicating mode of fractures in tested samples. SEM images are a well tool for documenting and identifying fracture morphology. These 3-D morphologies can then be used to correlate test conditions with failure mode. As an example, it was found that

ductility loss followed the monotonic reduction in strain rate in the samples that were exposed to the TEOS and Hydride environments. Selected SEM results are presented in this section illustrating the identified features related to flow and fracture.

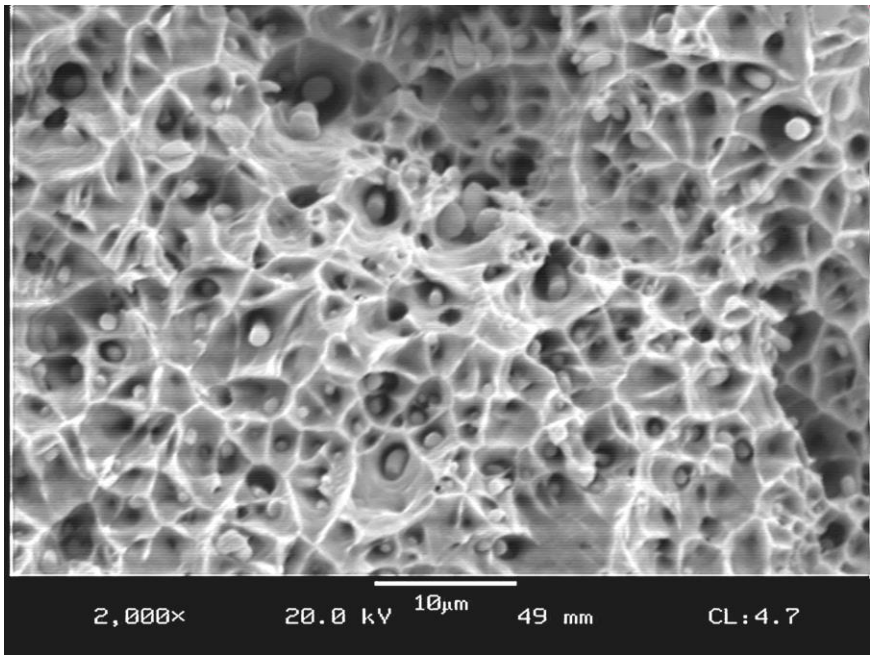

Figure 45. Fully ductile equiaxed dimples clearly illustrating particles associated with nucleation of the dimples,[27] (rod, 0.0005 sr, 1022 ^{o}F)

In figure 45, the equiaxed dimples are typical of void coalescence occurring in the center of a tensile bar under plain stress. Figures 46, and 47 show the change in shape of the dimples as the global stress state changes from the plain stress at the center of the tensile specimen to shear at the outer edge. Elongated shear dimples occur on the shear lip of the fracture sample. Fracture in this case is fully ductile with each void plainly initiating at a second phase particle. Using the

energy dispersive spectroscopy large amounts of sulfur were found in the elongated cavities indicating these are sulfide stringers. Disk and symmetrical particles are likely carbide; EDAX could not confirm this observation.

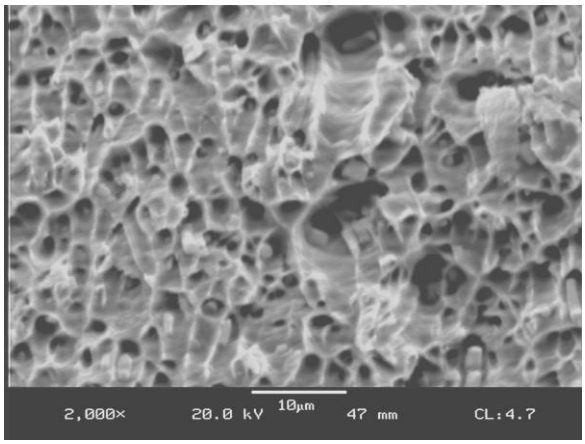

Figure 46. Shear dimples observed at a distance half way between the central equiaxed fracture zone and the sample edge,[27] (rod, 0.0005 sr, 1022 ^{o}F)

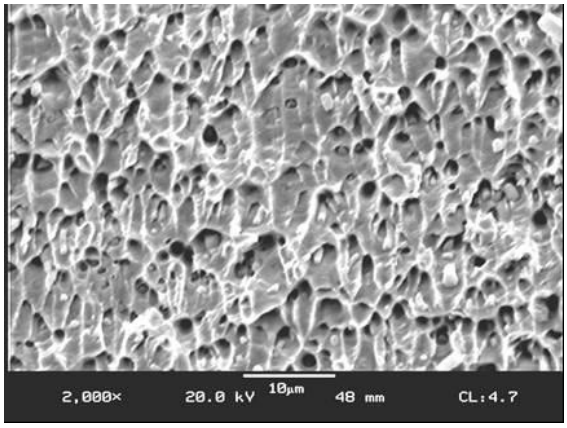

Figure 47. Elongated shear dimples illustrating ligament stretching of dimples located in the shear lip near the edge of the tensile specimen,[27] (rod, 0.0005 sr, 1022 ^{o}F)

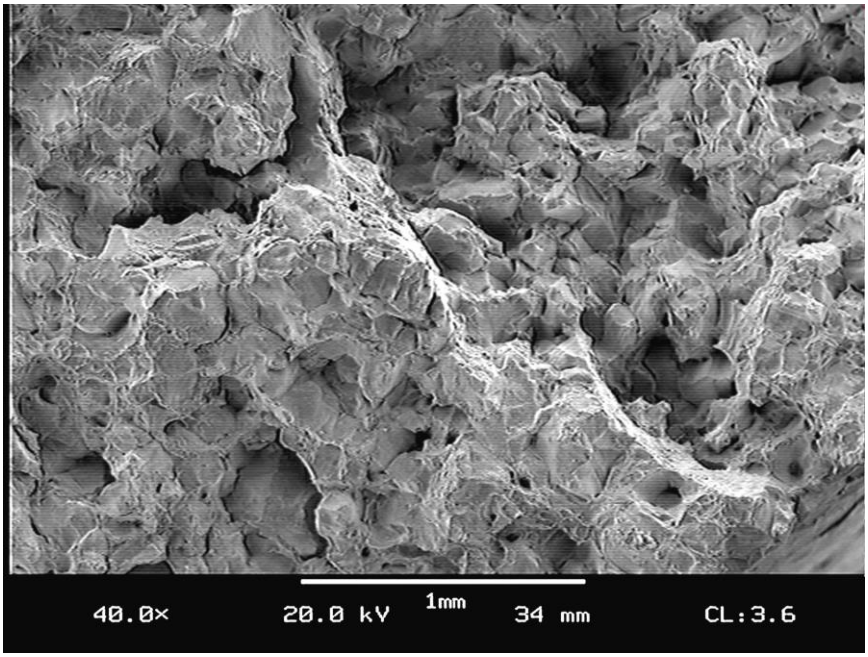

Figure 48. Intergranular fracture 40X (hydride, 0.00005 sr, 1295 ^{o}F)

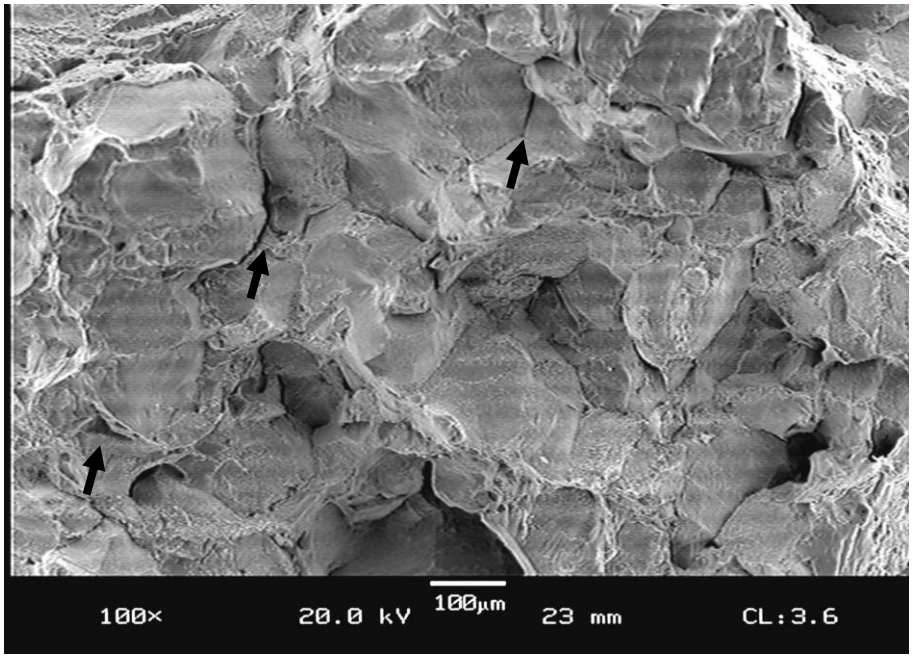

Figure 49. Intergranular fracture at higher magnification 100X, arrow points to possible w-crack surface, (hydride, 0.00005 sr, 1295 ^{o}F)

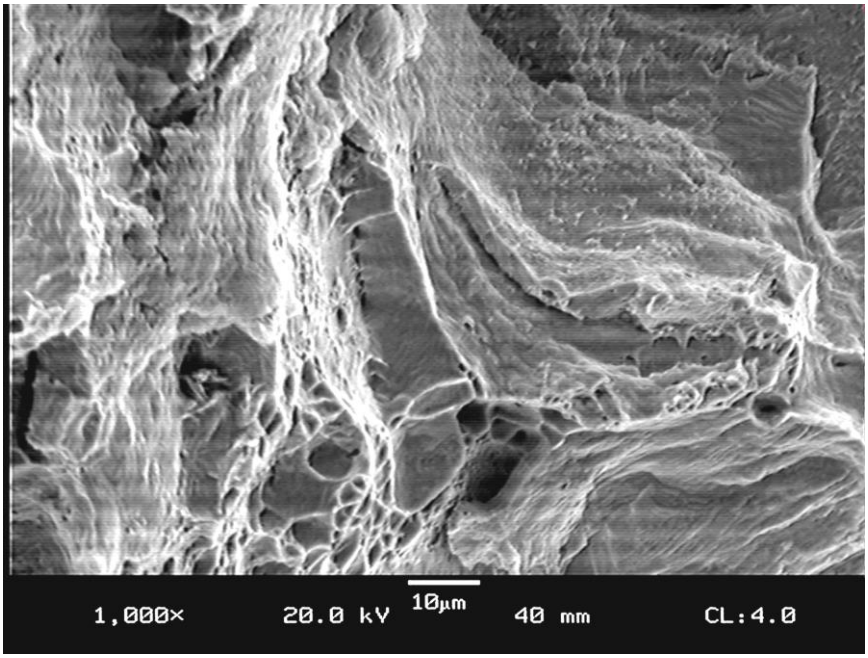

Figure 50. Ductile fracture with duplex void size and an area of ridging

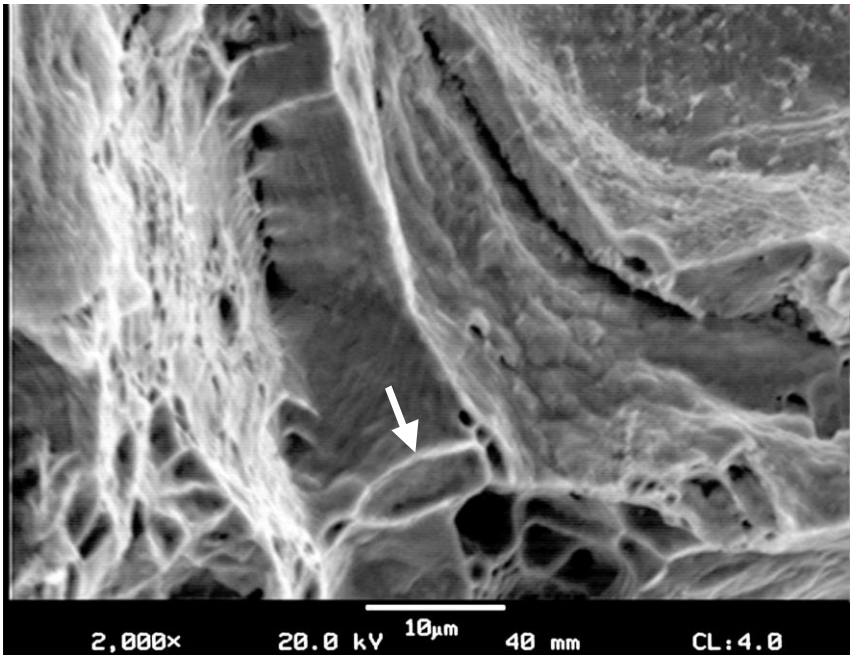

Figure 51. Ductile fracture with duplex (large and small) voids at higher magnification, arrow points to texture in a large void due to streatching[27,30]

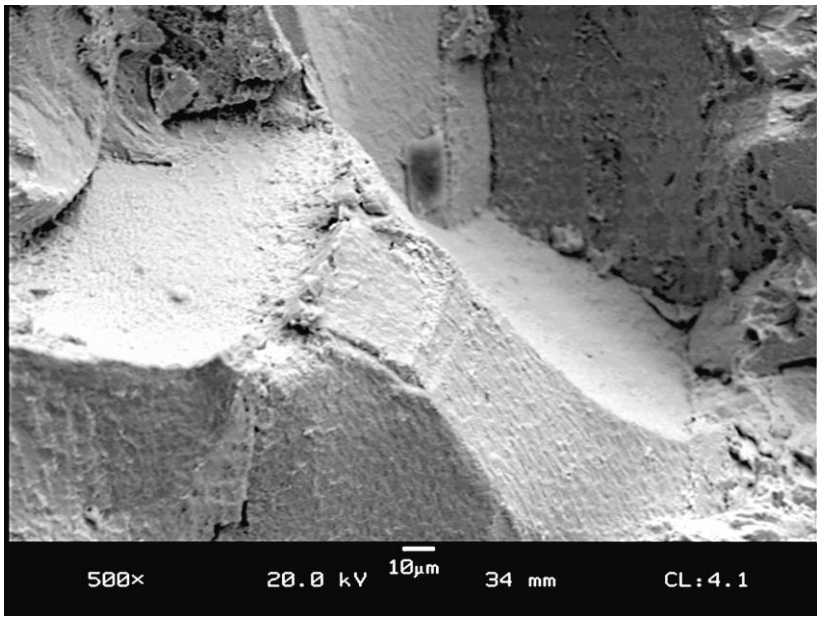

Figure 52. IGF initiated at what appears to be carbides, (teos 0.00005 sr, 1292 ^{O}F)

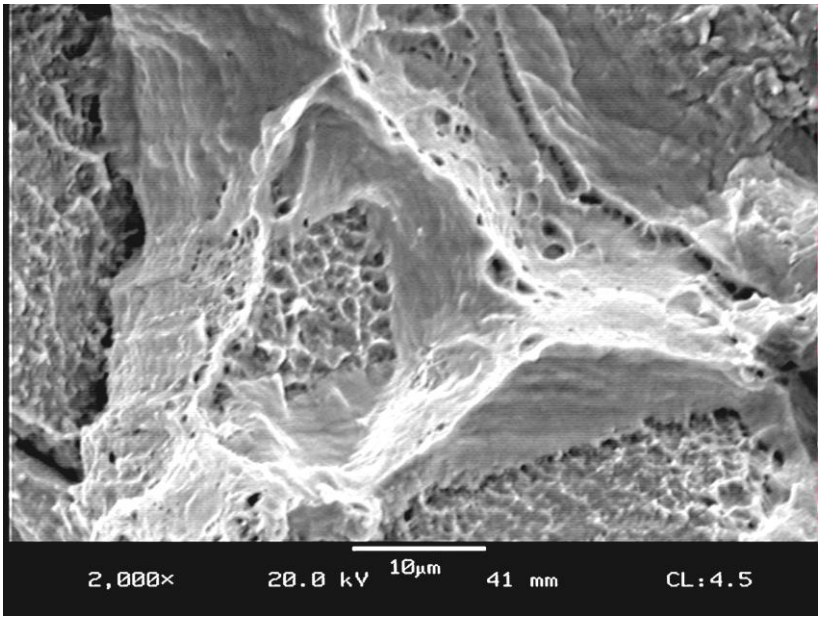

Figure 53. Mixed mode fracture, note the fracture following straight twin-boundary fracture and very fine VC[33] r-type and an igf at a triple point due to grain boundary sliding–x-type, typical of intermediate stress, moderate strain-rate, and temperature[33]

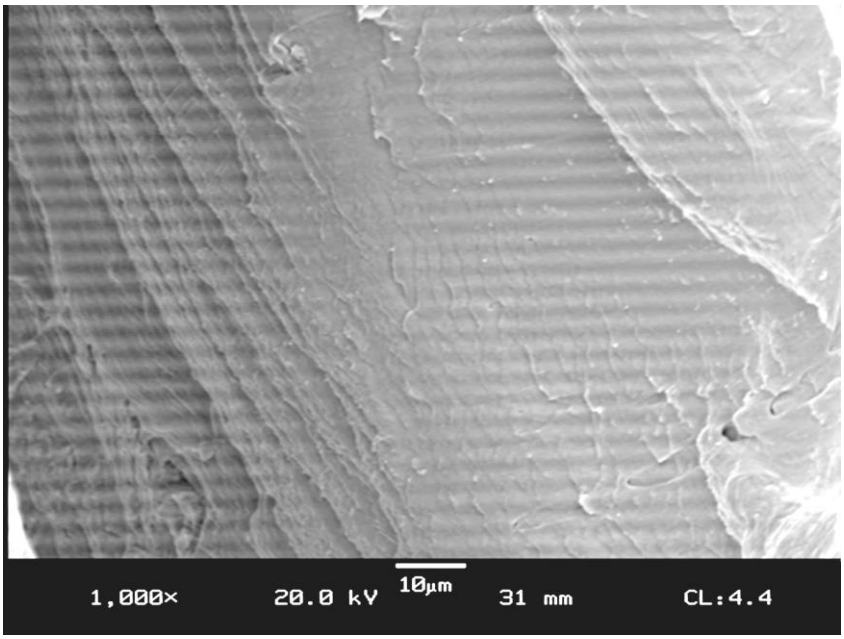

Figure 54. Smooth featureless fracture for what appears to be an igf at a triple point separation due to GB sliding

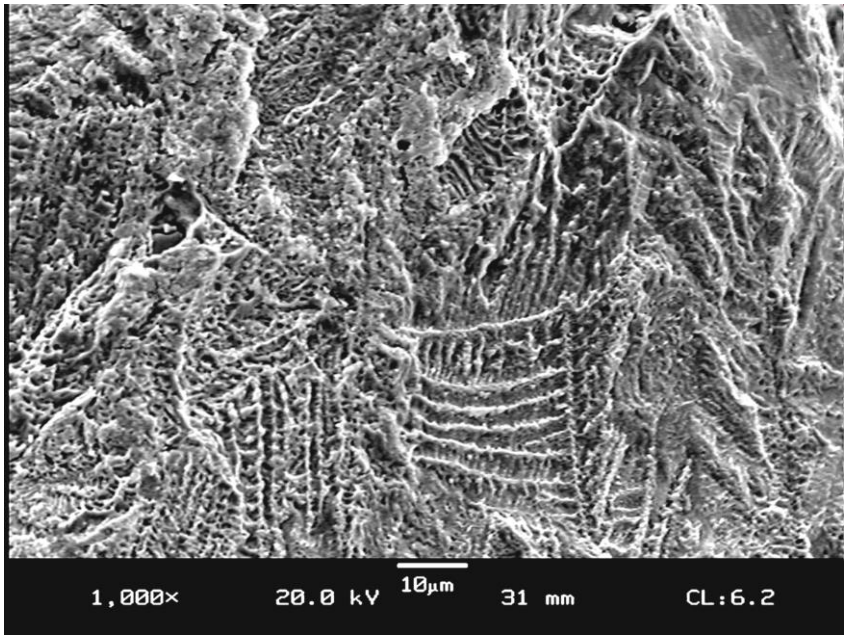

Figure 55. Transgranular fracture with quasi-cleavage along slip bands and tear ridges with locally micro ductility at MVC and very fine precipitates (carbides or gamma prime)

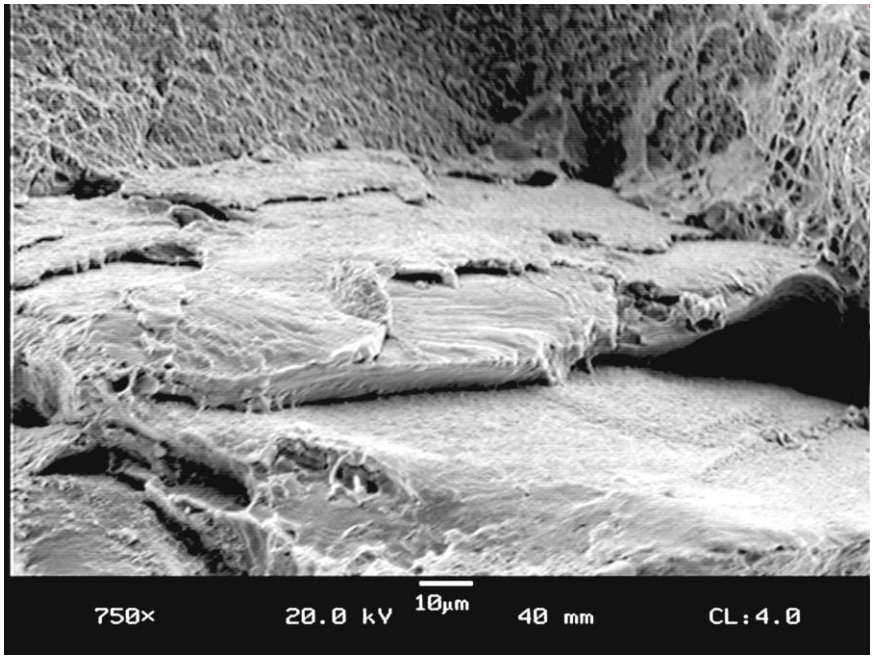

Figure 56. Mixed mode fracture, illustrating very fine ig void coalescence and cleavage, this fracture has local ductility but is brittle on a macro scale [26,27,33]

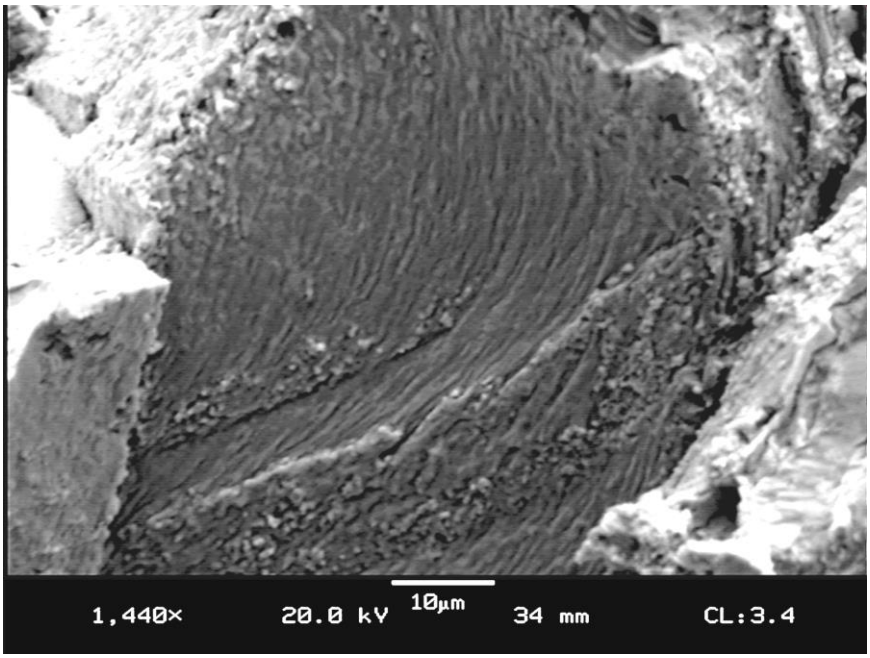

Figure 57. Transgranular fracture where slip traces show a flow distorted grain

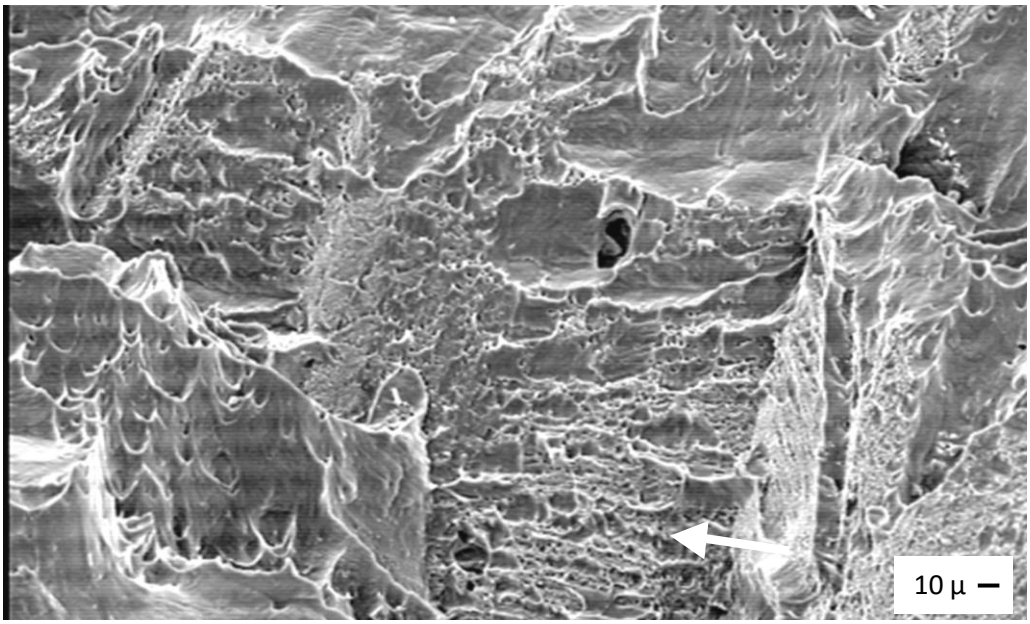

Figure 58. Transgranular fracture with markedly different micro-void sizes, arrow indicates tear ridges

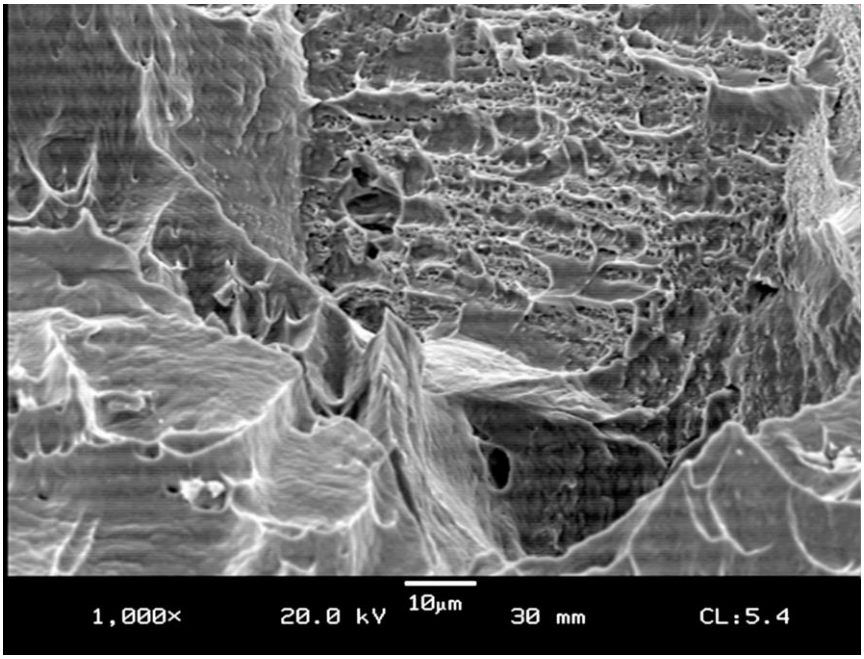

Figure 59. Region below arrow in figure 58, note the large difference in micro-void size

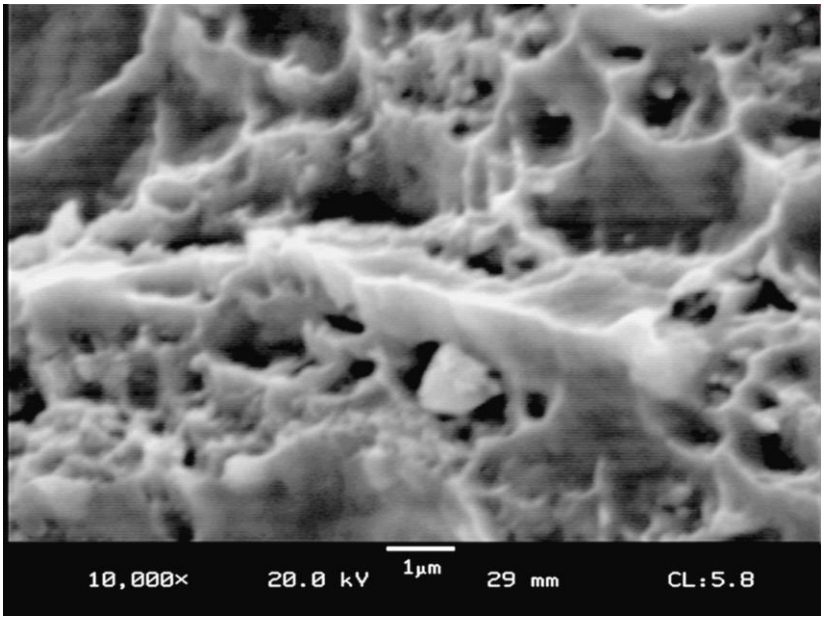

Figure 60. Central region of figure 58 showing the hyperfine void coalescence (10,000X), note the very fine second phase particles (carbides & sulphides) where the voids are nucleating

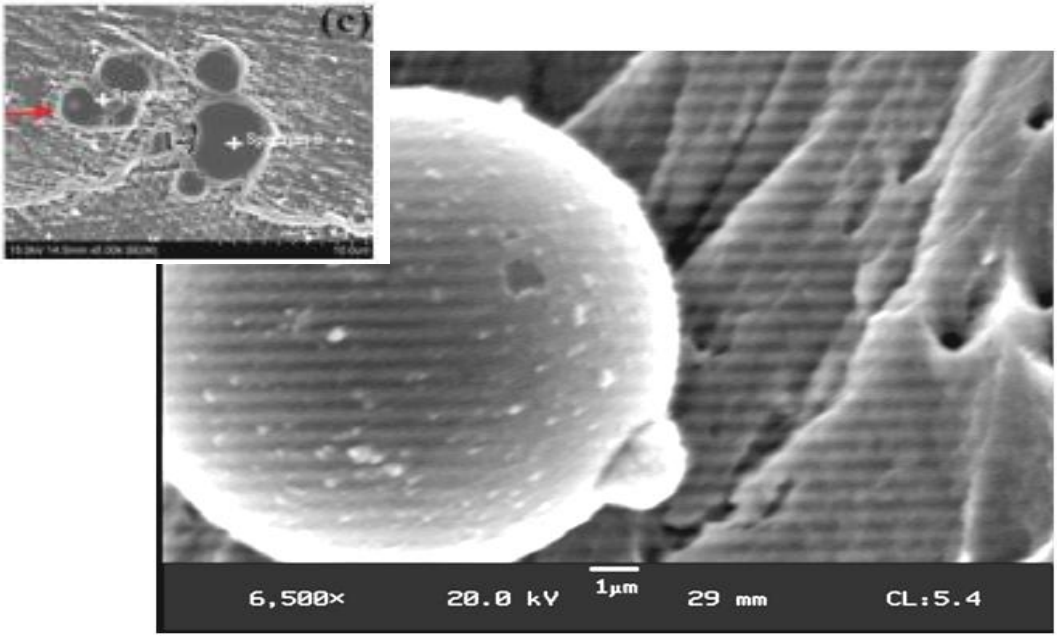

Figure 61. Possibly large M_6C secondary carbide morphology nucleating separation and fracture, note elongated shear dimples

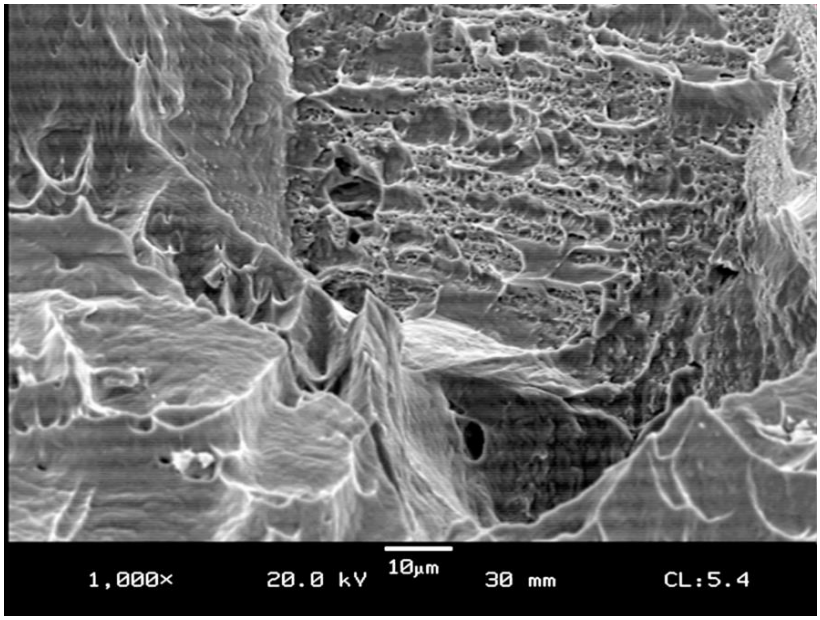

Figure 62. Repeat of figure 59 to emphasize mixed mode fracture with duplex mv size, in the central area are tear ridges of small mvc following slip bands with fracture either around gamma prime ppt. or carbides, typical of intermediate strain-rate and intermediate temperature

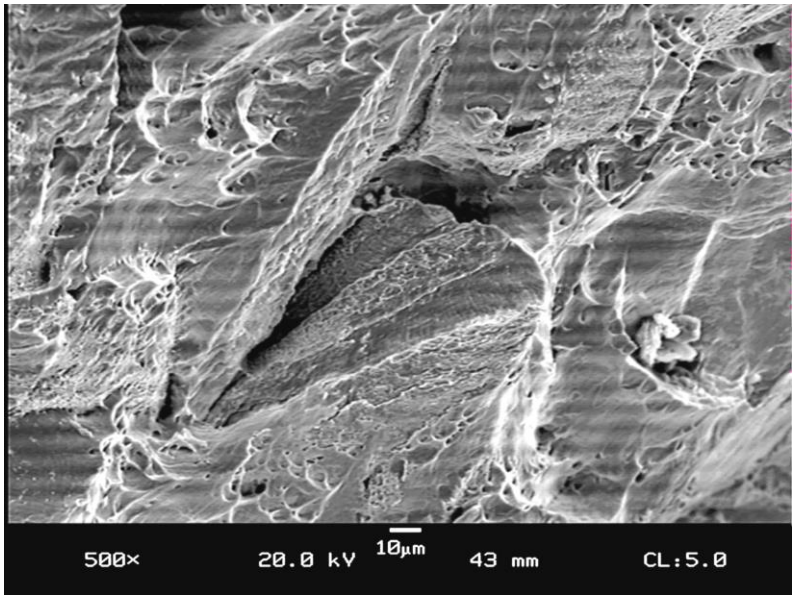

Figure 63. Transgranular fracture with multiple void sizes and what appear to be facets initiated at twin-boundaries

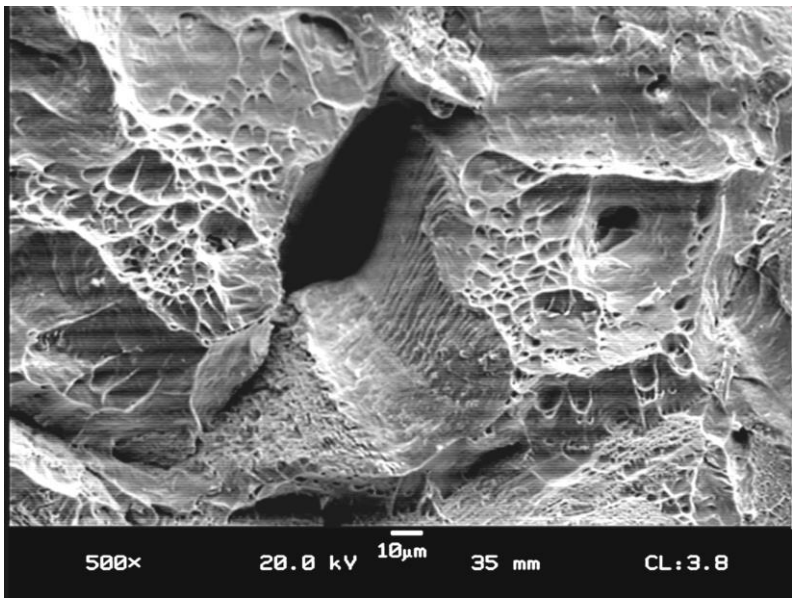

Figure 64. Mixed mode fracture with about equal amounts of igf and transgranular mvc with fracture initiating along steps in slip bands, teos 0.5 strain rate, temperature 1195 ^{o}F – fast strain rate at high temperature

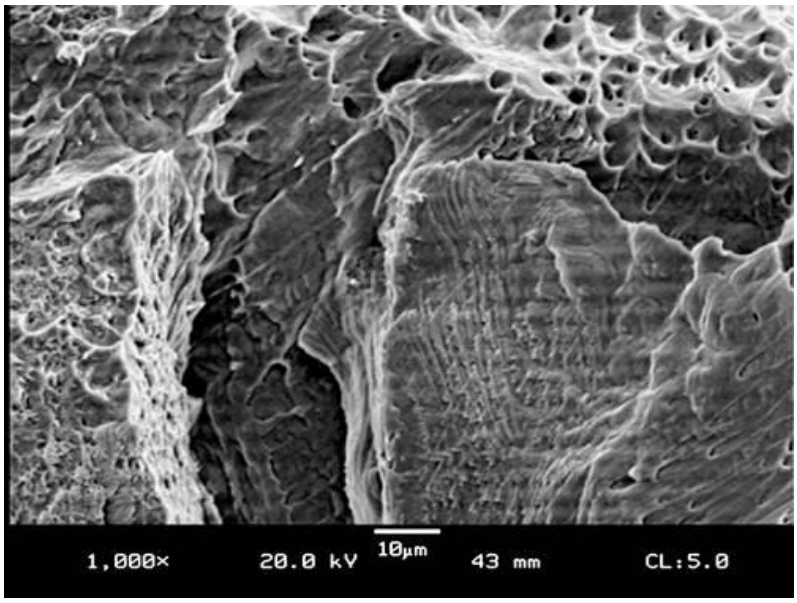

Figure 65. Mixed mode fracture with more igf and finer mv and tear ridges than the previous figure, teos, 0.005 strain rate, temperature 1195 ^{o}F – litermediate strain rate at high temperature

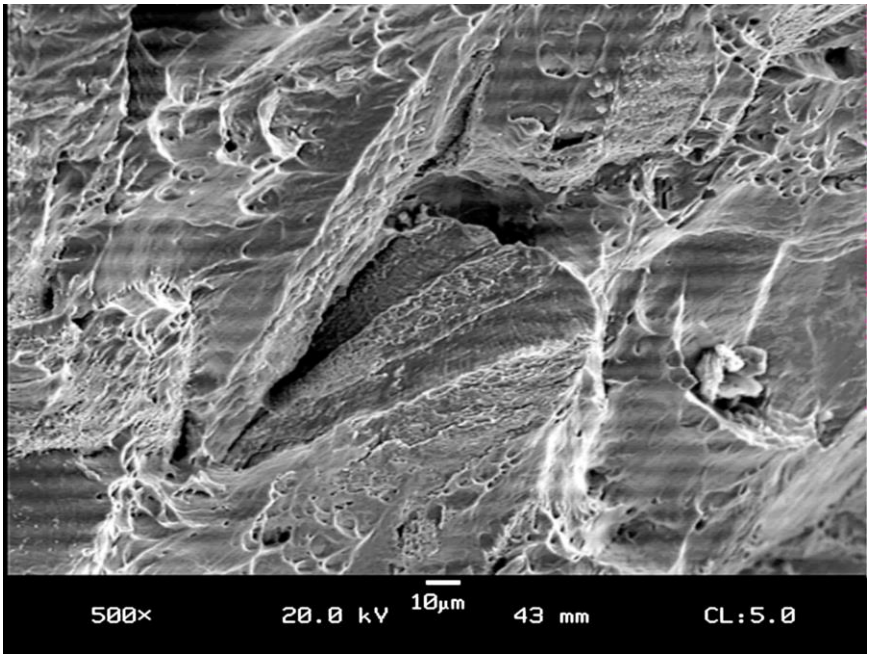

Figure 66. IGF with smooth gb surfaces or very, very fine mvc, w-voids are found at flat triple point intersections and evidence of fracture initiation along twin-boundaries, teos, 0.00005 strain rate, temperature 1195 ^{o}F

5.8 Overview

As described previously, when at operating temperature, a super-alloy exists in a state of white-hot dynamic chemical equilibrium. With the presence of either temperature gradients or mechanical load, the alloy is also in a state of dynamic change at the atomistic level through diffusion and dislocation movement. Achieving a metallurgically stable microstructure when at temperature is recognized as an important objective. Stable microstructure and predictable strength go hand-in-hand. A Superalloy must function in a regime best characterized as anisotropic, discontinuous and non-equilibrium. In this state, strain, strain-rate and temperature must be identified and controlled to guarantee

the mechanical properties and prevent undesirable flow and fracture. In the regimes studied, loss of ductility and a change in fracture mode from ductile to intergranular occurred when the strain rate of the test was slowed from 0.5 $-S^{-1}$ to 0.00005 $-S^{-1}$. This demonstrates at least one aspect of possible active causes to the loss of ductility and BIG fracture. Gleeble simulation of thermal gradient, temperature and strain rate to match actual conditions experienced in use is a valuable tool for the engineer. Simulation with a close approximation to actual operation provides data to improve design and a means to better understand alloy behavior which is otherwise unavailable.

The kinetics associated with microstructural change in a state of dynamic equilibrium can be altered by applied stress or by continuous strain. The kinetics are often more rapid under such conditions. TTT diagrams show how the nucleation and growth of phases change with temperature and time. The TTT curve for Inconel 617 (figure 67) is a close approximation to that of Inconel 601. It illustrates changes in the microstructure with temperature and time.

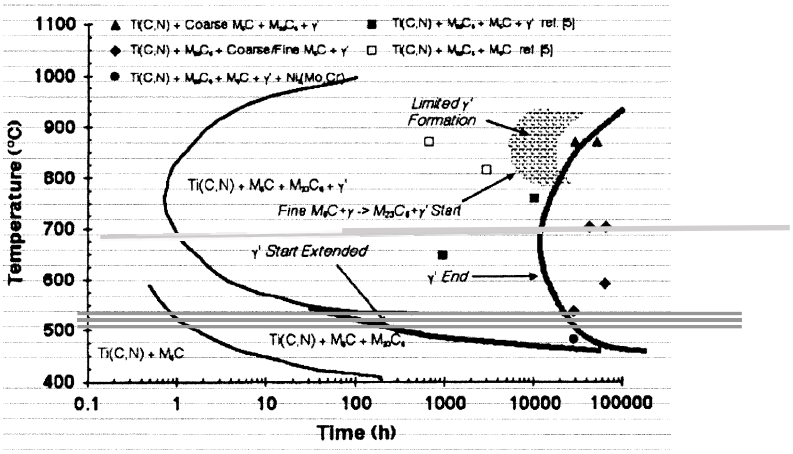

Figure 67. TTT diagram (c-curve) γ' and carbide formation nickel alloy 617, (report ASME B & PV code section III, 2013)

Microstructure at temperatures above 0.4 T_m are subject to dynamic change. Those microstructure changes are illustrated figure 67 show why the term metastable is so often applied to these alloys. Short term or aging tests used to establish conventional properties often do not account long-term property changes in various time temperature regimes or associated with use or in the mechanical design analysis. Between the gray band of horizontal lines highlights the region of Gleeble tests for the TEOS and Hydride test samples.

TTT diagrams present those changes in microstructure related to temperature and time at temperature below a solvus. They do not include directly the various effects of processing or service conditions. Although they may be developed to map these effects. In developing the TTT plot a TMT (thermo-mechanical treatment) is performed then given a specific heat-treatment followed by a quench to freeze microstructure. Then the values of quantitative metallography are plotted. Some TTT summaries use only hardness as the quantitative metric for changes in structure.

Applying TTT to this work, several changes to microstructure during the test are indicated. For instance, $M_{23}C_6$ carbides may be replacing unstable primary MC carbides, and at longer exposure M_6C + austenite combines and precipitates $M_{23}C_6$ carbide and gamma prime. Also carbides will be becoming coarser and go into solution. Gamma prime will also Ostwald ripen and will be become coarser. Phase change reactions indicated by the TTT are thermodynamically driven and are diffusion limited with activation energies in the range of that for nickel self-diffusion. Kinetics of the phase change is typically found to follow the Power Law

model. Under the influenced of applied stress and various imposed strain-rates, kinetics are often accelerated.

At the atomistic or crystalline scale, mobile dislocations provide the means for the crystal structure to accommodate stress. Frost has summarized flow regimes and illustrated the key competing dislocation patterns (figure 68). His work brings together the work of many researchers and organizes findings into a tractable summary.

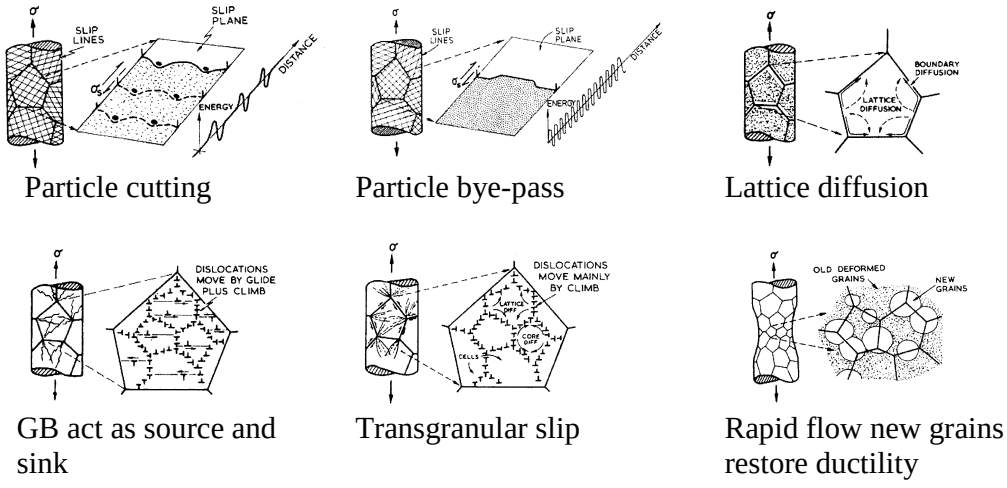

Figure 68. Illustrations of various mechanisms of dislocation contributions to flow[77, 82]

Each of the illustrated dislocation movement mechanisms operates to accommodate stress and facilitate flow within different regimes of stress, temperature and strain-rate. Resistance to easy glide begins by pile up of dislocations followed by climb (a diffusion-limited process) as a crystalline scale adjustment to macro scale strain, strain-rate or temperature. Dislocations blocked by precipitate phases must climb to either operate on different planes or cut

through the particles. Particle cutting of gamma prime has been identified as occurring by dislocation pairs forming an antiphase (partial dislocation pairs) boundary within the particle. Gamma prime is unusual as the Ni_3Al is know to increase in strength with increasing temperature and thus the particle cutting becomes more difficult at higher temperatures until the particle goes into solution. In addition, growth of the precipitates would increase the anti-phase boundary energy required to cut through larger gamma prime precipitates. Various modes of dislocation movement, acting in concert, develop accumulated damage ultimately leading to crack formation and fracture.

5.9 TEOS and Hydride

In base line tests of strain-aged samples, both strain-rate and temperature were found to lower ductility (Figures 27 & 28). A minimum of ductility was found at temperature of 850 ^{o}F and recovery of ductility increasing above 900 ^{o}F. Gleeble plots (figures 69 & 70) for test at a temperature of 1295 ^{o}F for stroke vs. load show a monotonic reduction in flow to ultimate load with decreasing strain rate. This profile suggests a diffusion-regulated accumulation of damage. These tests were done at a temperature 400 ^{o}F above where Inconel 601 was found to recover ductility. Recovery of ductility, as found in the base line tests, can be explained by re-solutioning of carbides and increase in diffusion rate thus freeing dislocation movement with increased climb through faster diffusion.

This was not the case in the Hydride and Teos samples. Reduction in area was lower at 1292 ^{o}F than base line for both conditions (Hydride & Teos). Changes

to alloy microstructure and damage accumulated during exposure would account for these lower values.

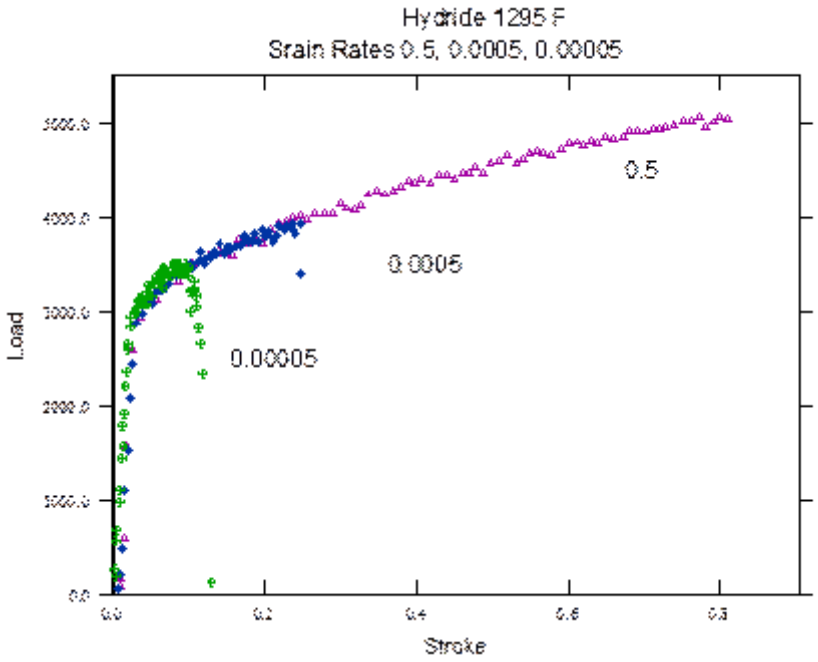

Figure 69. Plots, gleeble stroke vs. load at 1295 ^{o} F, 3 strain rates, hydride

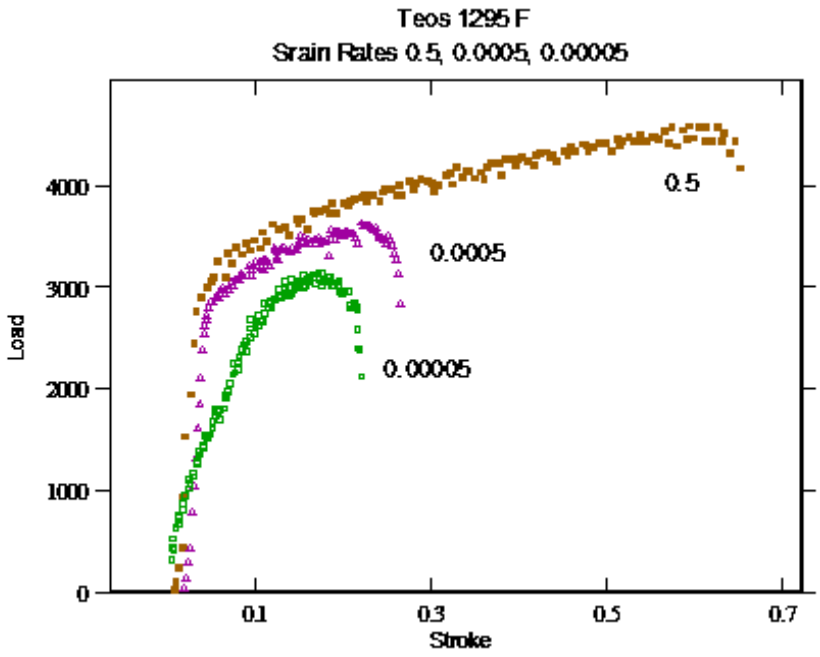

Figure 70. Plots, gleeble stroke vs. load at 1295 ^{o}F, 3 strain rates, teos

However, alloy damage, does not by itself explain the significant difference between values found between the two exposures. Clearly, flow and fracture differ with the exposed conditions although there is similarity. Hydride test values with decreasing strain-rate are consistent with each test following similar flow. Similarity of flow regimes in the hydride tests is seen in overlaid plots (figure 69). Teos displays different flow characteristics with differing flow paths as strain rate decreases and presenting lower value of proportional limit as well as ultimate (figure 70). At the slowest strain rate there is apparently a change in modulus; this change in modulus can be an artifact of the test if there was a slipping of the sample in the jaws or a subcritical growth of a flaw. Replication would be the approach to resolving this anomaly in the data but additional samples were not available.

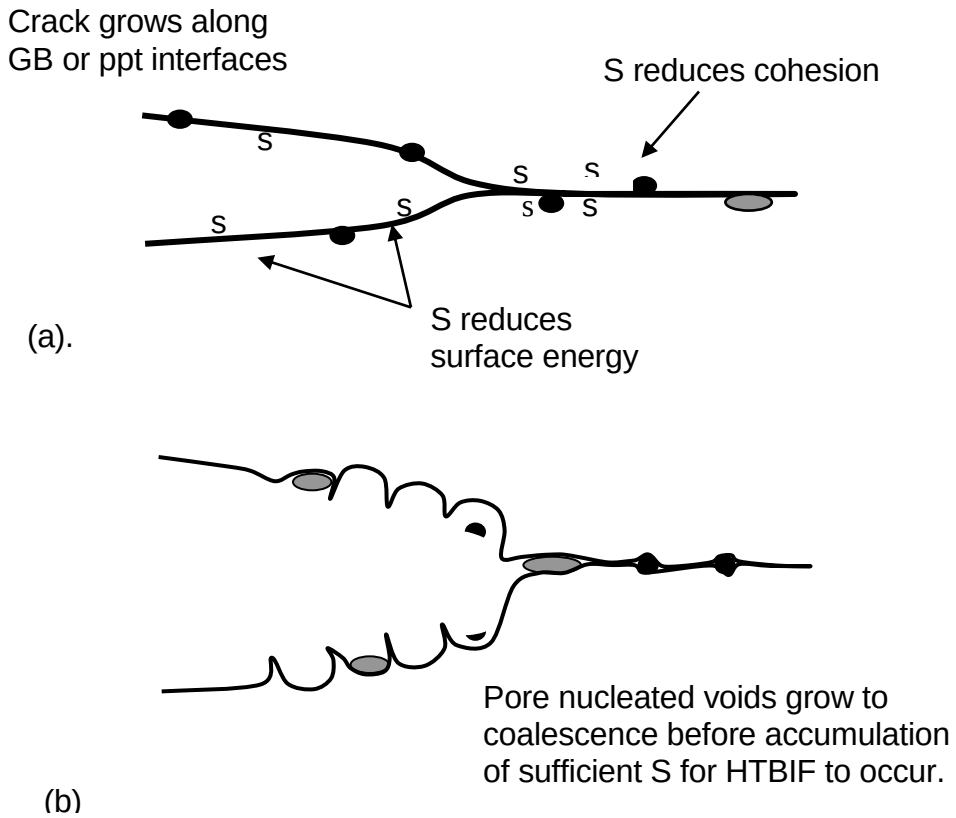

Figure 71. Schematic diagram illustrating mechanisms proposed by Hippsley C. A., for high temperature brittle intergranular failure in austenitic steels when damage rate is slow, A and B above, show the transition to intergranular micro void coalescence (mvc)

The difference in location for MVC can be associated with the degree of MVC found at a sliding grain boundary or where precipitates are incoherent within the austenite.

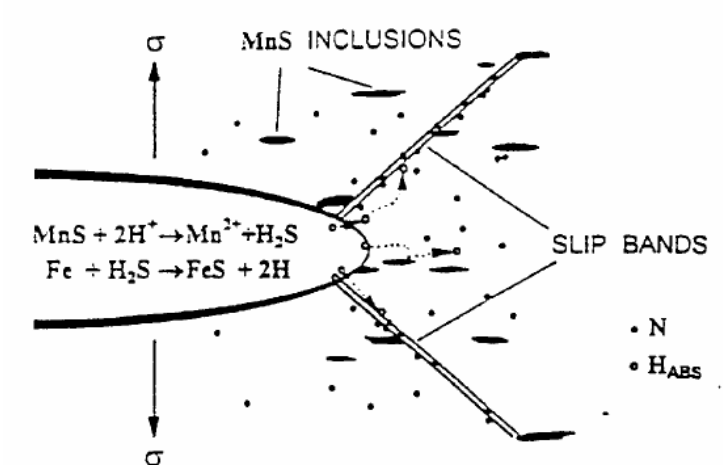

Figure 72. Role of nitrogen and sulfur in formation of slip bands

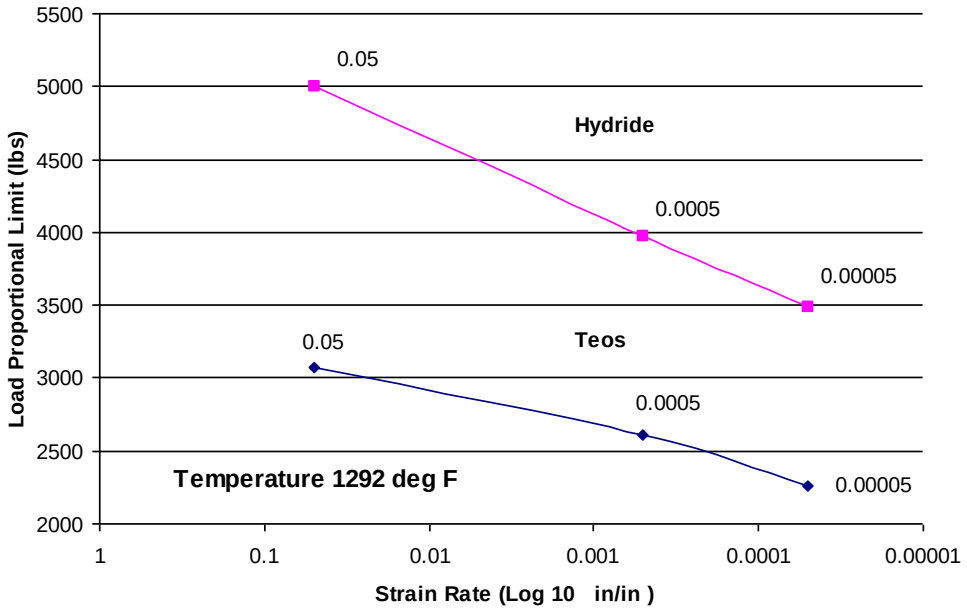

Figure 73. Plots of load at proportional limit vs. strain rate – hydride and teos

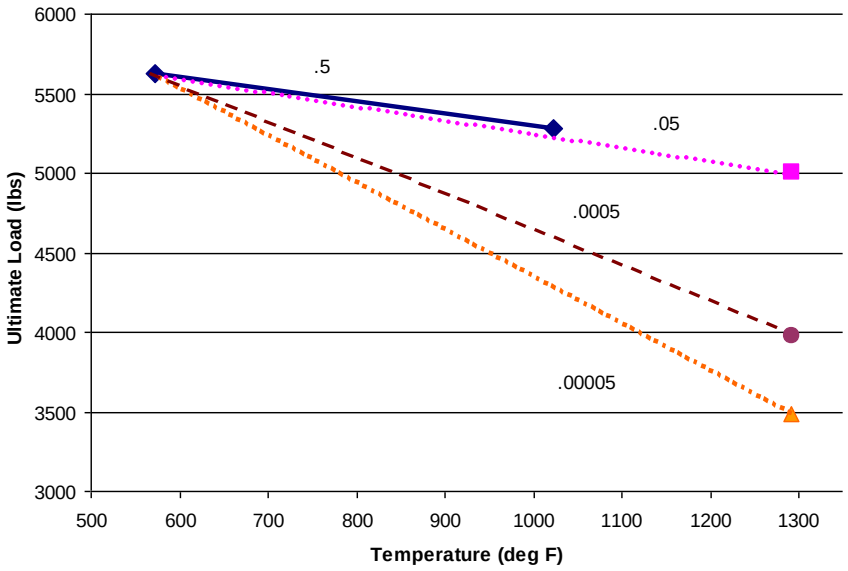

Hydirde

Figure 74. Plots load at ultimate vs. temperature – hydride

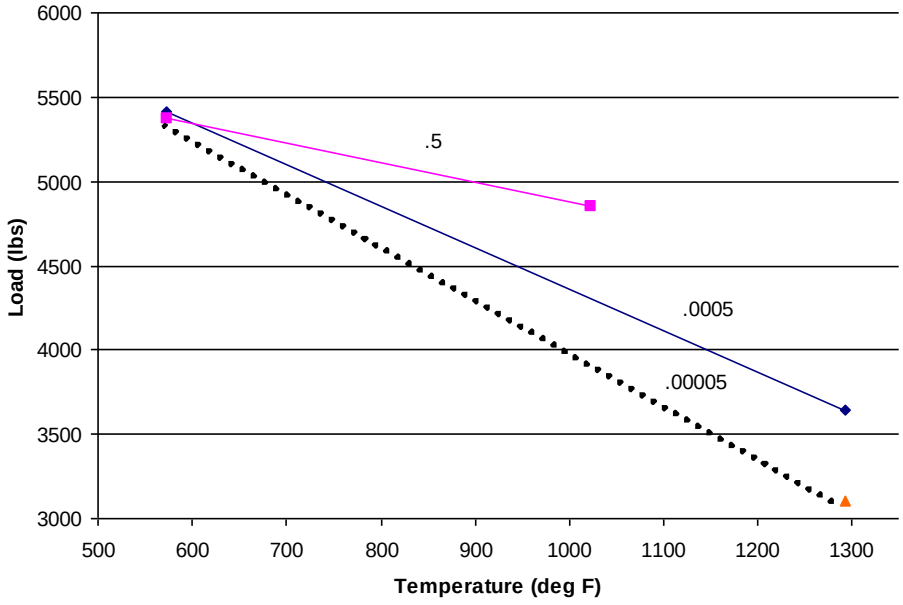

Teos

Figure 75. Plots load at ultimate vs. temperature – teos

Loss of strength was influence by both the temperature and strain-rate. Note the plot of 0.00005, the slowest rate, assumes nearly the same strength at 600 ^{o}F as this test was not run due to the limited number of samples.

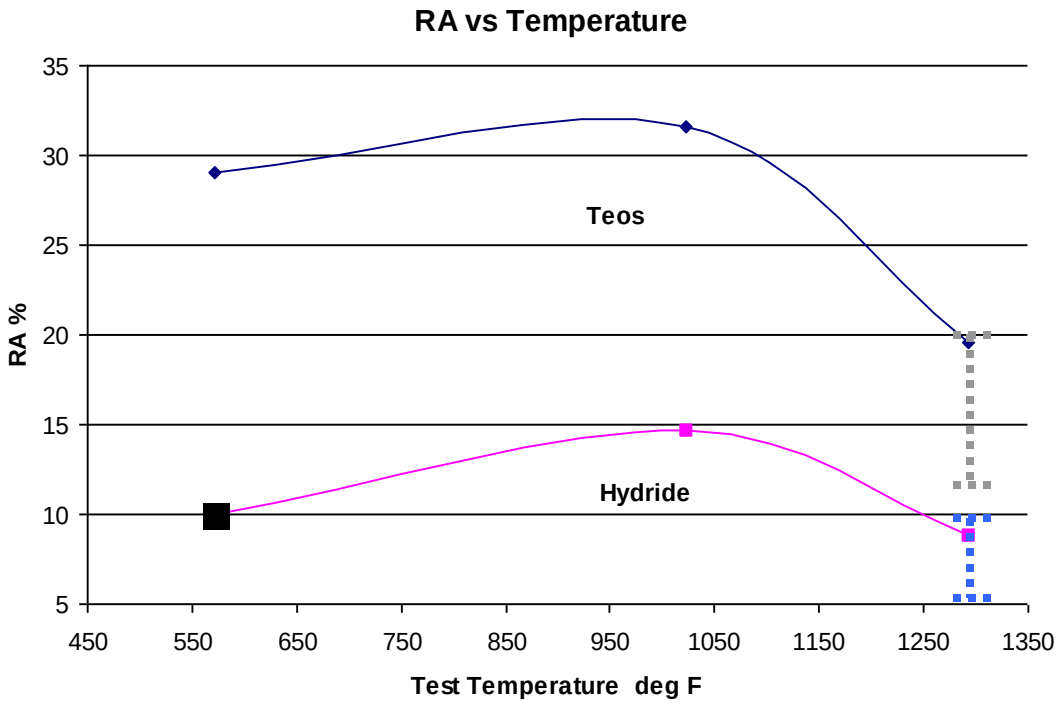

Figure 76. Plots of reduction in area vs. strain rate – teos and hydride

Plots of over aged Teos and Hydride have similar shapes. In the plot of reduction in area Hydride vs. TEOS, Hydride is much less ductile.

5.10 Closure

Crystal structure and bonding in metal alloys alter with mechanical and thermal load in various ways. Room temperature characterization and the models for flow and fracture are insufficient to predict performance at increasing fractions of the homologous temperature. Figures 69 and 70 are excellent in demonstrating Inconel 601 responding to slower strain rate at 1295 ^{o}C. With the ability to simulate the regimes of strain rate and temperature, it is clear both samples of IN 601 lose ductility. Loss of ductility can be attributed to ductility dip fracture and the application of the insight to BIG fracture of Hippsley. Further testing is necessary to factually determine cause for the unexpected loss of ductility and premature failure in the alloy and definitively assign cause. It is however reasonable to attribute fractures to the intermediate temperature and slow strain rate as that regime is convincingly demonstrated and characterized by Hippsley. What was not determined was the reason for difference between the two furnace exposures, -Hydride and TEOS. It is clear that there is significant difference between flow after Hydride exposure and Teos exposure. Both modes of fracture were BIG but Teos exposure also exhibits significant change in the modulus and yield properties (figure 70) of the alloy that cannot be explained by ductility dip fracture theory or Hippsley trace element stress enhanced diffusion Further carefully crafted test regimes and examination with sensitive analysis of fractures surfaces and near area fracture surfaces with Auger or SIMS instruments to supplement SEM and EDS are needed. Such characterization of the material and fracture are beyond the resources available and scope of this thesis.

Solute segregation of trace elements has long been implicated in the change of fracture mode from ductile micro void coalescence to low ductility BIG fractures in various alloys and crystal structures. BONCH is an acronym for the atoms Boron, Oxygen, Nitrogen, Carbon, and Hydrogen. These elements as well as Sulfur and Phosphorous are all reported to reduce flow and fracture in various ways and regimes. BONCH atoms are all chemically reactive forming many compounds and all have “Goldschmidt radii” sufficiently small to fit interstitially within commercial alloy lattice structure. Hydrogen embrittlement in welding is the classic example. It is well settled that stress, as derived during rapid heating/cooling during welding, and the presence of hydrogen produce loss of grain boundary cohesion and BIG fracture in the main but mixed mode BIG and transgranular failures are known.

Under the right conditions, trace element solutes of hydrogen, carbon, oxygen, phosphorous, and sulfur have all been implicated in low ductility fracture. Dix and Savage found significant loss of the ductility of X750 when tested in air as opposed to the Vacuum, Argon, or Nitrogen. Hippsley found Sulfur in combination with a partial Oxygen coverage increased the propensity to brittle fracture. Further source of sulfur, effect of stress and mode of crack growth indicated rearrangement within crack tip stress field are consistent with “pure drift” model for decohesion. These elements in combination with low strain rate and intermediate temperature regimes are subject of on-going investigation to ascertain fundamental engineering models and Ab initio determination of the solid-state physics of the fracture.

Uphill diffusion and concentration of elements in solution as demonstrated by Hippsley is a critical un-mixing phenomenon. As such, it has not been addressed in the thermodynamic regular solution model. Speculation suggests an underlying thermodynamic principle may connect ductility dip fracture and stress influenced concentration of trace elements to high-energy regions of the crystals like grain boundaries, twin boundaries, or precipitate interfaces. These regions of crystals are well known to be sinks for dislocations and dislocation flows may be a means for directing movement and concentration of BONCH atoms or Sulfur or Phosphorus. Speculating with the current data suggests ductility dip fracture and the associated fracture regimes are influenced by a characteristic of spinodal decomposition. Clearly, the change in fracture mode is not a consequence of thermal activation terminating in nucleation and growth of new phases.

Chapter 6

CONCLUSION

6.1 Data and Testing

The following conclusions pertain to the system used to study the high temperature behavior of Nickel Based Alloys.

1) The Gleeble can be used to successfully study strain-aging phenomena in nickel base alloys.

The following conclusions apply to the high-temperature mechanical properties characterization of as-received IN 601 plate, strain-aged IN 601 rod, and gun-drilled, strain-aged IN 601 plate.

1) In the as-received plate, the proportional limit and the ultimate tensile strength increased monotonically as strain rate decreased.

2) In the strain-aged rod the proportional limit and the ultimate tensile strength were similar for the high and the low strain rate, and lower at the intermediate rate.

3) In the as-received plate, the Reduction-in-Area at failure decreased monotonically with decreasing strain rate.

4) In the strain-aged rod the Reduction-in-Area at failure decreased monotonically with decreasing strain rate.

5) Gun-drilled, strain-aged plate showed behaviors similar to the strain-aged rod.

6.2 Environmental

The following conclusions pertain to IN 601 test samples taken from materials exposed to service conditions in TEOS and Hydride atmospheres.

1) The Reduction-in-Area of samples made from materials exposed to TEOS and Hydride processing was dramatically lower than pristine and strain aged samples.

2) Reduction-in-Area was significantly lower in Hydride than that found in TEOS samples tested under similar conditions.

3) TEOS samples had lower Yield and UTS than Hydride samples tested under similar conditions.

4) The low ductility in samples made from materials exposed to the TEOS or Hydride process cannot be explained by notch and strain-rate effects alone.

5) The low ductility in samples made from materials exposed to TEOS and Hydride processes can be explained by high temperature diffusion and strain assisted diffusion of damaging materials into the grain boundaries.

6) Strain ageing observed in the pristine materials can be an associated cause for failure in the TEOS and Hydride exposed samples.

6.3 Fractography

The following conclusions are based on SEM fractography of the samples tested and specific regimes studied.

1) Strain aging can explain the increase in stress at failure with lower strain rates in as received (AR) and strain aged (SA) rod and plate.

2) In the AR and SA rod and plate, fractures are microscopically and macroscopically ductile.

3) In the AR and SA rod and plate, ductile dimple orientations on the fracture surface are related to regions of micro-void coalescence in the sample center, with increasing shear evident as the location moves radially from the center of the sample toward the surface

4) In the AR and SA rod and plate, ductile dimples nucleate at inclusions in the material.

BIBLIOGRAPHY

1. Sims C. T., editor, S*uperalloys II,* John Wiley & Sons, New York, 1987
2. Pickering F.B., *Stainless Steels: Past, Present and Future, The Metallurgical Evolution of Stainless Steels*, Pickering F.B., editor, TMS & ASM, 1979
3. B. Ralph, *Grain-Boundaries in Engineering Materials, Grain-Boundary Structure and Kinetics,* ASM, Metals Park OH, 44073, 1980
4. H. Riedel, *Fracture At High Temperature,* Materials Research and Engineering, Springer-Verlag, Berlin Heidelberg New York London Paris Tokyo, 1987
5. Elihu F. Bradley, editor, *Source Book On Materials for Elevated – Temperature Applications,* American Society for Metals, Metals Park, OH, 44073, 1979
6. C.D.Ludin, C.Y.P. Qiao, C.H. Lee, *Standardization of Gleeble Hot Ductility Testing: Part I: Historical Review*, Weldability of Materials, (Proceeding of the Materials Weldability Symposium 8-12 October 1990), ASM International, Materials Park, OH 44703, 1991
7. R.A. Patterson and K.W. Mahin editors, Weldability of Materials (Proceeding of the Materials Weldability Symposium 8-12 October 1990), ASM International, Materials Park, OH 44703, 1991
8. Stoloff N.S. , Sikka V.K. editors, *Physical Metallurgy and Processing of Intermetallic Compounds,* Chapman & Hall, New York, Chapters 1,2,3,4,6, 7, & 14, 1996

9. Honeycombe R. W. *The Plastic Deformation of Metals,* Edward Arnold, London, WC1B3DQ, 2nd ed., 1985
10. deBarbadillo J.J., *Product Development in The 1990's – Adapting to a New Paradigm*, Heat-Resistant Materials II, Proceeding of the 2nd International Conference on Heat-Resistant Materials, Natesan K., Gabesan P., and Lai G., ed., ASM International Metals Park OH, 1991
11. Antolovich S.D., Campbell J.E., *Fracture Properties of Superalloys, Application of Fracture Mechanics for Selection of Metallic Structural Materials,* Gerberich W.W., and Underwood J.H. editors, American society for Metals, Metals Park, OH 44073 Chapter 8, 1982
12. Gannesan P., PlyburnJ., and Tassen C., *INCOLOY Alloy 803, A Cost Effective Alloy for High Temperature Service,* Proceeding of the 2nd International Conference on Heat-Resistant Materials, Gatlinburg, Tennessee, September 1995, ASM Metals Park, OH, 1996
13. Macia M. and Sanders T. Jr., A Study on the Dendritic Growth of Gamma Prime in Astroloy, Proceeding of the 2nd International Conference on Heat-Resistant Materials, Gatlinburg, Tennessee, September 1995, ASM Metals Park, OH, 1996
14. Reed-Hill R., Abbaschian R., *Physical Metallurgy Principles, 3rd ed.* PWS-Kent Publishing Co, Boston, 1992
15. Parker E.R., *Creep of Metals,* High Temperature properties of Metals, American society for Metals, Cleveland OH 1951

16. Rosenberg H.M., *The Solid State --- An Introduction to the Physics of Crystals for Students of Physics,* Materials science and Engineering, Oxford University Press, Walton Street, Oxford OX26DP, 1988
17. Barrett C.S., Massalaski T.B., *The Structure of Metals—Crystallographic Methods, principles, and Data,* M^{c}Graw-Hill, New York, 3rd ed., Chapters 1,4,8,10-15,18-21, 1966
18. Tien J.K., Coply S.M., “The Effect of Orientation and Sense of Applied Uniaxial Stress on the Morphology of Coherent Gamma Prime Precipitates in Stress Annealed Nickel-Base Superalloy Crystals”, *Metallurgical Transactions,* Vol 2. pp 543—553, ASM, February 1971
19. Loomis W., PhD Thesis, University of Michigan, Ann Arbor, MI, 1969, follows Sims C.T., editor, Superalloys II, John Wiley & Sons, New York, page 131, 1987
20. Dix A.W., and Savage W.F., “Factors Influencing Strain-Age Cracking in Inconel W-750”, *Welding Journal (Welding Research Supplement),* pp247s—261s, AWS, June 1971
21. Kelly T.J., “Welding Metallurgy of Investment Cast Nickel Based Superalloys”, *Weldability of Materials, (Proceeding of the Materials Weldability Symposium 8-12 October 1990), OH 44073, 1991*
22. Von Ohain V., “The Evolution and Future of Aero propulsion Systems”, *The Jet Age,* Boyne W.J. and Lobez D.S., editors, National Air and Space Museum, 1979

23. Coleman W.H., Steele G.W. Jr., *Experimentation and Uncertainty Analysis for Engineers 2ed,* John Wiley & Sons, Inc., 1999

24. Dieter G.E., *Mechanical Metallurgy,* McGraw-Hill, New York., 2nd ed., 1976

25. Tetelman A.S., McEvily A.J. Jr., *Fracture of Structural Materials*, John Wiley & Sons, Inc., 1967

26. Shubat J.G., Committee Chair, *Fractography and Atlas of Fractographs,* Volume 9, American Society for Metals, Metals Park, OH 44073, 1974

27. Mills K., editor, ASM HandbookVolume12, *Fractography, ASM International, Metals Park, OH. 44073 2nd Printing 1992*

28. Massalski T.B., editor, "Precipitation Hardening of Superalloys by Ordered γ' – Particles" *Progress in Materials Science,* Vol. 29 number 3, Pergamon Press, Oxford, 1985

29. Meyers M.A., Chawala K.K., *Mechanical Metallurgy Principles and Applications,* Prentice-Hall, Inc., Englewood Cliffs, N.J., 1984

30. Averbach B.L., et al., editors, *Fracture,* Proceeding of An International Conference on The Atomic Mechanisms of Fracture Held in Swampscott, Massachusetts, April 12-16, 1959, M.I.T. Press, Cambridge, Massachusetts

31. Guttmann V., editor, *Phase Stability In High Temperature Alloys,* Applied Science Publisher LTD, London, Chapters 3 & 4, 1981

32. Doremus R.H., *Rates of Phase Transformations*, Academic Press, Inc, London, 1985

33. Caskey R.H., *Rates of Phase Transformations*, Academic Press, Inc, London 1985

34. Manir G.N., et al. “Correlation of Gamma-Gamma prime Mismatch and Strengthening in Ni/Fe-Ni Base Alloys Containing Aluminum and Titanium as Hardeners”, *Metallurgical Transactions,* Vol. 2, pp.1028-1030, Pergamon Press, Oxford, G.B., AND The M.I.T. Press, Cambridge, Mass U.S.A., no date
35. Langdon T.G., “Dislocation Mechanism Maps: Application to Alloy Design”, Encyclopedia of Materials Science and Engineering, Vol 2., pp. 1028-1030, Pergamon Press, Oxford, G.B., and the M.I.T. Press, Cambridge, Mass U.S.A, no date
36. Lagneborg R., “Dislocation Mechanisms in Creep”, *International Metallugical Reviews, Vol. unk, pp. 130-146,* The institute of Metals, 1976
37. Editor, et al., Assessment and Use of Creep-Rupture Data, American Society for Metals, no date
38. Kestenbach H.J., “Creep of 316 stainless Steel Under High Stresses”, *Acta Metallurgica, Vol. 26, pp. 661-670,* Pergamon Press*, G.B., 1978*
39. Argon A.S. and Bhattacharya A.K., “Primary Creep in Nickel: Experiments and Theory”, *Acta Metallurgica,* vol. 35, pp. 1499-1514, Pergamon Press, G.B., 1987
40. Cary C. and Strudel J.L., “Apparent and Effective Creep Parameters in Single Crystals of a Nickel Base Superalloy—II Secondary Creep”, *Acta Metallurgica*, Vol. 26 pp. 859-870, Pergamon Press, G.B., 1978

41. Dyson B.F. and Gibbons T.B., “Tertiary Creep in Nickel-Base Superalloys: Analysis of Experimental data and Theoretical Synthesis”, *Acta Metallurgica*, Vol. 35, pp. 2355-2369, Pergamon Press, G.B., 1987
42. Tweeddale J.D., The Mechanical Properties of Metals: Assessment and Significance, pp. 65-70, American Elsevier Publishing Company, Inc., 1964
43. Zhu S.M. et al., “Creep Behavior of a β' (Ni_3Al) Precipitation Strengthened Ferritic Fe-Cr-NiAl Alloy”, *Acta Metallurgica,* pp. 2969-2976, Pergamon Press, G.B., 1998
44. Ortner S.R. and Hippsley C.A., “High Temperature Brittle Intergranular Failure in Austenitic Stainless steels”, *Materials Science and Technology,* Vol. 8, pp. 883-895, unk., October 1992
45. Kameda J. and Bevolo A.J., Mechanism of High Temperature Brittle Intergranular Cracking in Hi strength Nickel Alloys, Creep of Materials (Proceedings of the Fifth International Conference on Creep of Materials), Lake Buena Vista, Florida, USA, 18-21 May 1992
46. Lewandowski J.J. Hippsley C.A. et al., “Effects of Impurity Segregation and Test Environment on Sustained Load Cracking of 2 ¼ Cr 1 Mo Steel—II Crack Propagation”, *Acta Metallurgica,* , pp. 2081-2090, Pergamon Press, G.B., 1987
47. Hippsley C.A., “Sulfur Segregation and High-Temperature Brittle Intergranular Fracture in Alloy Steels”, *Acta Metallurgica,* Vol. 35 pp. 2399-2416, Pergamon Press, G.B., 1987

48. Hippsley C.A. et al., “Stress-Driven Solute Enrichment of Crack-Tips During Low-Ductility Intergranular Fracture of Low Alloy Steel”, *Acta Metallurgica*, Vol. 32, pp. 1381-1394, Pergamon Press, G.B., 1984

49. Shin J. and McMahon C.J., “Mechanisms of Stress Relief Cracking in a Ferritic Steel”, *Acta Metallurgica,* Vol. 32, pp. 1535-1552, Pergamon Press, G.B., 1984

50. Lassila D.H. and Birbaum H.K., “Intergranular Fracture of Nickel: The Effect of Hydrogen-Sulfur Co-Segregation”, *Acta Metallurgica,* Vol. 35, pp. 1815-1822, Perhamon Press, G.B., 1987

51. Thorp S.J., “Effect of Gaseous HCL on Sulfur Segregation and Intergranular Embittlement in 321 Stainless Steel”, *Acta Metallurgica*, Vol 32, pp. 1297-1304, Pergamon Pres, G.B., 1984

52. Seah M.P., “Adsorption-Induced Interface Decohesion”, *Acta Metallurgica,* Vol. 28, pp. 995-962, Pergamon Press, G.B., 1980

53. Van Den Beukel a., “On the Mechanism of Serrated Yielding and Strain Ageing”, *Acta Metallurgica*, Vol. 28, pp. 965-969, Pergamon Press, G.B., 1980

54. Goods S.H. and Nix W.D., “The Coalescence of Large Grain Boundary Cavities in Silver During tension Creep*”, Acta Metallurgica,* Vol. 26. pp. 753-758, Pergamon Press, G.B., 1978

55. Urcola J.J. and Sellers C.M., “Effect of Changing Strain Rate On Stress-Strain Behavior During High Temperature Deformation”, *Acta Metallurgica,* Vol. 35, pp. 2637-2647, Pergamon Press, G.B., 1987

56. Poirier J.P., “Is Power-Law Creep Diffusion Controlled?”, *Acta Metallurgica*, Vo. 26, pp. 629-637, Pergamon Press, G.B., 1978

57. Farris J.P. et al., “On the Scatter in Creep Rupture Times”, *Metallurgical Transactions* A, Vol. 21A, pp. 345-352, ASM, February 1990

58. Medina S.F. and Hernandez C.A., “General Expression of the Zenner-Holomon Parameter as a Function of the Chemical Composition of Low Alloy and Microalloyed Steels”, *Acta Metallurgica,* Vol. 44, pp. 137-148, Pergamon Press, G.B., 1996

59. Hicks P.D. and Altsetter C.J., “Hydrogen-Enhanced Cracking of Superalloys”, *Metallurgical Transactions* A, vol. 23A, pp. 237-249, ASM, January 1992

60. Brindley B.J., “The Effect of Dynamic Strain-ageing on the Ductile Fracture Process in Mild Steel”, *Acta Metallurgica,* Vol. 18, pp. 325-329, Pergamon Press, G.B., 1970

61. Lim L.C., “Cavity Nucleation at High Temperatures Involving Pile-Ups of Griain Boundary Dislocations”, *Acta Metallurgica,* Vol. 35, pp. 1663-1673, Pergamon Press, G.B., 1987

62. Raj R., “Nucleation of Cavities at Second Phase Particles in Grain Boundaries”, *Acta Metallurgica*, Vol. 26, pp. 995-1006, Pergamon Press, G.B., 1978

63. Goods S.H. and Nix W.D., “The Kinetics of Cavity Growth and Creep Fracture in Silver Containing Implanted Grain Boundary Cavities”, *acta Metallurgica,* Vol. 26, pp.739-752, Pergamon Press, G.B., 1978

64. Floreen S. and Davidson J.M., “The Effects of B and Zr on the Creep and Fatigue Crack Growth Behavior of a Ni-Base Alloy”, *Metallurgical Transactions* A*,* Vol. 24A, pp. 895-901, ASM, May 1983

65. Jao J.G. and Varma S.K., “The Effect of Grain Size and Strain Rate on the Substructures and Mechanical Properties in Nickel 200”, *Metallurgical Transactions* A, Vol. 24A. pp. 2559-2567, ASM, November 1993

66. Dix A.W. and Savage W.F., “Stress Relaxation and Strain-Age Cracking in Inconel X-750”, *Welding Journal (*Welding Research Supplement), pp. 247s-252s, AWS, June 1971

67. Franklin J.E. and Savage W.F., “Stress Relaxation and Strain-Age Cracking in Rene 41 Weldments”, *Welding Journal*, (Welding Research Supplement), pp. 380s-387s, AWS, September 1974

68. Keiji S. and Tomisawa Y., “Cracking by Elevated Temperature Embrittlement in the HAZ pf Alloy 800H”, *Transactions of the Japan Welding Society,* vol. 22, pp. 10-15, unk., April 1991

69. White J.H. et al., “High Temperature Embrittlement of Ni and Ni-Cr Alloys by Trace Elements”, *Metallurgical Transactions* A, Vol. 14A, pp. 595-610, ASM, April 1983

70. Duval D.S. and Owczarski W.A., “Studies of Postweld Heat-Treatment Cracking in Nickel=Base Alloys”, *welding Journal* (Welding Research Supplement), pp. 10s-22s, AWS, January 1969

71. George E.P. et al., “Creep Cavitation in Iron—I Sulfides and carbides as Nucleation Sites”, *Acta Metallurgica,* Vol. 35, pp. 2471-2486, Pergamon Press, G.B., 1987

72. Mulfor R.A., “Grain Boundary Segregation in Ni and Binary Ni Alloys Doped With Sulfur”, *Metallurgical Transactions* A, Vol. 14A, pp. 865-870, ASM, May 1983

73. Kameda J. and Bevelo A.J., “Mechanism of High Temperature Brittle Intergranular Cracking in High Strength Nickel Alloys”, *Creep of Materials* (Proceeding of the Fifth International Conference on Creep of Materials, Lake Buena Vista, Florida, USA 18-24 May), 1992

74. Meyers M. and Chawala K., Mechanical Metallurgy—Principals and Applications, Prentice-Hall Inc., New Jersey, 1984

75. Briant C.L. editor., Impurities in Engineering Materials, Impact, Reliability and Control, Marcel Dekker, Inc., New york, 1999

76. Caron P., High γ' Solvus New Generation Nickel-Based Superalloys for Single Crystal Turbine Blade Applications, *Superalloys* Metals Park,

77. Course Notes Dartmouth Edu. Flow and Fracture: Deformation Mechanisms and Deformation Maps, WEB, http://engineeringDartmouth/edu/defmech/2014
78. ASM Source Book, no date, p48.
79. Stephen Floreen, et al, “The Metallurgy of Alloy 625, p 13-37, Superalloys 718, 625, 706 and Various Derivatives, E.A. Loria, Editor, The Minerals, Metals, and Materials Society, 1994
80. Karl A. Heck, “The Time-Temperature-Trans-formation Behavior of Alloy 706, P 393-404, Superalloys 718, 625, 706 and Various Derivatives, E.A. Loria, Editor, The Minerals, Metals, and Materials Society, 1994
81. Xishan Xie, et al, “TTT Diagram of a Newly Developed Nickel-Base Superalloy-- Allvac® 718Plus™”, p193-201, Superalloys 718, 625, 706 and Various Derivatives, E.A. Loria, Editor, The Minerals, Metals, and Materials Society, 2005
82. Frost, Harold J. Flow and Fracture. Dartmouth ENG EDU., 2014
83. Roger C. Reed, *Superalloys – Fundamentals and Applications*, Cambridge University Press, 2006.
84. Web Search, Google, “Calculation Gamma Prime Solvus” ONERA, Post, Regression Formula, 2015